ARTICLE TYPE

A micromechanical Mean-Field Homogenization surrogate for the stochastic multiscale analysis of composite materials failure

Juan Manuel Calleja Vázquez † * | Ling Wu * | Van-Dung Nguyen †* | Ludovic Noels *,**

¹Computational & Multiscale Mechanics of Materials, Liège Université, Liège, Belgium

Correspondence

† F.R.S.-FNRS Rue d'Egmont 5 - B 1000 Bruxelles Email: {jmcalleja, vandung.nguyen}@uliege.be

* Liège Université, CM3 B52, Allée de la découverte 9, B4000 Liège, Belgium. Email: {jmcalleja, vandung.nguyen}@uliege.be, {l.wu, l.noels}@ulg.ac.be

** Corresponding author l.noels@ulg.ac.be

Summary

This paper presents the construction of a Mean-Field Homogenization (MFH) surrogate for nonlinear stochastic multiscale analyses of two-phase composites that allows the material response to be studied up to its failure. The homogenized stochastic behavior of the studied unidirectional composite material is first characterized through full-field simulations on stochastic volume elements (SVE) of the material microstructure, permitting to capture the effect of the microstructural geometric uncertainties on the material response. Then, in order to conduct the stochastic nonlinear multiscale simulations, the microscale problem is substituted by a pressure-dependent MFH reduced order micromechanical model, that is, a MF-ROM, whose properties are identified by an inverse process from the full-field SVE realizations. Homogenized stress-strain curves can be used for the identification process of the nonlinear range, however, a loss of size objectivity is encountered once the strain softening onset is reached. This work addresses this problematic introducing a calibration of the energy release rate obtained with a nonlocal MFH micromechanical model, allowing to scale the variability found on each SVE failure characteristics to the macroscale. The obtained random effective properties are then used as input of a data-driven stochastic model to generate the complete random fields used to feed the stochastic MF-ROM. To show the consistency of the methodology, two MF-ROM constructed from SVE of two different sizes are successively considered. The performance of the MF-ROM is then verified against an experimental transverse-compression test and against full-field simulations through nonlocal Stochastic Finite Element Method (SFEM) simulations. The implementation of the energy release rate calibration allows to conduct stochastic studies on the failure characteristics of material samples without the need for costly experimental campaigns, paving the way for more complete and affordable virtual testing.

KEYWORDS:
Surrogate, Stochastic, Mean-Field Homogenization, Incremental-Secant, Failure, Size Objectivity, Nonlocal, Data-Driven Sampling, Random Field

1 | INTRODUCTION

The inherent complexity of the manufacture of composite materials constitutes a major concern for all those industries in which the use of these materials has recently been introduced. Many of these industries need a thorough characterization of the properties and characteristics of the used materials for certification purposes, for which a large number of tests are normally needed. This costly step could be largely reduced by means of virtual testing, being possible to characterize the variability in the performance and the main properties of these materials without the need of real-life testing campaigns.

Stochastic Finite Elements (SFEM) are a way of approaching this problematic [1]. This methodology is based on proper random fields [2] that allow representing the stochastic properties of the material. These random fields would have to be obtained from a large number of experiments in order to obtain accurate results, which is not always possible. In order to avoid this costly step, these random fields can be defined from micromechanical information ([2],[3]) that contains the statistic properties of the uncertainties present on the microstructure of the material, being then possible to generate realistic virtual microstructures that contain the same stochastic properties as the real material. This has been done for multiple microstructures as shown in the review by L. Noels [4]. Some examples are the works on Unidirectional (UD) fiber reinforced composites ([5],[6],[7]), for woven composites ([8],[9],[10]) and for particle-reinforced composites [11]. In most cases, a homogenization step is needed, as the macro and the microscale sizes are separated by several orders of magnitude [2].

In order to perform this homogenization step, multiple approaches have been developed ([12],[13]). Their goal is to predict the mesoscopic or macroscopic responses of a given material. The first approach is to solve full-field Boundary Value Problems (BVP) on a microscale volume in which the different material phases are represented at each material point of the macrostructure ([14],[15],[16]). The Finite Element Square (FE²) ([17],[18]) method uses Finite Element (FE) simulations for the full-field analysis, being capable of yielding accurate predictions thanks to the explicit definition of the microstructures and the phases properties on the microscale BVP. However, these approaches still imply high computational requirements due to the explicit definition of the microstructure. This methodology has been mainly used taking into account a deterministic microscale called Representative Volume Element (RVE). This RVE must be statistically representative of the microstructure, which means that its size varies with the number of sources of uncertainties. Some works have focused on the correct definition of this RVE for different heterogeneous material microstructures. Such is the case of the integrated framework using fast statistical homogenization procedure (FSHP) developed in [19]. The developed framework makes use of the virtual element method (VEM) and allows to efficiently converge towards the RVE size detection by solving a series of simulations. The FSHP has been used for the estimation of effective properties in a wide variety of random heterogeneous microstructures, such as for random porous materials [20] or ceramic matrix composites (CMC) [21]. In some cases, the existence of the definition of an RVE is impossible because of the large size required to be statistically representative of nonlinear behaviors ([22],[23]), meaning that the separation criterion for a multiscale analysis is not always met.

If the separation criterion is not met, the multiscale analysis should be performed based on multiple virtual microstructures called Stochastic Volume Elements (SVEs) [3] (see Fig. 1). With the use of multiple SVEs, the homogenized properties depend on the location as well as the applied boundary conditions ([7],[23],[24],[25],[26],[27],[28]). These SVEs are the means used to propagate the uncertainties from the microscale to the macroscale ([23],[24],[25],[26]), which means that in order to obtain accurate macroscale simulations, the mesh used in these simulations must have a size lower than the correlation length, which itself depends on the size of the SVE used to define the random properties of the microscale [29]. This implies a strong constraint on the mesh level, making the direct stochastic FE² methodology unaffordable nowadays since a large number of simulations are needed.

Accelerating the homogenization process can be done by means of a Reduced Order Model (ROM), which speeds up the microscale solution with off-line computations. This method projects the governing equations into a suitably selected reduced order space where the microscale model is solved with a reduced number of unknown variables which are defined by means of proper orthogonal decomposition of the degrees-of-freedom [30]. The computational cost of the solution of the internal forces resulting from the evaluation of local constitutive equations could be even further reduced by the application of hyper-reduction techniques ([31],[32]). In the context of order reduction using a micromechanics-based homogenization model, non-uniform transformation field analysis (NTFA) [33] reduces the field of internal variables by using the pre-defined internal variables modes obtained with off-line full-field analyses and a tangent second-order (NTFA-TSO) expansion of the dissipation potential reduces the evolution equations related to the reduced internal variables [34]. Clustering the volume elements and applying self-consistent homogenization of the nonlinear clusters response to avoid nonlinear pre-off-line computations is an efficient alternative [35]. In the work of D. Pivovarov et al. [36], hyperreduction is performed through a new element-based modification of the element-based
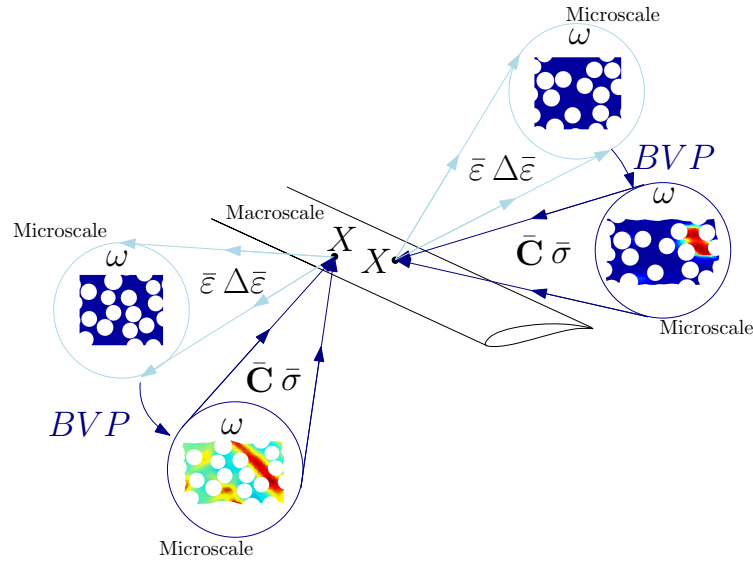
FIGURE 1 Nonlinear stochastic homogenization-based multiscale analysis schematic.

empirical approximation method (EDEAM), which is combined with proper orthogonal decomposition. ROM's have been used in stochastic analyses, for example, a ROM capable of accounting for the geometrical uncertainties of the fibers was developed by using a mesoscale potential for finite elasticity ([37],[38]), however, even if the use of ROM accelerates the multiscale simulation by several orders of magnitude, the quantity of pre-off-line computations needed to perform Monte Carlo (MC) simulations of nonlinear complex materials and the amount of memory required to store the data makes this method to be mainly applied to deterministic analyses.

In order to avoid the computation of the homogenized properties of a microstructure, or to at least solve only a limited amount of them, the use of surrogate models has seen an increased interest, making stochastic multiscale simulations of complex nonlinear materials finally possible. In the seek for maximum efficiency, machine learning has recently been used to this end, as a limited amount of microstructure computations would be needed to train the algorithm, and therefore to build the surrogate. In [39], the database of thermal conductivities used for the training of the algorithm was obtained with the use of a Fast Fourier Transform (FFT) homogenization method on different microstructures. This data-set was used as an input for the training of a supervised machine learning. This surrogate model showed its capabilities not only predicting a given microstructure behavior, but also good inverse design capabilities. In the work by X. Lu et al. [40], a data-driven FE^2 method was developed, for which a hybrid Neural Network (NN) interpolation scheme was introduced, achieving an improved accuracy of the NN surrogate and permitting to lower the number of RVE needed as database for the training of the NN to account for microstructure variations. Similarly, NN has been used in [41], in which a data-driven multiscale method for anisotropic electrical responses has been developed, and in [42], where its use in calibration of surrogate models is seen as promising. Liu et al. introduced the concept of Deep Material Network (DMN)[43], which focuses on the modeling of two-phase heterogeneous composite materials, allowing for good extrapolation capabilities in terms of the material behavior thanks to its ability to predict the interaction between the composite constituents. This concept was later used in other works, such as in T. Huang et al. [44], which introduced a microstructure-guided deep material network that avoided the need for further training to predict the nonlinear response of new microstructures, allowing for good accuracy while largely improving the efficiency of the modeling of heterogeneous materials with uncertainty.

In [45], a surrogate model for linear elasticity was developed by using the Mean-Field Homogenization (MFH) theory for the stochastic ROM (MF-ROM) definition. MFH is a semi-analytical technique developed to obtain efficient modeling of multi-phase composites. Being initially conceived for the modeling of linear elastic composites by using the Eshelby single inclusion [46], the Mori-Tanaka ([47],[48]) solutions or the self-consistent schemes ([49],[50]) to model the interaction between multiple inclusions, it has been later extended to nonlinear composites with the Linear Comparison Composite (LCC) concept ([51],[52]). However, with the use of MFH, the uncertainty effects of the microstructure are not taken directly into account. Contrary to the computation homogenization method, these uncertainties are now contained in a vector of random parameters that will define the effective material properties which are identified by an inverse analysis performed on the full-field SVE simulations. In the works by L. Wu et al. ([45],[53]), a stochastic nonlinear micromechanics model serving as mesoscale surrogate model for UD composite

materials was developed for linear and further extended to nonlinear behaviors. This surrogate model was used as the input of a SFEM analysis. The geometric microscale information was obtained through SEM images of real UD materials, and then used to build synthetic microstructures SVEs of arbitrary size and number[7]. However, the method was not able to account for failure.

The purpose of this paper is to develop a stochastic Mean-Field Reduced Order Model (MF-ROM) capable of modeling the nonlinear and the post-strain softening behaviors of two-phase UD composite materials and to generate a database used to feed random fields for SFEM analyses. To that end, as shown in Fig. 2, full-field realizations are performed on virtual SVEs generated with stochastic information extracted from experimental measurements[7]. The homogenized responses obtained from these SVE realizations are then used as the input of an inverse identification process that allows identifying the random effective parameters of the stochastic MFH micromechanical surrogate, which serves as a surrogate that can be used as input for SFEM.
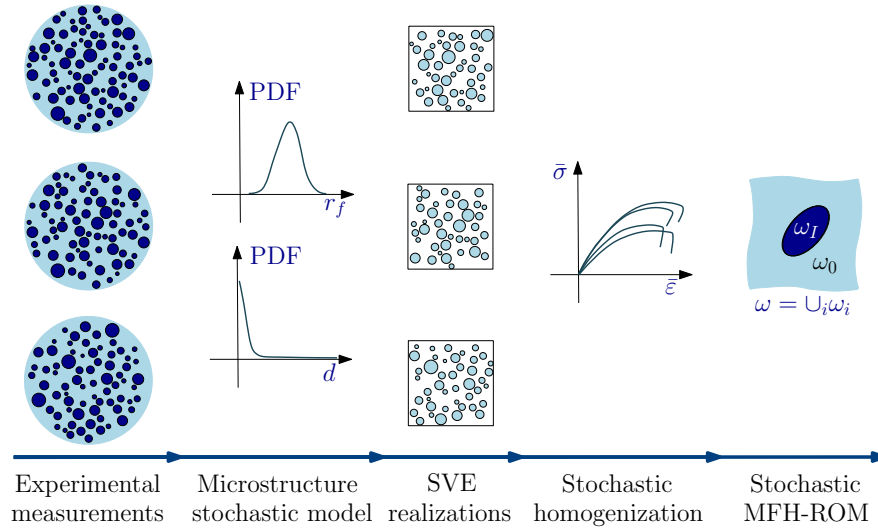

FIGURE 2 Schematic representation of the generation of the stochastic MF-ROM. r_f stands for fiber radius, d stands for the fiber nearest distance, $\bar{\sigma}$ and $\bar{\varepsilon}$ stand for the homogenized macro-stress and strains, and ω_i stand for the phases i that compose the composite ω.

Similar approaches for the construction of the stochastic MFH-ROM have already been developed for the cases of linear elasticity and damaged-enhanced J_2 plastic behaviors ([45,7,53]), however, when modeling real composite materials, some discrepancies were found in the material response under different internal pressure conditions. For this reason, the pressure-dependent MFH scheme developed in[54] is used in this work. Also, it was stated, that the obtained homogenized behavior of the SVE is not representative once the strain softening onset is reached, because of the loss of size objectivity of the SVE response encountered once this point is reached, meaning the homogenized stress-strain curves no longer represent a valid quantity for the identification process. In order to be able to recover this size objectivity, the inverse process must rely on a new reference quantity that allows to recover it ([55,56]). Different quantities, such as the traction-displacement jump softening response, the critical energy release rate or the fracture toughness of the material ([57,58,55,59,56]) have been used in the past to address this problem. In this paper, as the MFH scheme is energy consistent during this phase because of the nonlocal formulation of the damage evolution law, the critical energy release rate (G_c) has been chosen as the parameter used to recover this size objectivity. The critical energy release rate is then extracted from each SVE realization, permitting to upscale the variabilities found in the failure stage of each SVE to the macroscale through a calibration of the MFH micromechanical surrogate model. This will allow the stochastic MF-ROM to correctly predict not only the effect of the variabilities in the linear and nonlinear stages, but also the variabilities and characteristics of the failure stage.

The paper is divided into 5 Sections. Section 2 focuses on the full-field SVE realizations step, from which the data needed for the surrogate construction will be extracted (see steps 3 and 4 of Fig. 2). This Section presents the mathematical basis of the microscale problem and the scale transition of the obtained results, followed by the development of the models used to define the composite phases and the presentation of the performed finite element simulations. Then, Section 3 focuses on the MFH surrogate model and the identification of its parameters. This Section briefly presents the basis of the linear-elasticity MFH,

and the nonlinear MFH schemes. In this work, the nonlocal incremental secant scheme is used in order to model the nonlinear behavior of the composite material including its failure. The inverse identification of the model parameters used for the definition of the MF-ROM completes this Section. The inverse identification is detailed for the elastic and pressure-dependent nonlinear stages of the material response and is completed with the implementation of a calibration process allowing to recover the size objectivity once the strain softening onset is reached. This identification process is then applied to the UD composite SVE realizations in order to construct the MF-ROM, being possible to show a comparison between the predicted MFH responses and the full field SVE results in order to evaluate the accuracy of the inverse-identification process. The identification of parameters is performed for SVE samples of 45×45 μm^2 and 25×25 μm^2, which allows verifying the consistency of the presented methodology. The obtained effective random parameters are analyzed in Section 4, which ends with a brief introduction of the data-driven sampling method used to obtain proper random fields needed for the construction of the stochastic MF-ROM and a comparison between the distributions of the identified and the generated data. This MF-ROM is then applied to the resolution of stochastic simulations in Section 5. To this end, two test cases will be used. First, transverse loading tests performed on ply realizations are used as test cases to show the performance of MF-ROM and be able to assess the results obtained through the two property field discretizations corresponding to the two SVE lengths, by comparing the results with full-field realizations. Then, the validity of the MF-ROM is tested directly against a real-life transverse compression test on a UD composite material.

2 | SVE REALIZATIONS AND THEIR APPARENT RESPONSES

In this work a homogenization-based nonlinear stochastic multiscale analysis is performed. Several scales are involved in this analysis. As shown in Figs. 1 and 2, the homogenized responses seen at the macroscale level are obtained from the microscale resolution. This section will present the main equations governing the relation between the different scales. First, the scale transition and a brief recall of the computational homogenization basics are presented, followed by the models used to represent the composite phases in the finite-element simulations. When performing the SVE simulations, large local deformations appear in the matrix regions embedded between two contiguous fibers. Therefore a finite strain setting has to be considered at the SVE level although the homogenized strain remains limited to a few percents. Finally, this Section concludes with the generation of the full-field SVE realizations and the extraction of their responses, including during their failure stage.

2.1 | Microscale boundary value problem

Let us consider a point X belonging to the macroscale volume Ω. In the multiscale analysis based on homogenization, the deformation gradient tensor $\bar{\mathbf{F}}$ and its increment $\dot{\bar{\mathbf{F}}}$ are obtained from the macroscale Boundary Value Problem (BVP). Then, the BVP resolution of the microscale volume element with domain $x_{\text{ref}} \in \omega$, which represents a point of the studied macrostructure X, allows the macro-stress tensor $\bar{\sigma}$ to be evaluated.

The position x of a material particle at time t is defined as a two-point mapping of its initial position at the reference configuration x_{ref} such that: $x = x(x_{\text{ref}}, t)$. Defining the displacement vector $u = x - x_{\text{ref}}$, the deformation gradient tensor $\mathbf{F}$ writes:

$$\mathbf{F} = x \otimes \boldsymbol{\nabla}_0 = \mathbf{1} + u \otimes \boldsymbol{\nabla}_0, \tag{1}$$

where $\mathbf{1}$ stands for the second-order identity tensor, and $\boldsymbol{\nabla}_0$ stands for the gradient operator with respect to the reference configuration. The energetically conjugate to the deformation gradient tensor, the first Piola-Kirchhoff stress $\mathbf{P}$, is used as the stress measure.

The microscale is composed of different phases ω_i, having that $\cup_i \omega_i = \omega$. Assuming that classical continuum mechanics applies, the equilibrium equations read:

$$\begin{cases} \mathbf{P} \cdot \boldsymbol{\nabla}_0 = \mathbf{0} & \forall x_{\text{ref}} \in \omega, \\ T = \mathbf{P} \cdot N & \forall x_{\text{ref}} \in \partial\omega, \end{cases} \tag{2}$$

where T is the surface traction on boundary $\partial\omega$ with outward unit normal N. The material constitutive law is written as:

$$\mathbf{P} = \mathbf{P}\left(\mathbf{F}(t); q(\tau), \tau \in \left[0, t\right]\right). \tag{3}$$

Plasticity makes deformation to be a path-dependent process, being then necessary to take the strain history into account. To that end, a set of internal variables q that stores this history dependence is used. In the case of a damage-enhanced material, the strain softening implies a mesh dependency of the result if a local formulation is used. In order to avoid this mesh dependency, the

implicit nonlocal model ([60],[61],[62],[63]) is used to define the nonlocal internal variables $\breve{q}$. This formulation states that the relation between the internal variable $q_i \in q$ and its nonlocal counterpart $\breve{q}_i \in \breve{q}$ follows a Helmholtz-type equation, which writes:

$$\breve{q}_i(\boldsymbol{x}_{\text{ref}}, t) - \boldsymbol{\nabla}_0 \cdot \left(\boldsymbol{c}_{\text{g}}(\boldsymbol{x}_{\text{ref}}) \cdot \boldsymbol{\nabla}_0 \breve{q}_i(\boldsymbol{x}_{\text{ref}}, t) \right) = q_i(\boldsymbol{x}_{\text{ref}}, t) \quad \forall \boldsymbol{x}_{\text{ref}} \in \omega, \tag{4}$$

where, for an isotropic medium[64], $\boldsymbol{c}_{\text{g}} = \text{diag}\left(l^2; l^2; l^2 \right)$, being l the characteristic length scale. It is now possible to rewrite Eq. (3) in a nonlocal form:

$$\mathbf{P} = \mathbf{P}\left(\mathbf{F}(t); \breve{q}(\tau), q(\tau), \tau \in \left[0, t \right] \right). \tag{5}$$

2.2 | Scale transition and computational homogenization

To ensure consistency between scales, the Hill-Mandel condition, which guarantees deformation power consistency, is used. Expressing it in terms of the macroscopic first Piola-Kirchhoff stress tensor $\overline{\mathbf{P}}$ and the macroscopic deformation gradient tensor $\overline{\mathbf{F}}$, one has:

$$\overline{\mathbf{P}} : \dot{\overline{\mathbf{F}}} = \langle \mathbf{P} : \dot{\mathbf{F}} \rangle_\omega = \frac{1}{|\omega|} \int_{\partial\omega} \dot{\boldsymbol{u}} \cdot \boldsymbol{T} dA, \tag{6}$$

where ω stands for the volume element of volume $|\omega|$, $\partial\omega$ stands for its external boundary, $\langle \bullet(\boldsymbol{x}_{\text{ref}}) \rangle_\omega = \frac{1}{|\omega|} \int_\omega \bullet(\boldsymbol{x}_{\text{ref}}) dV$ is the volume average, dA represents the differential area and dV represents the differential volume. This condition allows us to write the weak form equations:

$$\begin{cases} \left\langle \mathbf{P} : \left(\dot{\boldsymbol{u}} \otimes \boldsymbol{\nabla}_0 \right) \right\rangle_\omega - \overline{\mathbf{P}} : \dot{\overline{\mathbf{F}}} = 0, \\ \left\langle (\breve{q}_i - q_i)\dot{\breve{q}}_i + \left(\boldsymbol{c}_{\text{g}} \cdot \boldsymbol{\nabla}_0 \breve{q}_i \right) \cdot \boldsymbol{\nabla}_0 \dot{\breve{q}}_i \right\rangle_\omega = 0. \end{cases} \tag{7}$$

The macroscopic quantities can then be estimated by performing the average over the studied volume. By further integrating by parts and applying the Gauss theorem using Eq. (6), one gets:

$$\begin{cases} \dot{\overline{\mathbf{F}}} = \langle \dot{\mathbf{F}} \rangle_\omega = \frac{1}{|\omega|} \int_{\partial\omega} \dot{\boldsymbol{u}} \otimes \boldsymbol{N} dA, \\ \overline{\mathbf{P}} = \langle \mathbf{P} \rangle_\omega = \frac{1}{|\omega|} \int_{\partial\omega} \boldsymbol{T} \otimes \boldsymbol{x}_{\text{ref}} dA. \end{cases} \tag{8}$$

Contrarily to those quantities for which the scale transition $\overline{\bullet} = \langle \bullet(\boldsymbol{x}_{\text{ref}}) \rangle_\omega$ is performed in the homogenization step, this is the case neither for the local nor for the nonlocal internal variables, for which the macroscopic variables correspond to representations of their microscale counterpart distribution, but not to their volume average.
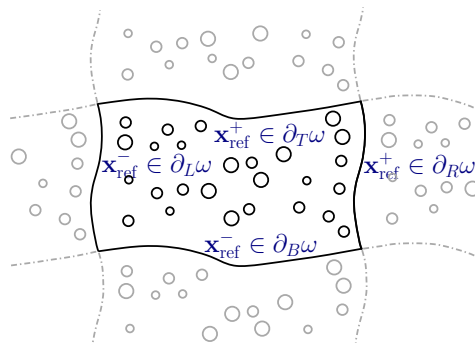

FIGURE 3 Graphical representation of the effect of the periodic boundary conditions on a loaded test sample.

The Hill Mandel condition, Eq. (6), and the evolution of the deformation gradient tensor, Eq. (8), have to be satisfied a priori by the microscopic boundary condition of the displacement field. In this work, the periodic boundary condition is used: the periodic boundary condition decomposes the edges of ω into positive and negative edges, allowing the coincident nodes to be defined. Each point $\boldsymbol{x}_{\text{ref}}^+$ belonging to an edge $\boldsymbol{x}_{\text{ref}}^+ \in \partial_+\omega$ will correspond to its negative counterpart $\boldsymbol{x}_{\text{ref}}^- \in \partial_-\omega$. In this way, the limit $\partial\omega$ of the volume ω will be distributed in these two subdivisions as: $\partial_+\omega = \partial_R\omega \cup \partial_T\omega$ and $\partial_-\omega = \partial_L\omega \cup \partial_B\omega$ (see Fig. 3).

These distributions allow defining the condition of antiperiodicity in the traction field and periodicity in the displacement field for the coincident nodes:

$$\begin{cases} \dot{\boldsymbol{u}}\left(\boldsymbol{x}_{\text{ref}}^{+}\right) - \dot{\boldsymbol{u}}\left(\boldsymbol{x}_{\text{ref}}^{-}\right) = \dot{\bar{\mathbf{F}}} \cdot \left(\boldsymbol{x}_{\text{ref}}^{+} - \boldsymbol{x}_{\text{ref}}^{-}\right), \\ \boldsymbol{T}\left(\boldsymbol{x}_{\text{ref}}^{+}\right) = -\boldsymbol{T}\left(\boldsymbol{x}_{\text{ref}}^{+}\right). \end{cases} \tag{9}$$

Fig. 3 shows a schematic representation of the effect of this Periodic Boundary Condition (PBC) on a loaded sample. This expression implies a direct constraint between opposing nodes, however, this cannot be imposed in general non-periodic meshes. In order to solve this problem the PBC are approximated by an interpolation form[65]. The effect of the BC choice for small periodic and non-periodic volume elements was studied in[66]. By considering volume elements of increasing size, it was shown that for a periodic microstructure the Kinematics Uniform Boundary Condition and Statistic Uniform Boundary Condition respectively overestimate and underestimate the effective response predicted by the PBC, and that for a non-periodic microstructure, the same trend can be observed although some oscillations appear with respect to the volume element size. We thus select the PBC, although this introduces a boundary effect for the small SVEs considered in this work. In order to study this boundary effect, we will consider two different SVE sizes during the analyses and will show that both sizes lead to the same statistical content in the macroscale response predictions. Periodic boundary condition is applied on the nonlocal variables as proposed in[56], and we refer to the discussion in Appendix A. A similar idea of the periodicity in the nonlocal variable can be found in[67].

The use of PBC for problems involving failure is debatable, in particular when considering PBC for the nonlocal variables. Indeed, as discussed in the work by Van Dung Nguyen et al.[56], multiple localization bands can appear in the post-peak localization stage, which is considered to be a nonphysical result[68]. Nevertheless, during the post-peak localization stage characterized by a loss of size objectivity, the stress-strain response cannot be used and, in this work, we consider the dissipated energy as a consistent value. For this value to be unaffected by the PBC, we consider tensile loading conditions, for which the failure band is perpendicular to the loading direction ([56]), allowing to correctly capture the stress-strain relation before softening onset and the dissipated energy of the sample during failure. For this reason the uniaxial tension condition will later be the preferred loading condition for the calibration of the post localization onset stage.

2.3 | Information extracted from the SVE realizations

The system of equations is then complete and can be solved by the multiplier elimination method[69]. From these SVE realizations, the fourth order homogenized macroscopic tensor $\bar{\boldsymbol{C}} = \frac{\partial \bar{\boldsymbol{\sigma}}}{\partial \bar{\boldsymbol{\varepsilon}}}$ can be extracted (where the Cauchy stress tensor $\bar{\boldsymbol{\sigma}}$ and the small strain tensor $\bar{\boldsymbol{\varepsilon}}$ write: $\bar{\boldsymbol{\sigma}} = \det(\bar{\mathbf{F}})^{-1} \bar{\boldsymbol{P}} \bar{\mathbf{F}}^{T}$ and $\bar{\boldsymbol{\varepsilon}} = 1/2(\bar{\mathbf{F}}^{T} + \bar{\mathbf{F}}) - \boldsymbol{I}$). In order to perform the inverse identification process, the SVE fiber volume fraction as well as the homogenized macro stress-strains ($\bar{\boldsymbol{\sigma}}; \bar{\boldsymbol{\varepsilon}}$) and the homogenized macroscopic damaged elastic tensors $\bar{\boldsymbol{C}}^{\text{elD}}$ are extracted. This macroscopic damaged elastic tensor $\bar{\boldsymbol{C}}^{\text{elD}}$ is computed as the homogenized composite material tensor during a virtual elastic unloading.

These quantities allow to perform the elastic and damaged-enhanced plastic regimes identifications[53], however, these quantities are not valid once the strain-softening onset is reached. Between the dissipation and the localization onset stages, the development of the damage of the composite material starts diffusing over the entire microstructure. However, once the SVE stress reaches its peak, the so-called localization onset, the dissipated energy released during this stage does not scale to the entire microstructure, as localization begins to unfold on a microscopic scale. A loss of the size objectivity is therefore encountered after the localization onset, meaning that a new objective value must be used in order to be able to recover this size objectivity. To that end, the critical energy release rate G_{c}, computed from the SVE realization, is used. This quantity quantifies the fracture energy released per unit of crack surface, permitting to obtain an objective value to capture the failure characteristics of a given SVE. In order to compute this energy release rate, the dissipated energy $\mathcal{D}$ from the uniaxial tensile test is extracted at each iteration making it possible to evaluate its value through the failure diagram as shown in Fig. 4, in which we assume that $\mathcal{D}$ scales with the SVE volume before onset and with the SVE cross-section after onset.

By obtaining the value of the total dissipated energy at the localization onset and at total failure and assuming a crack perpendicular to the loading direction with surface $S_{0} = W \times 1 \mu\text{m}^{2}$, being W the side length of the square SVE, it is possible to compute the energy release rate as:

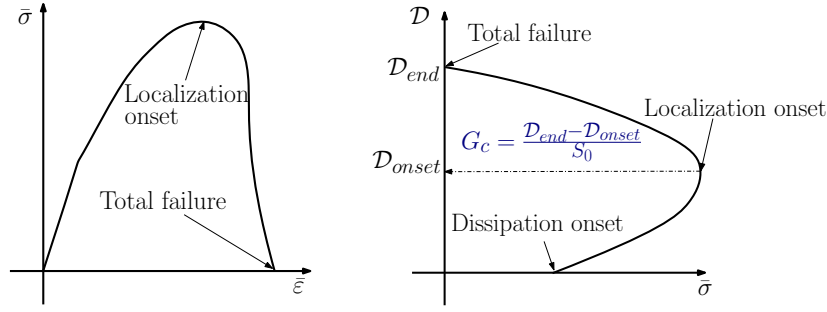$$G_{c} = \frac{\mathcal{D}_{end} - \mathcal{D}_{onset}}{S_{0}}. \tag{10}$$

FIGURE 4 Stress ($\bar{\sigma}$) - strain ($\bar{\varepsilon}$) and energy dissipation (D) - stress ($\bar{\sigma}$) plots used for the computation of the MFH energy release rate G_c.

2.4 | Generation of full-field SVE simulations

In order to extract the microscale information needed to perform the multiscale analysis, the first step is the generation and simulation of stochastic volume elements of the composite material microstructure. The simulated unidirectional composite is composed of high strength carbon fibers UD300/CHS and a matrix of pure RTM6 epoxy resin. This Section will start defining the parameters used to model the inclusion and matrix phases of the composite in the full-field realizations. Then, the used geometries and boundary conditions will be presented, finishing with a brief summary of the methodology used to extract the critical energy release rate (G_c) from the full-field simulations.

2.4.1 | Phase models and parameters

The carbon fibers are modeled as a hyperelastic and transversely isotropic material following the finite-strain setting [70,71] summarized in Appendix A.1. The matrix phase is modeled using the large strain constitutive pressure-dependent elasto-plastic model enhanced by a multi-mechanism nonlocal damage continuum in order to capture the matrix failure [72,56]. The model is summarized in Appendix A.2. Table 1 shows the parameters used for the UD300/CHS inclusions and Table 2 the parameters used to model the RTM6 matrix phase [1] following literature data

TABLE 1 UD300/CHS carbon fiber properties [73] of the model reported in Appendix A.1

| Property of carbon fibers (Unit)	Value
Density ρ (kg/m^3)	1750
Longitudinal Young's modulus E^{L} (GPa)	230
Transverse Young's modulus E^{T} (GPa)	40
Transverse Poisson's ratio ν^{TT} (-)	0.2
Longitudinal-transverse Poisson's ratio $\nu^{\mathrm{LT}} = \nu^{\mathrm{TL}} \frac{E^{\mathrm{L}}}{E^{\mathrm{T}}}$ (-)	0.256
Transverse shear modulus G^{TT} (GPa)	16.7
Longitudinal-transverse shear modulus G^{LT} (GPa)	24

The two phases properties are considered to be uniform across each UD-composite phase, being the geometrical distribution and fibers properties the only source of randomness on the SVE realizations.

---

[1] In the present work we neglect the viscous part of the models and thus we do not report the corresponding paramters

TABLE 2 RTM6 epoxy properties[56] of the model reported in Appendix A.2.

Property of RTM6 epoxy (Unit)	Value
Young's modulus E (MPa)	2450
Yield Exponent α (-)	3.5
Poisson's ratio v (-)	0.39
Plastic Poisson's ratio v_p (-)	0.45
Compressive yield σ_c^0 (MPa)	48
Tensile yield σ_t^0 (MPa)	40.8
Compressive hardening H_c (MPa)	$6475 \exp(-37p)$
Tensile hardening H_t (MPa)	$5503.8 \exp(-37p)$
Kinematic hardening H_b (MPa)	$1412.7p - 5484.8p^2 + 18283p^3$
Saturation damage law D_s (-)	$0.62[1 - \exp(-30p_s)]$
Saturated damage $D_{s\infty}$ (-)	0.62
Saturation damage parameter H_s (-)	30
Saturation damage parameter ζ_s (-)	0
Saturation damage onset p_{s0} (-)	0
. Failure damage parameter ζ_f (-)	1
Failure damage parameter ζ_d (-)	0.3
Failure critital damage D_{f_c} (-)	0.999
Failure critical strain p_{f_c} (-)	0.117
Failure strain onset p_{f_0} (-)	0.
Failure surface parameter a (-)	0.03428
Failure surface parameter b (-)	7.815
Failure surface parameter c (-)	0.02169
Nonlocal length l (μm)	3

2.4.2 | Finite element simulations
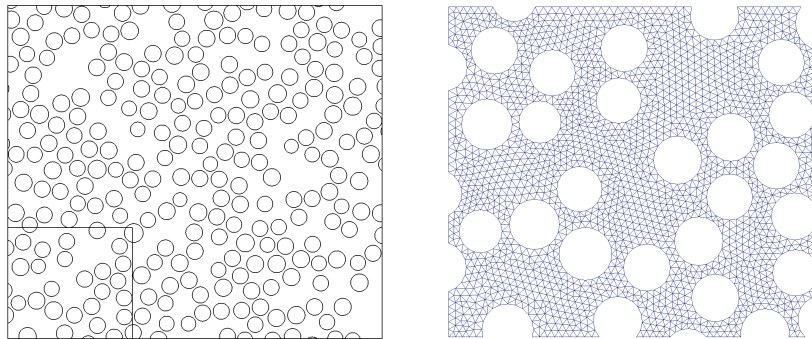
FIGURE 5 Composite window of $135 \times 135 \mu m^2$ with smaller $45 \times 45 \ \mu m^2$ SVE and full-field SVE mesh detail.

In order to carry the full-field simulations, transverse cross-sections of the UD composite are generated at the microscale from dependent variables represented within a copula framework built from SEM images, allowing the generation of microstructures by an inclusions additive process[7]. This SVE generation process allows a realistic statistical distribution of the dependent microscale parameters to be obtained as shown in[7], ensuring the applicability of this work to real-life applications. The statistical information of the microstructure parameters is provided in Appendix B.

One of the major constraints of this kind of approach, as already mentioned, is the size of the SVE used to build the data-set of random homogenized parameters. The use of a larger SVE would allow for a lower number of SVE realizations needed in

order to obtain all the required statistical information. To check the effect of the SVE size in the final obtained responses, two different SVE sizes were used. In order to obtain these SVEs, 100 windows of $135 \times 135 \ \mu m^2$ with an average of 40% fiber volume fraction were generated, from which small windows of $25 \times 25 \ \mu m^2$ or $45 \times 45 \mu m^2$ are extracted as shown in Fig. 5. Then, the extracted SVE is meshed with quadratic elements in order to perform the finite element simulation.
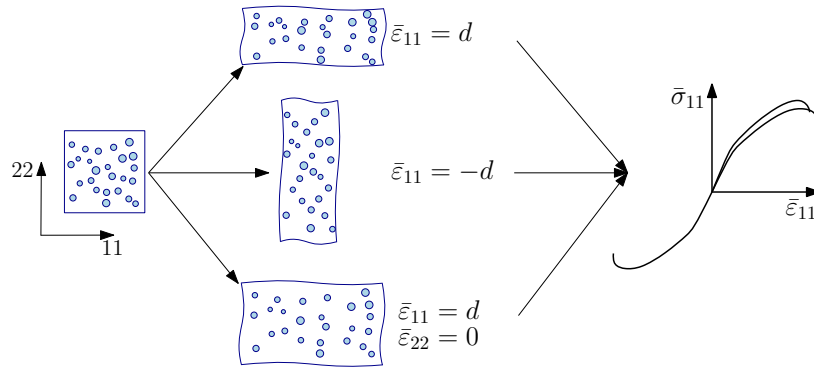

FIGURE 6 Schematic of the three loading conditions tested on each SVE realization. From top to bottom: Uniaxial tensile test, uniaxial compressive test and uniaxial strain test. Letter d stands for the imposed value.

In order to perform the inverse identification introduced in Section 3, three different tests are run for each SVE realization: Uniaxial tensile and compressive loading, and a uniaxial strain test (see Fig. 6). As presented in Section 2.2, periodic boundary conditions are used for these three tests and plane strain conditions are assumed.
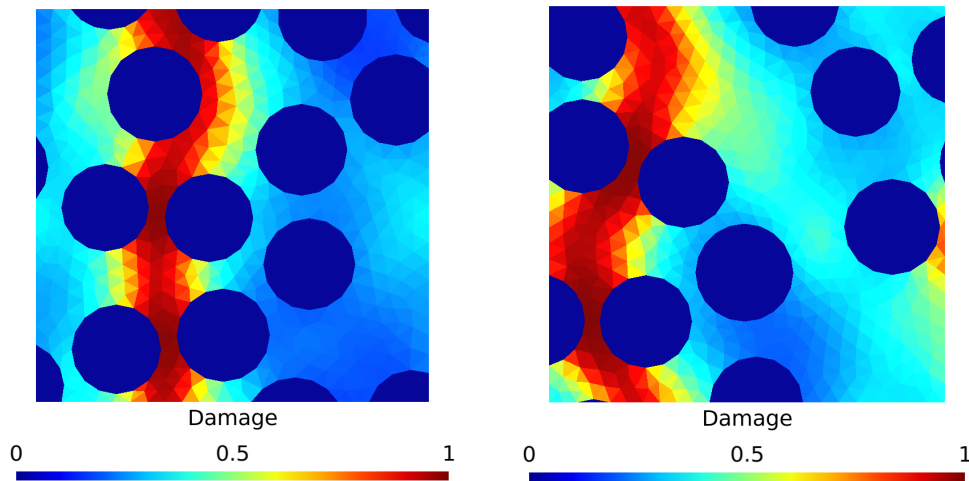

FIGURE 7 Matrix failure damage of two $25 \times 25 \mu m^2$ SVEs under uniaxial tension loading at fracture. SVE 1 on the left and SVE 2 on the right.

As Figs. 7 and 8 show, the used matrix model allows obtaining complex matrix behaviors, including total failure of the sample. The large strain matrix model used in this work allows to accurately capture the behavior of the RTM6 matrix up to its complete failure thanks to the use of the critical energy release rate in the calibration of its failure parameters.

The SVEs are then deformed under tensile loading until reaching their total failure, being possible to extract the uniaxial tensile critical energy release rate G_c. As it is possible to observe in Fig. 9, each SVE will present different characteristics due to the inherent uncertainties contained in these SVEs. This extracted data will then allow us to scale the effect of these uncertainties to larger scales.
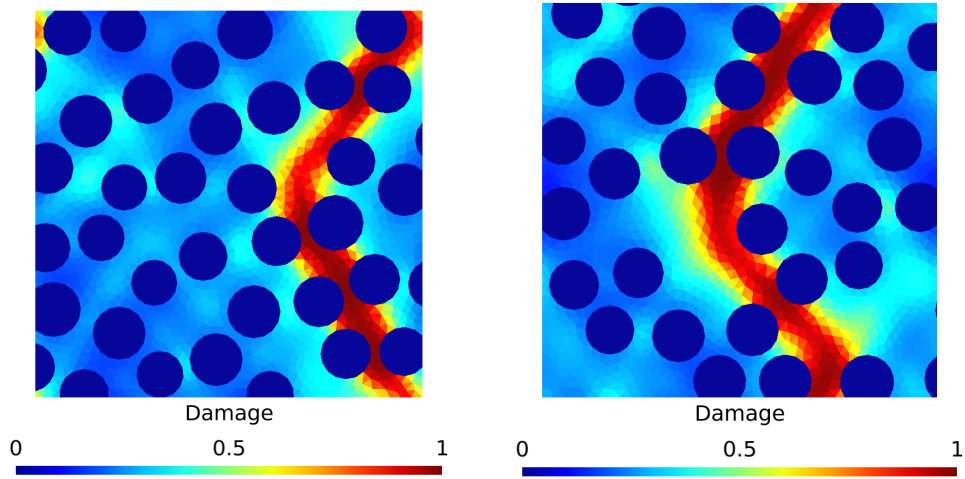
FIGURE 8 Matrix failure damage of two $45 \times 45 \mu\text{m}^2$ SVEs under uniaxial tension loading at fracture. SVE 3 on the left and SVE 4 on the right.
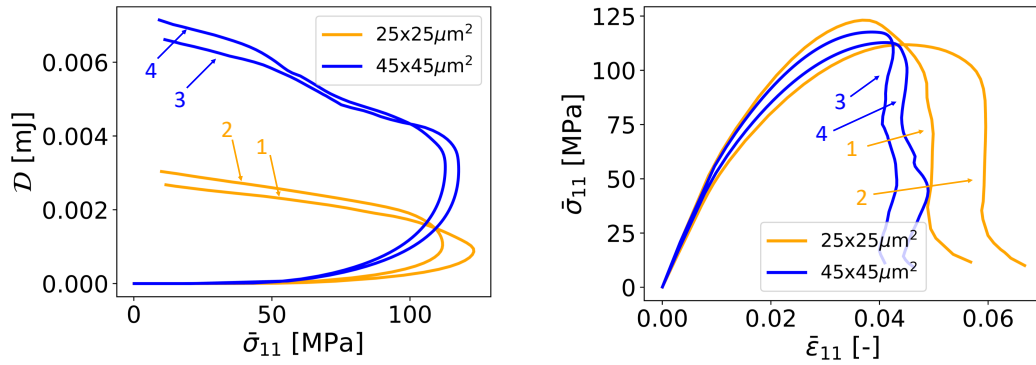

FIGURE 9 Dissipated energy in matrix vs. averaged stress component 11 for SVEs 1, 2, 3 and 4 on the left and averaged stress-strain of SVEs 1, 2, 3 and 4 for component 11 on the right (SVE numbering refers to Figs. 7 and 8).

As an example of the effect of these variabilities found in the material microstructure, the obtained distribution of the SVE G_c can be seen in Fig. 10, which shows the distribution for the two sizes of SVE used in this study. Similar distributions of the energy release rate are obtained for both cases, being the average value slightly higher for the $45 \times 45 \mu\text{m}^2$ SVE samples.
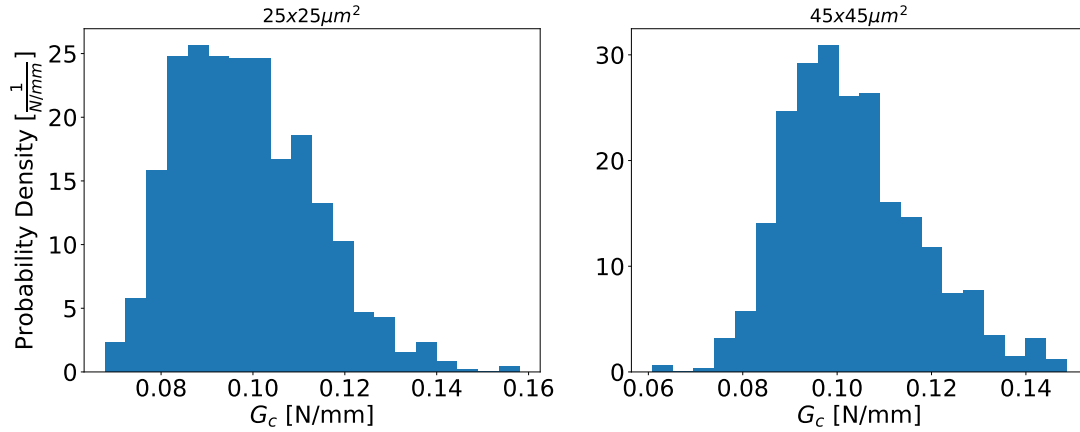
FIGURE 10 Probability density histograms of the energy release rate found in the $25 \times 25 \ \mu\mathrm{m}^2$ and $45 \times 45 \ \mu\mathrm{m}^2$ SVEs

3 | MEAN-FIELD HOMOGENIZATION (MFH) SURROGATE MODEL AND INVERSE IDENTIFICATION PROCESS

In order to build a stochastic MF-ROM capable of capturing all the microstructure variabilities shown by each SVE, an identification process must be developed. The goal of this identification process is to find, for each SVE realization, the parameters of the MFH model that allow obtaining a homogenized material response that is as its full-field counterpart. As seen in Section 2.4.2, failure of the SVE occurs at few percents of deformation at the homogenized level. Therefore the MF-ROM can be developed in a small strain setting. This Section summarizes the basis of the used surrogate model, then the identification process will be developed by presenting the identification method for elastic behaviors first and then for pressure dependent damage-enhanced elasto-plastic behaviors; and finally for the post-strain softening phase up to complete failure.

3.1 | MFH

In this work the Mean-Field Homogenization (MFH) method is used to homogenize the behavior of the composite material. The homogenized composite material will be modeled using a small deformation constitutive model.

Computing the average stress ($\boldsymbol{\sigma}_i$) and strain ($\boldsymbol{\varepsilon}_i$) of a given phase ω_i as:

$$\boldsymbol{\sigma}_i = \frac{1}{|\omega_i|} \int_{\omega_i} \boldsymbol{\sigma}(\boldsymbol{x}_{\mathrm{ref}}) dV,$$
$$\boldsymbol{\varepsilon}_i = \frac{1}{|\omega_i|} \int_{\omega_i} \boldsymbol{\varepsilon}(\boldsymbol{x}_{\mathrm{ref}}) dV. \tag{11}$$

In the studied case of two-phase isothermal composite material, having the matrix (v_0) and inclusion (v_{I}) volume fractions such that $v_0 + v_{\mathrm{I}} = 1$, the scale transition can be rewritten as:

$$\begin{cases} \bar{\boldsymbol{\varepsilon}} = v_0 \boldsymbol{\varepsilon}_0 + v_{\mathrm{I}} \boldsymbol{\varepsilon}_{\mathrm{I}}, \\ \bar{\boldsymbol{\sigma}} = v_0 \boldsymbol{\sigma}_0 + v_{\mathrm{I}} \boldsymbol{\sigma}_{\mathrm{I}}. \end{cases} \tag{12}$$

In small deformation, the local constitutive law for the phases writes:

$$\boldsymbol{\sigma}_i(t) = \boldsymbol{\sigma}_i \left(\boldsymbol{\varepsilon}_i(t); \boldsymbol{q}_i(\tau), \tau \in [0, t] \right). \tag{13}$$

The notation $\boldsymbol{\sigma}_i$ refers to the microscopic Cauchy stress tensor of phase i and $\boldsymbol{\varepsilon}_i$ is the phase i small-deformation strain tensor. Plasticity makes deformation to be a history-dependent process, being then necessary to take this history into account. To that end, a set of internal variables that stores this history dependence $\boldsymbol{q}_i$ is used. We note that $\boldsymbol{q}_i$ are not necessarily the volume average of $\boldsymbol{q}(\boldsymbol{x}_{\mathrm{ref}})$ on the phase ω_i.

In the case of a damage-enhanced material, the strain softening implies a mesh dependency of the result. The implicit nonlocal model[60] is used to define the nonlocal internal variables $\breve{\boldsymbol{q}}_i$ for the MFH. We consider as nonlocal variable the equivalent plastic

strain of the matrix phase. This formulation states that the relation between the internal variable $p_0 \in q_i$ and its nonlocal counterpart $\breve{p}_0 \in \breve{q}_i$ follows a Helmholtz-type equation, which writes:

$$\breve{p}_0 - \nabla_0 \cdot \left(c_{\mathrm{g}} \cdot \nabla_0 \breve{p}_0 \right) = p_0 \quad \text{for} \quad \omega_0, \tag{14}$$

where for an isotropic medium[64], $c_{\mathrm{g}} = \mathrm{diag}\left(l^2; l^2; l^2 \right)$, being l the characteristic length scale. It is now possible to rewrite Eq. (13) in a nonlocal form:

$$\sigma_i(t) = \sigma_i \left(\varepsilon_i(t), \breve{q}_i(\tau); q_i(\tau), \tau \in [0, t] \right). \tag{15}$$

The used MFH methodology will be first introduced for the case of linear materials, completing it afterwards for nonlinear behaviors, for which the incremental-secant MFH method will be introduced.

3.1.1 | Linear behavior

Completing Eq. (12) with the constitutive laws of each of the phases:

$$\begin{cases} \sigma_0 = C_0^{\mathrm{el}} : \varepsilon_0, \\ \sigma_\mathrm{I} = C_\mathrm{I}^{\mathrm{el}} : \varepsilon_\mathrm{I}, \end{cases} \tag{16}$$

where the constitutive material tensors C_i^{el} are considered to be uniform per phase. The MFH scheme reduces the complexity of the SVE formulation, by assuming a simplified morphology of the SVE in which only an ellipsoidal inclusion defined by the geometrical property (I) and volume fraction (v_I) is embedded into the matrix phase.

By defining a strain concentration tensor B^ϵ, it is possible to link the strain averages of the matrix and inclusion phases:

$$\varepsilon_\mathrm{I} = B^\epsilon \left(\mathrm{I}, C_0^{\mathrm{el}}, C_\mathrm{I}^{\mathrm{el}} \right) : \varepsilon_0, \tag{17}$$

where I stands for the geometrical information of the inclusions required to define B^ϵ.

Due to its good performance for two-phase composite materials for which the matrix can be identified, the Mori-Tanaka (M-T) model[47] is used to define the strain concentration. Assuming this model, the strain concentration B^ϵ reads:

$$B^\epsilon \left(\mathrm{I}, C_0^{\mathrm{el}}, C_\mathrm{I}^{\mathrm{el}} \right) = \left\{ I + S \left(\mathrm{I}, C_0^{\mathrm{el}} \right) : \left[\left(C_0^{\mathrm{el}} \right)^{-1} : C_\mathrm{I}^{\mathrm{el}} - I \right] \right\}^{-1}, \tag{18}$$

where S stands for the Eshelby tensor[46].

For the case of linear elastic composites, Eqs. (12, 16 and 17) can be used to write the following constitutive equation:

$$\bar{\sigma} = \bar{C}^{\mathrm{el}} \left(\mathrm{I}, C_0^{\mathrm{el}}, C_\mathrm{I}^{\mathrm{el}}, v_\mathrm{I} \right) : \bar{\varepsilon}, \tag{19}$$

where $\bar{C}^{\mathrm{el}}$ writes:

$$\bar{C}^{\mathrm{el}} \left(\mathrm{I}, C_0^{\mathrm{el}}, C_\mathrm{I}^{\mathrm{el}}, v_\mathrm{I} \right) = \left[v_\mathrm{I} C_\mathrm{I}^{\mathrm{el}} : B^\epsilon \left(\mathrm{I}, C_0^{\mathrm{el}}, C_\mathrm{I}^{\mathrm{el}} \right) + v_0 C_0^{\mathrm{el}} \right] : \left[v_\mathrm{I} B^\epsilon \left(\mathrm{I}, C_0^{\mathrm{el}}, C_\mathrm{I}^{\mathrm{el}} \right) + v_0 I \right]^{-1}. \tag{20}$$

3.1.2 | Nonlinear behavior

As already stated in the Introduction, the MFH method was extended to nonlinear behaviors through the use of a Linear Comparison Composite. This LCC is a fictitious material with linear phases, whose behavior is the same as the linearized behavior of the original composite material. Therefore, considering a material with a matrix phase with virtual elastic operator C_0^{LCC} and inclusions phase with virtual elastic operator $C_\mathrm{I}^{\mathrm{LCC}}$, it is possible to write the MFH equations of a linear composite material. In this case, the relation between the incremental strains of both phases, Eq. (17), can be written as:

$$\Delta \varepsilon_\mathrm{I} = B^\epsilon \left(\mathrm{I}, C_0^{\mathrm{LCC}}, C_\mathrm{I}^{\mathrm{LCC}} \right) : \Delta \varepsilon_0, \tag{21}$$

and the relations between the macro and the micro strains and stresses, Eq. (12), writes:

$$\begin{cases} \Delta \bar{\varepsilon} = v_0 \Delta \varepsilon_0 + v_\mathrm{I} \Delta \varepsilon_\mathrm{I}, \\ \bar{\sigma} = v_0 \sigma_0 + v_\mathrm{I} \sigma_\mathrm{I}. \end{cases} \tag{22}$$

Several approaches have been developed to define this LCC, for example through linearization of the nonlinear constitutive models of the material phases ([74],[75]) or through variational formulations ([76],[77],[15],[78],[79],[80]). Other approaches are the affine formulation ([81],[82],[83], etc.), the incrementally affine formulation ([84],[85]), or the incremental-tangent formulation ([51],[86],[87],[88]).

These formulations yield anisotropic formulations of their tangent operators, leading to stiff predictions of the material behavior and therefore needing an isotropization step[89]. This step is not needed in the case of the incremental-secant linearization ([90],[73],[91],[92],[54]) since its material operators are isotropic by nature. In this work, the incremental-secant formulation is used.

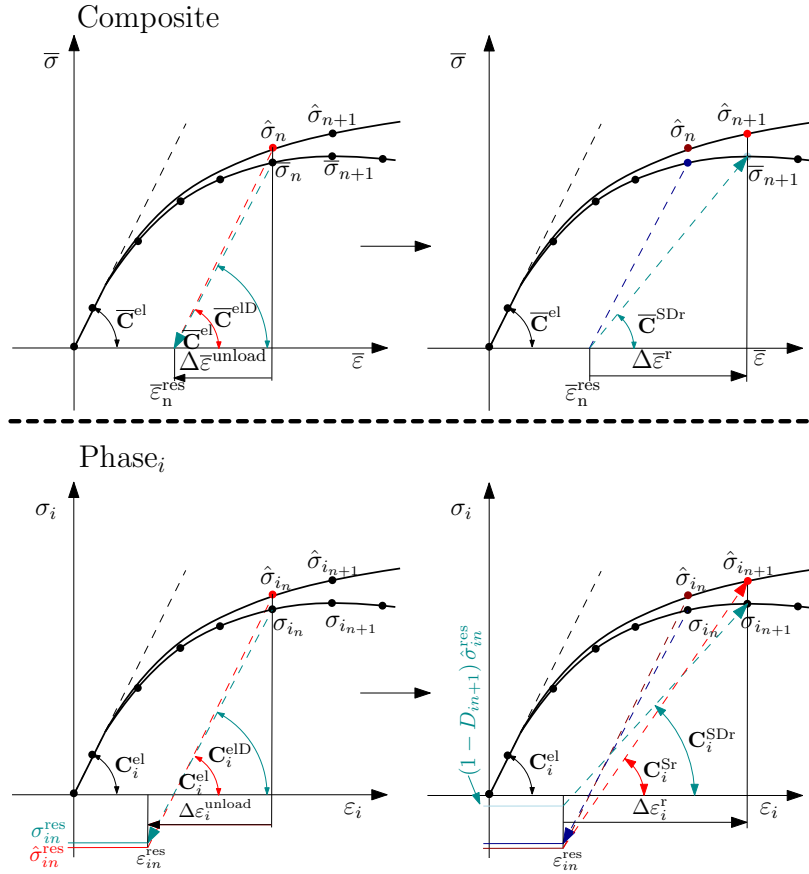### 3.1.3 | Damage-enhanced incremental-secant formulation[73]

FIGURE 11 Composite and phase elastic unloading and loading process for LCC definition for damage-enhanced elasto-plastic materials. Virtual elastic unloading on the left pictures and incremental-secant loading on the right pictures.

The incremental-secant formulation consists of two steps at each time increment. Within a time step $[t_n, t_{n+1}]$, the composite is elastically unloaded up to a stress-free state ($\bar{\boldsymbol{\sigma}}_n^{\text{res}} = 0$) from the state at t_n, being possible to obtain the residual stresses within the different phases. Then, the composite is re-loaded up to its new state at step t_{n+1}, defining the LCC via the secant operators of the phases defined from the residual strains and stresses. Fig. 11 shows this process schematically.

As for the case of the large strain model used for the full-field SVE realizations, the damage effect is introduced by a single scalar value (D) in a Lemaitre-Chaboche style[89]. The concept of effective stress ($\hat{\boldsymbol{\sigma}}$) is therefore introduced, having:

$$\hat{\boldsymbol{\sigma}} = \frac{\boldsymbol{\sigma}}{1 - D}. \tag{23}$$

Let us detail the operations carried out at each step.

Virtual elastic unloading:

In this step, a fictitious elastic unloading is applied on the material from the current state up to a stress free state. As shown in Fig. 11, the phase elastic operators $\boldsymbol{C}_i^{\text{el}}$ are used for the computation of this step. Considering a damage-enhanced elasto-plasticity

case with isotropic behavior one has:

$$\begin{cases} \boldsymbol{C}_i^{\mathrm{elD}} = (1 - D_i)\, \boldsymbol{C}_i^{\mathrm{el}}, \\ \boldsymbol{C}_i^{\mathrm{el}} = 3\kappa_i^{\mathrm{el}} \boldsymbol{I}^{\mathrm{vol}} + 2\mu_i^{\mathrm{el}} \boldsymbol{I}^{\mathrm{dev}}, \end{cases} \tag{24}$$

where κ_i^{el} is the bulk modulus and μ_i^{el} is the shear modulus of the studied phase, and where $\boldsymbol{I}^{\mathrm{dev}} = \boldsymbol{I} - \boldsymbol{I}^{\mathrm{vol}}$ is the deviatoric fourth-order tensor and $\boldsymbol{I}^{\mathrm{vol}} = \frac{1}{3}\mathbf{1} \otimes \mathbf{1}$ the volume fourth-order tensor, being $\mathbf{1}$ the second order identity tensor. For the studied case of the UD composites, only the matrix phase will undergo damage; it is then possible to rewrite Eqs. (21-22) as:

$$\begin{cases} \Delta\bar{\boldsymbol{\varepsilon}}^{\mathrm{unload}} = v_0 \Delta\boldsymbol{\varepsilon}_0^{\mathrm{unload}} + v_{\mathrm{I}} \Delta\boldsymbol{\varepsilon}_{\mathrm{I}}^{\mathrm{unload}}, \\ 0 = \bar{\boldsymbol{\sigma}}^{\mathrm{res}} = v_0 \boldsymbol{\sigma}_0^{\mathrm{res}} + v_{\mathrm{I}} \boldsymbol{\sigma}_{\mathrm{I}}^{\mathrm{res}}, \\ \Delta\boldsymbol{\varepsilon}_{\mathrm{I}}^{\mathrm{unload}} = \boldsymbol{B}^{\epsilon}\left(\mathrm{I}, \boldsymbol{C}_0^{\mathrm{elD}}, \boldsymbol{C}_{\mathrm{I}}^{\mathrm{el}}\right) : \Delta\boldsymbol{\varepsilon}_0^{\mathrm{unload}}. \end{cases} \tag{25}$$

This can be solved with the general constitutive expression (see Fig. 11):

$$\bar{\boldsymbol{\sigma}} = \bar{\boldsymbol{C}}^{\mathrm{elD}}\left(\mathrm{I}, \boldsymbol{C}_0^{\mathrm{elD}}, \boldsymbol{C}_{\mathrm{I}}^{\mathrm{el}}, v_{\mathrm{I}}\right) : \Delta\bar{\boldsymbol{\varepsilon}}^{\mathrm{unload}}; \tag{26}$$

with $\bar{\boldsymbol{C}}^{\mathrm{elD}}\left(\mathrm{I}, \boldsymbol{C}_0^{\mathrm{elD}}, \boldsymbol{C}_{\mathrm{I}}^{\mathrm{el}}, v_{\mathrm{I}}\right) = \bar{\boldsymbol{C}}^{\mathrm{el}}\left(\mathrm{I}, \boldsymbol{C}_0^{\mathrm{elD}}, \boldsymbol{C}_{\mathrm{I}}^{\mathrm{el}}, v_1\right)$ computed using Eq. (20). The free stress state corresponds only to the unloaded composite, but this is not the case for each of the phases. The phases will be therefore characterized by a residual strain tensor ($\boldsymbol{\varepsilon}_i^{\mathrm{res}}$) and a residual stress tensor ($\boldsymbol{\sigma}_i^{\mathrm{res}}$) where $\bullet_{i_n}^{\mathrm{res}} = \bullet_{i_n} - \Delta\bullet_{i_n}^{\mathrm{unload}}$.

At time t_n, and at unloaded state, the effective stress tensors write:

$$\begin{cases} \hat{\boldsymbol{\sigma}}_{i_n} = \dfrac{\sigma_{i_n}}{(1 - D_{i_n})}, \\ \hat{\boldsymbol{\sigma}}_{i_n}^{\mathrm{res}} = \dfrac{\sigma_{i_n}^{\mathrm{res}}}{(1 - D_{i_n})}. \end{cases} \tag{27}$$

Incremental-secant loading:

[2] Being $\bar{\boldsymbol{\varepsilon}}_{n+1}$ known from the macroscale BVP, it is possible to obtain the strain increment ($\Delta\bar{\boldsymbol{\varepsilon}}_{n+1}^{\mathrm{r}}$) as shown in Fig. 11 by solving:

$$\bar{\boldsymbol{\varepsilon}}_{n+1} = \bar{\boldsymbol{\varepsilon}}_n^{\mathrm{res}} + \Delta\bar{\boldsymbol{\varepsilon}}_{n+1}^{\mathrm{r}}. \tag{28}$$

The strain increments of each phase ($\Delta\boldsymbol{\varepsilon}_{i_{n+1}}^{\mathrm{r}}$) can be found by performing material reloading computations. Considering each phase in the undamaged stress state space, it is possible to define an incremental-secant operator as:

$$\begin{cases} \hat{\boldsymbol{\sigma}}_{i_{n+1}} = \hat{\boldsymbol{\sigma}}_{i_n}^{\mathrm{res}} + \Delta\hat{\boldsymbol{\sigma}}_{i_{n+1}}^{\mathrm{r}}, \\ \Delta\hat{\boldsymbol{\sigma}}_{i_{n+1}}^{\mathrm{r}} = \boldsymbol{C}_{i_{n+1}}^{\mathrm{Sr}} : \Delta\boldsymbol{\varepsilon}_{i_{n+1}}^{\mathrm{r}}, \end{cases} \tag{29}$$

writing the apparent stress tensor as:

$$\boldsymbol{\sigma}_{i_{n+1}} = \left(1 - D_{i_{n+1}}\right)\hat{\boldsymbol{\sigma}}_{i_n}^{\mathrm{res}} + \boldsymbol{C}_{i_{n+1}}^{\mathrm{SDr}} : \Delta\boldsymbol{\varepsilon}_{i_{n+1}}^{\mathrm{r}}, \tag{30}$$

where the damaged incremental-secant operator is defined as $\boldsymbol{C}_{i_{n+1}}^{\mathrm{SDr}} = \left(1 - D_{i_{n+1}}\right)\boldsymbol{C}_{i_{n+1}}^{\mathrm{Sr}}$. From the phase residual state it is then possible to define the LCC with $\bar{\boldsymbol{C}}^{\mathrm{SDr}}$. Eqs. (21) and (22) can be expressed as:

$$\begin{cases} \Delta\bar{\boldsymbol{\varepsilon}}_{n+1}^{\mathrm{r}} = v_0 \Delta\boldsymbol{\varepsilon}_{0_{n+1}}^{\mathrm{r}} + v_{\mathrm{I}} \Delta\boldsymbol{\varepsilon}_{\mathrm{I}_{n+1}}^{\mathrm{r}}, \\ \bar{\boldsymbol{\sigma}}_{n+1} = v_0 (1 - D_{0_{n+1}})\hat{\boldsymbol{\sigma}}_{0_{n+1}} + v_{\mathrm{I}}\hat{\boldsymbol{\sigma}}_{\mathrm{I}_{n+1}}, \\ \Delta\boldsymbol{\varepsilon}_{\mathrm{I}_{n+1}}^{\mathrm{r}} = \boldsymbol{B}^{\epsilon}\left(\mathrm{I}, \boldsymbol{C}_{0_{n+1}}^{\mathrm{SDr}}, \boldsymbol{C}_{\mathrm{I}_{n+1}}^{\mathrm{Sr}}\right) : \Delta\boldsymbol{\varepsilon}_{0_{n+1}}^{\mathrm{r}}. \end{cases} \tag{31}$$

These equations can be solved following the process carried out in [54] and detailed in Appendix C.1. Defining the macroscale incremental-secant operator as:

$$\bar{\boldsymbol{C}}^{\mathrm{SDr}} = \left[v_{\mathrm{I}}\boldsymbol{C}_{\mathrm{I}}^{\mathrm{Sr}} : \boldsymbol{B}^{\epsilon}\left(\mathrm{I}, \boldsymbol{C}_0^{\mathrm{SDr}}, \boldsymbol{C}_{\mathrm{I}}^{\mathrm{Sr}}\right) + v_0 \boldsymbol{C}_0^{\mathrm{SDr}}\right] : \left[v_{\mathrm{I}}\boldsymbol{B}^{\epsilon}\left(\mathrm{I}, \boldsymbol{C}_0^{\mathrm{SDr}}, \boldsymbol{C}_{\mathrm{I}}^{\mathrm{Sr}}\right) + v_0 \boldsymbol{I}\right]^{-1}, \tag{32}$$

Eq. (19) is rewritten in the incremental-secant form as:

$$\bar{\boldsymbol{\sigma}}_{n+1} + v_0 \left(D_{0_{n+1}} - D_{0_n}\right)\hat{\boldsymbol{\sigma}}_{0_n}^{\mathrm{res}} = \bar{\boldsymbol{C}}_{n+1}^{\mathrm{SDr}}\left(\mathrm{I}, \boldsymbol{C}_{0_{n+1}}^{\mathrm{SDr}}, \boldsymbol{C}_{\mathrm{I}_{n+1}}^{\mathrm{Sr}}, v_{\mathrm{I}}\right) : \Delta\bar{\boldsymbol{\varepsilon}}_{n+1}^{\mathrm{r}}. \tag{33}$$

---

[2]In previous works ([91],[73],[53]) it was shown that when using first statistical moments, cancelling the matrix residual stress could help improving the scheme accuracy for composites with stiff inclusions. However, note that as the MFH model is used as a reduced order model, the residual version of the incremental-secant scheme developed in [54] is used in this paper.

3.1.4 | Phase behaviors[54]

In this subsection, we omit the subscript related to the phase for clarity.

For the case of elastic phases, the constitutive material equation is written in terms of the elastic tensor $\boldsymbol{C}^{\text{el}}$ as:

$$\boldsymbol{\sigma} = \boldsymbol{C}^{\text{el}} : \boldsymbol{\varepsilon}. \tag{34}$$

In this paper, the inclusion phase is modeled as a transversely isotropic elastic material, meaning it will be defined by a longitudinal and a transverse Young's modulus (E^{L}, E^{T}), and transverse and longitudinal transverse quantities of the Poisson's ratio (ν^{TT}, ν^{LT}) and the shear modulus (G^{TT}, G^{LT}).

The matrix phase is modeled by a damage-enhanced pressure-dependent elasto-plastic model. In this work, the small-strain pressure-dependent damaged-enhanced incremental secant implementation developed in J.M. Calleja Vázquez et al.[54] of the pressure-dependent yield surface

$$f(\hat{\boldsymbol{\sigma}}) = \left(\frac{(\hat{\boldsymbol{\sigma}})^{\text{eq}}}{\sigma_c}\right)^{\alpha} - 3\frac{m^{\alpha} - 1}{(m+1)\sigma_c}\hat{\phi} - \frac{m^{\alpha} + m}{m+1} = 0, \tag{35}$$

completed by a non-associated flow rule $G = (\phi^{\text{eq}})^2 + \beta\left(\hat{\phi}\right)^2$ as presented in Appendix A.2, is used for the matrix phase. In this last equation, $\hat{\phi} = \frac{1}{3}\text{tr}\,\hat{\boldsymbol{\sigma}} = \frac{1}{3}\hat{\sigma}_{ii}$,

$$\beta = \frac{9\left(1 - 2\nu_p\right)}{2\left(1 + \nu_p\right)}, \tag{36}$$

is a material parameter defined from the plastic Poisson's ratio ν_p at the plastic flow onset, and $m = \frac{\sigma_t}{\sigma_c}$ is the ratio between the current compressive σ_c and tensile σ_t yield stresses. Besides, this model uses a power-enhanced version, the exponent α being a material constant, of the original Drucker-Prager formulation. The hardening evolution laws defining the evolution of the compressive and tensile isotropic yield stresses are defined as a function of the equivalent plastic strain p following $\dot{\sigma}_c = H_c(p)\dot{p}$, and $\dot{\sigma}_t = H_t(p)\dot{p}$. In the MFH surrogate, the ratio between the compressive and tensile yield stresses is assumed to be constant ($m = \frac{\sigma_t}{\sigma_c} = constant$) so that only $H_c(p)$ or $H_t(p)$ has to be defined. This assumption is not restrictive for the methodology. Considering two different hardening laws in tension and compression would allow introducing more parameters in the MFH surrogate in order to capture more accurately different loading modes. The inverse identification method further presented should however be adapted.

In tems of the trial and residual stresses, the yield surface writes:

$$f\left(\hat{\boldsymbol{\sigma}}^{\text{tr}}, \Gamma\right) = \left(\frac{\left(\frac{\hat{\sigma}_{n+1}^{\text{tr}} - \hat{\sigma}_n^{\text{res}}}{1 + 6\mu^{\text{el}}\Gamma} + \hat{\sigma}_n^{\text{res}}\right)^{\text{eq}}}{\sigma_c}\right)^{\alpha} - 3\frac{m^{\alpha} - 1}{(m+1)\sigma_c}\left(\frac{\hat{\phi}_{n+1}^{\text{tr}} - \hat{\phi}_n^{\text{res}}}{1 + 2\kappa^{\text{el}}\Gamma\beta} + \hat{\phi}_n^{\text{res}}\right) - \frac{m^{\alpha} + m}{m+1} = 0, \tag{37}$$

where the superscript "tr" relates to the trial state –i.e. an elastic loading and Γ is the plastic multiplier. The expression (37) of the yield surface was obtained after using the radial return mapping algorithm. By using a first order approximation in the stress space in terms of $\Delta\boldsymbol{\varepsilon}$, the normal direction of the plastic flow writes:

$$\mathbf{Q}_{n+1} = 3\left(\boldsymbol{C}^{\text{Sr}} : \Delta\boldsymbol{\varepsilon}_{n+1}^{\text{r}}\right)^{\text{dev}} + \frac{2\beta}{3}\left(\boldsymbol{C}^{\text{Sr}} : \Delta\boldsymbol{\varepsilon}_{n+1}^{\text{r}}\right)^{\text{vol}} = 3\left(\hat{\sigma}_{n+1} - \hat{\sigma}_n^{\text{res}}\right)^{\text{dev}} + \frac{2\beta}{3}\left(\hat{\sigma}_{n+1} - \hat{\sigma}_n^{\text{res}}\right)^{\text{vol}}. \tag{38}$$

As it can be observed, the normal is composed by a deviatoric and a volumetric terms. By updating this definition of the normal with the plastic correction developments, these deviatoric and volumetric terms can be written as:

$$\mathbf{Q}_{n+1}^{\text{dev}} = \frac{1}{1 + 6\mu^{\text{el}}\Gamma}\left(\mathbf{Q}_{n+1}^{\text{tr}}\right)^{\text{dev}} \quad ; \quad \mathbf{Q}_{n+1}^{\text{vol}} = \frac{1}{1 + 2\kappa^{\text{el}}\Gamma\beta}\left(\mathbf{Q}_{n+1}^{\text{tr}}\right)^{\text{vol}}. \tag{39}$$

It was found in[54] that with this definition of the normal, the tensors defining the LCC are naturally isotropic, being possible to decompose the incremental secant operator $\boldsymbol{C}^{\text{Sr}}$ as:

$$\boldsymbol{C}^{\text{Sr}} = 3\kappa_s^{\text{r}}\boldsymbol{I}^{\text{vol}} + 2\mu_s^{\text{r}}\boldsymbol{I}^{\text{dev}}, \tag{40}$$

where the shear and bulk moduli of phase ω_i are defined as:

$$\kappa_s^{\text{r}} = \kappa^{\text{el}} - \frac{2\beta\kappa^{\text{el}^2}\Gamma}{1 + 2\kappa^{\text{el}}\Gamma\beta} \quad ; \text{ and } \quad \mu_s^{\text{r}} = \mu^{\text{el}} - \frac{6\mu^{\text{el}^2}\Gamma}{1 + 6\mu^{\text{el}}\Gamma}, \tag{41}$$

with the damage counterparts

$$\kappa_s^{\mathrm{Dr}} = \left(1 - D_{n+1}\right)\left(\kappa^{\mathrm{el}} - \frac{2\beta\kappa^{\mathrm{el}^2}\Gamma}{1 + 2\kappa^{\mathrm{el}}\Gamma\beta}\right) \quad ; \text{ and } \quad \mu_s^{\mathrm{Dr}} = \left(1 - D_{n+1}\right)\left(\mu^{\mathrm{el}} - \frac{6\mu^{\mathrm{el}^2}\Gamma}{1 + 6\mu^{\mathrm{el}}\Gamma}\right), \tag{42}$$

The increment of the accumulated plastic strain can be written in terms of the plastic multiplier Γ, the phase strain increment $\Delta\boldsymbol{\varepsilon}^{\mathrm{r}}$ and the secant tensor $\boldsymbol{C}^{\mathrm{Sr}}$ as:

$$\Delta p = \frac{\Gamma}{\sqrt{1 + 2\nu_p^2}}\sqrt{\mathbf{Q}:\mathbf{Q}} = \frac{\Gamma}{\sqrt{1 + 2\nu_p^2}}\sqrt{6\left(\left(\boldsymbol{C}^{\mathrm{Sr}}:\Delta\boldsymbol{\varepsilon}^{\mathrm{r}}\right)^{\mathrm{eq}}\right)^2 + \frac{4}{3}\beta^2\left(\frac{1}{3}\mathrm{tr}\left(\boldsymbol{C}^{\mathrm{Sr}}:\Delta\boldsymbol{\varepsilon}^{\mathrm{r}}\right)\right)^2}, \tag{43}$$

where the first statistical moment is used to compute the equivalent the average von Mises stresses and increment strains, writing:

$$\begin{cases} \boldsymbol{\sigma}^{\mathrm{eq}} = \sqrt{\frac{3}{2}\boldsymbol{\sigma}:\boldsymbol{I}^{\mathrm{dev}}:\boldsymbol{\sigma}}, \\ \Delta\boldsymbol{\varepsilon}^{\mathrm{eq}} = \sqrt{\frac{2}{3}\Delta\boldsymbol{\varepsilon}:\boldsymbol{I}^{\mathrm{dev}}:\Delta\boldsymbol{\varepsilon}}. \end{cases} \tag{44}$$

The damage used to model the damaged-enhanced phase is divided into two contributions: A softening damage (D_s) and a failure damage (D_f). The softening damage models the damage evolution up to the strain-softening onset writing:

$$\Delta D_s = \frac{D_{\mathrm{onset}}}{p_{\mathrm{onset}}}\Delta p, \tag{45}$$

where D_{onset} and p_{onset} are the matrix damage and the accumulated plastic strain at the strain-softening onset respectively. The failure damage D_f contribution starts after the matrix strain-softening onset. This law permits to model the failure characteristics of the material by accelerating the development of damage. The failure damage D_f writes:

$$\Delta D_f = \alpha_{\mathrm{Dam}}\left(p + \Delta p - p_{\mathrm{onset}}\right)^{\beta_{\mathrm{Dam}}}, \quad \text{if} \quad p > p_{\mathrm{onset}}. \tag{46}$$

Finally, the used matrix damage evolution law D writes:

$$\Delta D = \begin{cases} \Delta D_s, & \text{if} \quad p \leq p_{\mathrm{onset}}, \\ \Delta D_s + \Delta D_f, & \text{if} \quad p > p_{\mathrm{onset}}. \end{cases} \tag{47}$$

3.2 | Inverse identification

After presenting the basis of the used surrogate model, this Section will now present the inverse identification process carried out in order to find the micro-mechanical equivalent properties for each of the SVE realizations. This consists in an extension to account for failure of the elastic[45] and elasto-plastic[53] approaches inverse identification approaches. For each SVE we will associate corresponding parameters yielding the same homogenized behavior. As this identification is performed for each SVE realization, as many values of each random descriptors as SVE realizations will be obtained. The notation $(\tilde{\cdot})$ will be used to make reference to the identified parameters. The parameters that will define the inclusion phase will be the fiber volume fraction $\tilde{v}_{\mathrm{I}}$, the major and minor axes ratio of the single inclusion phase ellipsoid $\tilde{\mathrm{I}}$, and its orientation $\tilde{\theta}$. The matrix phase is characterized by its elastic, pressure-dependent plastic and damage parameters. The Young's modulus $\tilde{E}_0$ and the Poisson's ratio $\tilde{v}_0$ describe the elastic matrix behavior. The pressure-dependent plasticity stage is defined by the compressive yield stress $\tilde{\sigma}_c^0$, the parameters $\tilde{H} = \left[\tilde{h}_0, \tilde{h}_1, \tilde{m}_0\right]$ of the further described hardening law, the tension and compression yield stress ratio $\tilde{m}$, the plastic Poisson's ratio $\tilde{v}_p$ and the yield surface exponent $\tilde{\alpha}$. The damage of the matrix phase will depend on the softening damage parameters $\tilde{p}_{\mathrm{onset}}$ and $\tilde{D}_{\mathrm{onset}}$ and its failure damage parameters $\tilde{\alpha}_{\mathrm{Dam}}$ and $\tilde{\beta}_{\mathrm{Dam}}$. A total of 16^3 random effective parameters, which will form the vector $\boldsymbol{\beta}^D$ will be identified for each SVE realization:

$$\boldsymbol{\beta}^D = \left[\tilde{v}_{\mathrm{I}}, \tilde{\mathrm{I}}, \tilde{\theta}, \tilde{E}_0, \tilde{v}_0, \tilde{\sigma}_c^0, \tilde{h}_0, \tilde{h}_1, \tilde{m}_0, \tilde{m}, \tilde{v}_p, \tilde{\alpha}, \tilde{p}_{\mathrm{onset}}, \tilde{D}_{\mathrm{onset}}, \tilde{\alpha}_{\mathrm{Dam}}, \tilde{\beta}_{\mathrm{Dam}}\right]. \tag{48}$$

The inverse identification of a given SVE draws on the results extracted from the full-field simulations. As shown in Fig. 12, the information used for the identification process of each SVE realization is extracted from the three different loading conditions tested. The obtained effective parameter vectors from the full set of SVE realizations will form the effective random parameters vector $[\beta^d]$ that will then serve as input for the generator of new data.

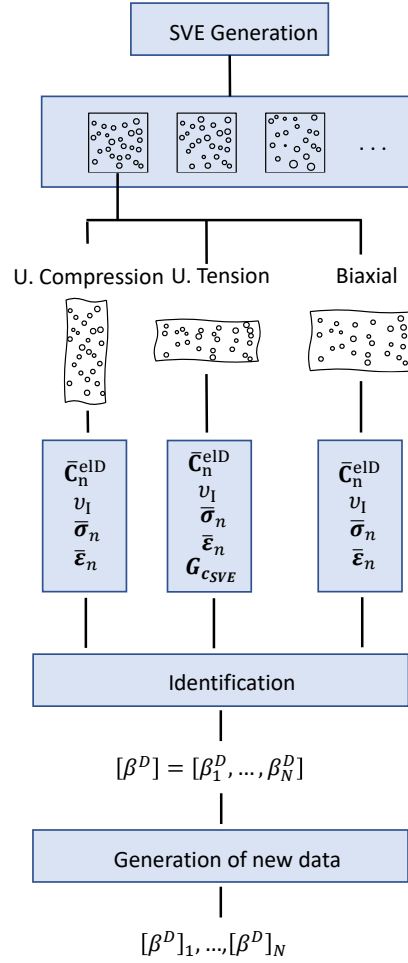[3]Actually $\tilde{\beta}_{\mathrm{Dam}}$ has a fixed value

FIGURE 12 Flowchart of the complete methodology for the generation of the MF-ROM.

This Section will start presenting the identification process for the elastic properties, followed with the nonlinear damaged-enhanced pressure dependent plasticity, and will end with the calibration of the model in order to recover the size objectivity encountered after the strain-softening stage. At the beginning of some key points of the identification process, a line specifying the already identified effective parameters and the parameters that will be identified at that specific point of the process will be introduced. This will allow the reader to more easily identify the MF-ROM parameters needed for its definition and follow the identification process.

3.2.1 | Elastic Composites

At this stage, the known MF-ROM variable is: the fiber volume fraction $[\tilde{v}_I]$. This parameter is directly deduced from the SVE. In this step, the following variables will be identified: $[\tilde{I}, \tilde{\theta}, \tilde{E}_0, \tilde{v}_0]$.

The equivalent inclusion model[45] substitutes the complex microstructure of the composite material by an SVE composed of matrix and a single elliptic inclusion (see Fig. 13). To define the inclusion, the volume fraction v_I and its effective anisotropic elasticity tensor C_I^{el}, which is considered constant for all SVEs, are directly obtained from the SVE realizations. Then, the ratio between the major and minor axes of the inclusion's ellipsoid $\tilde{I}$, and its orientation, denoted by $\tilde{\theta}$, are obtained through the inverse identification process (hence the $\tilde{\bullet}$ notation). In this inverse identification process, the effective elasticity properties of the isotropic matrix $\tilde{C}_0^{el}\left(\tilde{E}_0, \tilde{v}_0\right)$, as well as the effective Young's modulus and Poisson's ratio ($\tilde{E}_0, \tilde{v}_0$ respectively) are identified to characterize the matrix phase.

In order to identify the elastic random descriptors, the elasticity tensor of the equivalent composite ($\tilde{\tilde{C}}^{el}$), Eq. (20), which depends on the variables $\tilde{I}, \tilde{\theta}, \tilde{E}_0, \tilde{v}_0$, has to be as similar as possible to the homogenized elasticity tensor extracted from the SVE
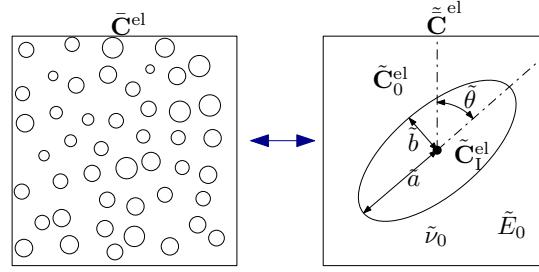
FIGURE 13 Schematic representation of the elastic full-field SVE and its MFH virtual counterpart.

realizations ($\bar{\boldsymbol{C}}^{\text{el}}$). To that end, the following optimization process is performed:

$$\min_{\tilde{\text{I}},\tilde{\theta},\tilde{E}_0,\tilde{v}_0} \left\| \tilde{\boldsymbol{C}}^{\text{el}} \left(\tilde{\text{I}}, \tilde{\theta}, \tilde{\boldsymbol{C}}_0^{\text{el}} \left(\tilde{E}_0, \tilde{v}_0 \right); \boldsymbol{C}_{\text{I}}^{\text{el}}, v_{\text{I}} \right) - \bar{\boldsymbol{C}}^{\text{el}} \right\|, \tag{49}$$

where $\|\bullet\|$ stands for the Frobenius norm. By performing this minimization problem for each of the SVE realizations, the elastic random descriptors are identified.

3.2.2 | Nonlinear damage-enhanced elasto-plastic composites up to strain softening

Once the geometrical information of the inclusion and the effective elastic descriptors of the matrix are identified, the nonlinear behavior descriptors of the matrix, including the plasticity onset, are still to be identified. In order to perform the identification of the pressure-dependent matrix model parameters, three different loading conditions are used in order to characterize all its parameters. These different loading conditions allow obtaining information about the effect of different hydrostatic pressures on the composite material response. In this work, uniaxial tension and compression and biaxial tension ($\bar{\varepsilon}_{22} = 0$) loading conditions are used for the identification of the material parameters (as previously shown in Fig. 6). Since the incremental-secant formulation is used, the loading curves will be divided into loading increments and virtual elastic unloadings.
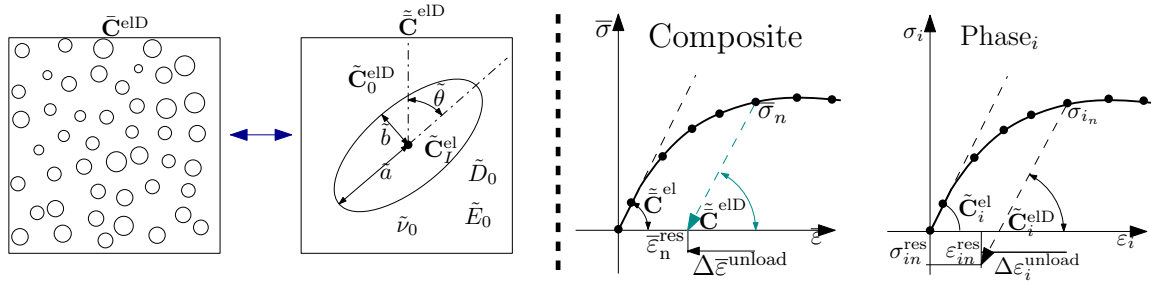
FIGURE 14 Schematic representation of the damaged elastic full-field SVE and its MFH virtual counterpart (left) and schematic unloading phase in a stress-strain plot (right).

Effective damage evolution.

The first step consists in identifying the effective damage D_0 present at each loading increment. To that end, as the damaged elastic tensor is extracted from the full-field simulation, the virtual elastic unloading step at each iteration can be used to extract the value of the damage evolution [53] (see Fig. 14). In this work, damage is taken into account on the matrix phase of the composite through the scalar damage variable D_0. The effective damage $\tilde{D}_0$ of the matrix phase is obtained through the following minimization problem:

$$\min_{\tilde{D}_{0_n}} \left\| \tilde{\boldsymbol{C}}_n^{\text{elD}} \left(\tilde{\boldsymbol{C}}_{0_n}^{\text{elD}} \left(\tilde{D}_{0_n}; \tilde{\text{I}}, \tilde{\theta}, \tilde{E}_0, \tilde{v}_0 \right), \boldsymbol{C}_{\text{I}}^{\text{el}}, v_{\text{I}} \right) - \bar{\boldsymbol{C}}_n^{\text{elD}} \right\|, \tag{50}$$

where $\tilde{C}_{0_n}^{\text{elD}}\left(\tilde{D}_{0_n}\right)$ is the matrix damaged elastic tensor defined as:

$$\tilde{C}_{0_n}^{\text{elD}} = \left(1 - \tilde{D}_{0_n}\right)\tilde{C}_0^{\text{el}}\left(\tilde{E}_0, \tilde{\nu}_0\right).$$ (51)

This procedure is performed for the three different loading conditions, obtaining the matrix damage evolution for each step increment of the three loading conditions.
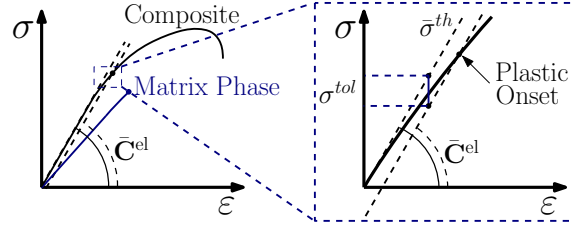

FIGURE 15 Composite yield identification scheme.

Composite plastic onset identification.

The next step consists in identifying the composite plasticity onset stress-strain state ($\tilde{\bar{\sigma}}_y$, $\tilde{\bar{\varepsilon}}_y$) of the three loading conditions used for the parameter identification in order to be able to later characterize the matrix stress-strain state at this point. Using the already identified elastic tensor of the composite $\bar{C}^{\text{el}}$, it is possible to compute a theoretical elastic stress ($\bar{\sigma}_n^{\text{th}}$) of the composite as:

$$\bar{\sigma}_n^{\text{th}} = \bar{C}^{\text{el}} : \bar{\varepsilon}_n.$$ (52)

Due to the complex microstructure that is taken into account, localization points in which plasticity starts developing due to the fibers disposition do not allow to implement a straightforward analytical methodology to find a plasticity onset. As the homogenized composite macro stresses and strains ($\bar{\sigma}$, $\bar{\varepsilon}$) are known at all time steps from the full-field realizations, this theoretical elastic stress allows us to obtain a reference value to compare with these responses obtained from the full-field realizations and be able to assess the amount of plasticity that is developing in the SVE. In order to check when there is a meaningful amount of plasticity developing on the SVE, the plasticity onset is identified by defining a tolerance stress (σ^{tol}), e.g 1 MPa, on the loading component of the composite as shown in Fig. 15. The plasticity onset iteration is then found as the first step satisfying:

$$|\bar{\sigma}_{11_n}| < |\bar{\sigma}_{11_n}^{\text{th}} - \sigma^{tol}|.$$ (53)

It is then possible to define the yield strain $\tilde{\bar{\varepsilon}}_y$ and yield stress $\tilde{\bar{\sigma}}_y$ as the stress-strain state in which the extracted SVE stress-strain curve crosses the tolerance line by using a linear interpolation between the values of σ and ε at the plasticity onset iteration and the previous strain state, such that: ($\bar{\varepsilon}_{n-1} < \tilde{\bar{\varepsilon}}_y < \bar{\varepsilon}_n$) and ($\bar{\sigma}_{n-1} < \tilde{\bar{\sigma}}_y < \bar{\sigma}_n$).

Phases plasticity onset and identification of pressure dependency parameters

At this stage, the known MF-ROM variables are: $\left[\tilde{\nu}_{\text{I}}, \tilde{\text{I}}, \tilde{\theta}, \tilde{E}_0, \tilde{\nu}_0\right]$. In this step, the following variables will be identified: $\left[\tilde{\alpha}, \tilde{m}, \tilde{\sigma}_c^0\right]$. In addition, from the full-field simulations the macro-stressess and -strains ($\bar{\sigma}$, $\bar{\varepsilon}$) are known and from previous steps, the effective damage evolution $\tilde{D}_{0_n}$, and the plastic onset stress-strain state of the composite ($\tilde{\bar{\sigma}}_y$, $\tilde{\bar{\varepsilon}}_y$) are known for the three loading cases.

After identifying the plastic onset stress-strain state of the composite material under the three studied loading conditions, the matrix strain-stress state at the plastic onset ($\varepsilon_{0_{\text{PO}}}$, $\sigma_{0_{\text{PO}}}$) must be obtained, which will allow to have the needed information to compute the pressure-dependent parameters of the MF-ROM. To that end, the matrix strain and stress states at each iteration must be computed up to the identified composite plastic onset. It is important to point out that in order to obtain an accurate representation of the matrix stress-strain state at the plasticity onset of the three loading conditions, the damaged-enhanced nonlinear incremental-secant scheme is used to be able to account for the starting plasticity and damage effects in the matrix phase. Let us consider a time step $\left[t_n, t_{n+1}\right]$:

- First, a virtual elastic unloading is performed. This step unloads the composite up to a stress-free state such that:

$$0 = \bar{\sigma}_n^{\text{res}} = \bar{\sigma}_n - \bar{C}_n^{\text{elD}} : \Delta\bar{\varepsilon}_n^{\text{unload}}.$$ (54)
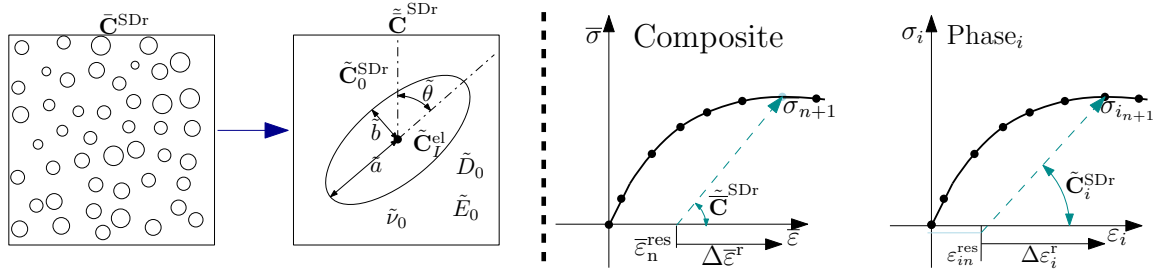
FIGURE 16 Schematic representation of the damaged plastic full-field SVE and its MFH virtual counterpart (left) and schematic loading phase in a stress-strain plot (right).
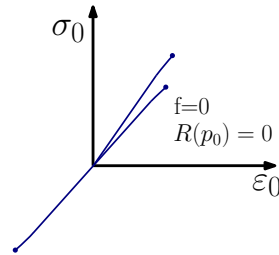

FIGURE 17 Matrix stress-strain curves for uniaxial tension and compression, and biaxial loading up to the plastic onset.

From this expression it is possible to obtain the residual strain tensor, allowing to write the strain increment $\Delta \bar{\varepsilon}^{\mathrm{r}}$ (see Fig. 11) as:

$$\Delta \bar{\varepsilon}^{\mathrm{r}}_{n+1} = \left(\bar{\varepsilon}_{n+1} - \bar{\varepsilon}_n \right) + \bar{C}_n^{\mathrm{elD}-1} : \bar{\sigma}_n. \tag{55}$$

As enough points are obtained from the full-field simulations, it is possible to assume that $\left(D_{0_{n+1}} - D_{0_n} \right) \hat{\sigma}^{\mathrm{res}}_{0_{n+1}} \approx 0$, writing Eq. (33) as:

$$\bar{\sigma}_{n+1} = \bar{C}^{\mathrm{SDr}}_{n+1} : \Delta \bar{\varepsilon}^{\mathrm{r}}_{n+1}. \tag{56}$$

- Then, using Eq. (56), the material is reloaded up to the next composite state, see Fig. 16. Since this stress-strain state is known from the full-field simulation, it is possible to identify the matrix secant tensor C_0^{SDr} by performing the following minimization problem using the definition of the composite secant tensor, Eq. (32), and of the phases, Eqs. (40, 41):

$$\min_{\tilde{\mu}^{\mathrm{Dr}}_s ; \tilde{\kappa}^{\mathrm{Dr}}_s} \left\{ \left\| \tilde{\bar{C}}^{\mathrm{SDr}}_{n+1} \left(\tilde{C}_0^{\mathrm{SDr}} \left(\tilde{\mu}^{\mathrm{Dr}}_s(\tilde{D}_0), \tilde{\kappa}^{\mathrm{Dr}}_s(\tilde{D}_0); \tilde{E}_0, \tilde{\nu}_0 \right); C_{\mathrm{I}}^{\mathrm{el}}, \tilde{\mathrm{I}}, \tilde{\theta}, \upsilon_{\mathrm{I}} \right) : \Delta \bar{\varepsilon}^{\mathrm{r}}_{n+1} - \bar{\sigma}_{n+1} \right\| \right\}. \tag{57}$$

By computing the damaged matrix secant tensor $\tilde{\bar{C}}_0^{\mathrm{SDr}}$ at each step, it is possible to obtain the stress-strain state of each of the phases at each step by using Eq. (31).

Performing consecutive virtual unloadings and loadings until reaching the computed plastic onset, making use of the mean-field homogenization relations shown in Eqs. (25) and (31), the plastic onset state of the matrix phase $(\varepsilon_{0_{\mathrm{PO}}}, \sigma_{0_{\mathrm{PO}}})$ is determined for each of the three loading conditions as shown in Fig. 17.

Once the stress state of the matrix is known at the plastic onset ("PO"), the surrogate model yield surface function f is assumed to have reached a null value. By considering the hardening $R(p_0)$ is small enough to be considered null at this stage, the number of unknowns of the yield surface decreases to three. By minimizing the yield surface equation at this stage for the three tests, it is then possible to identify these three unkonwn parameters: $\tilde{\alpha}$, $\tilde{m}$ and the matrix compressive yield stress $\tilde{\sigma}_c^0$, as:

$$\min_{\tilde{\alpha}, \tilde{m}, \tilde{\sigma}_c^0} \left\{ \sum_{\mathrm{Tests}} \left| f_{\mathrm{PO}}(\tilde{\alpha}, \tilde{m}, \tilde{\sigma}_c^0) \right| = \sum \left| \left(\frac{\left((\hat{\sigma}_{0_{\mathrm{PO}}})^{\mathrm{eq}} \right)^{\tilde{\alpha}}}{\left(\tilde{\sigma}_c^0 \right)^{\tilde{\alpha}}} - 3 \frac{\tilde{m}^{\tilde{\alpha}} - 1}{(\tilde{m}+1)\tilde{\sigma}_c^0} \hat{\phi}_{0_{\mathrm{PO}}} - \frac{\tilde{m}^{\tilde{\alpha}} + \tilde{m}}{\tilde{m}+1} \right) \right| \right\}. \tag{58}$$

Now that $\tilde{\alpha}$, $\tilde{m}$ and $\tilde{\sigma}_c^0$ are identified, all the parameters defining the pressure-dependency of the material are known except the hardening laws. However, assuming the tensile and compressive hardenings are related through parameter $\tilde{m}$ as $\tilde{H}_c = \tilde{m} \tilde{H}_t$, there

is no longer need to use different loading conditions in order to identify the remaining parameters. As explained in the work by Van Dung Nguyen et al.[65], multiple localization bands can appear in the post-peak localization stage, which is considered to be a nonphysical result[68]. This is not the case under tensile loading conditions, for which this condition is valid since in those cases the failure band is perpendicular to the loading direction ([56]), allowing to correctly capture the dissipated energy of the sample during failure. For this reason the uniaxial tension condition will later be the preferred loading condition for the calibration of the post localization onset stage. The uniaxial tension loading condition will therefore be used for the following identification steps.

Starting plastic flow: Initial plastic Poisson's ratio

At this stage, the known MF-ROM variables are: $\left[\tilde{v}_{\mathrm{I}}, \breve{\mathrm{I}}, \tilde{\theta}, \tilde{E}_0, \tilde{v}_0, \tilde{\alpha}, \tilde{m}, \tilde{\sigma}_c^0 \right]$. In this step, the following variables will be identified: $\left[\tilde{v}_p \right]$. Apart from these variables, the macro-stress and strains ($\bar{\sigma}, \bar{\varepsilon}$) and the effective damage evolution $\tilde{D}_0$ are known for all steps. In addition, the phases stress-strain state ($\sigma_0, \varepsilon_0, \sigma_{\mathrm{I}}, \varepsilon_{\mathrm{I}}$) have been computed up to the plastic onset.

Once plasticity is found to be reached, the initial plastic Poisson's ratio of the given SVE can be identified. To that end, the relation between the material parameters $\tilde{\beta}$ and $\tilde{v}_p$, Eq. (36) is used. In order to reduce the source of errors that could be introduced numerically at a specific time step, the following procedure is performed for the first 5 loading increments after the plastic flow onset in order to find an averaged quantity.

Rewriting the incremental-secant scheme, Eq. (33), for the studied case with all identified parameters, it is possible to identify the effective virtual shear and bulk moduli ($\tilde{\mu}_0^{\mathrm{SDr}}, \tilde{\kappa}_0^{\mathrm{SDr}}$) of the matrix (defined in Eq. (41)) through the evaluation of the $\tilde{C}_0^{\mathrm{SDr}}$ tensor using Eqs. (32, 33):

$$\min_{\tilde{\mu}_s^{\mathrm{Dr}}; \tilde{\kappa}_s^{\mathrm{Dr}}} \left\{ \left\| \tilde{C}_{n+1}^{\mathrm{SDr}} \left(\tilde{C}_0^{\mathrm{SDr}} \left(\tilde{\mu}_s^{\mathrm{Dr}}(\tilde{D}_0, \Gamma), \tilde{\kappa}_s^{\mathrm{Dr}}(\tilde{D}_0, \Gamma, \beta); \tilde{E}_0, \tilde{v}_0 \right); C_{\mathrm{I}}^{\mathrm{el}}, \breve{\mathrm{I}}, \tilde{\theta}, v_{\mathrm{I}} \right) : \Delta \bar{\varepsilon}_{n+1}^{\mathrm{r}} - \bar{\sigma}_{n+1} \right\| \right\} . \tag{59}$$

The matrix secant tensor $\tilde{C}_0^{\mathrm{SDr}}$ is known to be isotropic, being possible to write it in terms of $\tilde{\mu}_s^{\mathrm{Dr}}$ and $\tilde{\kappa}_s^{\mathrm{Dr}}$ as $\tilde{C}_0^{\mathrm{SDr}} = 3\tilde{\kappa}_s^{\mathrm{Dr}} I^{\mathrm{vol}} + 2\mu_s^{\mathrm{Dr}} I^{\mathrm{dev}}$, where the plastic bulk and shear moduli write:

$$\tilde{\kappa}_{s_{n+1}}^{\mathrm{Dr}} = \left(1 - \tilde{D}_{0_{n+1}} \right) \left(\kappa^{\mathrm{el}} - \frac{2\beta_{n+1} \kappa^{\mathrm{el}^2} \Gamma_{n+1}}{1 + 2\kappa^{\mathrm{el}} \Gamma_{n+1} \beta_{n+1}} \right) \quad ; \text{ and } \quad \tilde{\mu}_{s_{n+1}}^{\mathrm{Dr}} = \left(1 - \tilde{D}_{0_{n+1}} \right) \left(\mu^{\mathrm{el}} - \frac{6\mu^{\mathrm{el}^2} \Gamma_{n+1}}{1 + 6\mu^{\mathrm{el}} \Gamma_{n+1}} \right) . \tag{60}$$

By solving the system of two equations formed by the definitions of the bulk and shear moduli, the unknown plastic multiplier Γ_{n+1} and the parameter β_{n+1} can be obtained directly as:

$$\Gamma_{n+1} = -\frac{\left(\tilde{D}_{0_{n+1}} - 1 \right) \mu^{\mathrm{el}} + \tilde{\mu}_{s_{n+1}}^{\mathrm{Dr}}}{6\mu^{\mathrm{el}} \tilde{\mu}_{s_{n+1}}^{\mathrm{Dr}}}, \tag{61}$$

$$\beta_{n+1} = -\frac{\kappa^{\mathrm{el}} \left(\tilde{D}_{0_{n+1}} - 1 \right) + \tilde{\kappa}_{s_{n+1}}^{\mathrm{Dr}}}{2\Gamma_{n+1} \tilde{\kappa}_{s_{n+1}}^{\mathrm{Dr}} \kappa^{\mathrm{el}}} . \tag{62}$$

In order to find a unique value of the parameter $\tilde{\beta}$, this is computed as the arithmetic mean of the identified β_i at each loading increment. Once the parameter $\tilde{\beta}$ is computed, the initial plastic Poisson's ratio $\tilde{v}_p$ can be identified as:

$$\tilde{v}_p = \frac{9 - 2\tilde{\beta}}{18 + 2\tilde{\beta}} . \tag{63}$$

Parameters $\tilde{\beta}$ and $\tilde{v}_p$ remain constant for the rest of the identification process.

Fig. 18 shows a flowchart of the inverse identification process up to the plastic flow with all the steps performed separated into the three tested loading conditions.

Plastic flow and damage evolution law up to strain softening onset

At this stage, the known MF-ROM variables are: $\left[\tilde{v}_{\mathrm{I}}, \breve{\mathrm{I}}, \tilde{\theta}, \tilde{E}_0, \tilde{v}_0, \tilde{\alpha}, \tilde{m}, \tilde{\sigma}_c^0, \tilde{v}_p \right]$. In this step, the following variables will be identified: $\left[\tilde{p}_{\mathrm{onset}}, \tilde{D}_{\mathrm{onset}} \right]$. Apart from the MF-ROM variables, it is worth recalling that the macro-stress and strains ($\bar{\sigma}, \bar{\varepsilon}$) and the effective damage evolution $\tilde{D}_0$ are known for all steps, as well as the phases stress-strain states ($\sigma_0, \varepsilon_0, \sigma_{\mathrm{I}}, \varepsilon_{\mathrm{I}}$) up to the plastic onset and the matrix parameters $\tilde{v}_p$ and $\tilde{\beta}$, with $\tilde{v}_p$ and $\tilde{\beta}$ being linked through $\tilde{v}_p = \frac{9 - 2\tilde{\beta}}{18 + 2\tilde{\beta}}$.

Once all the parameters defining the plastic evolution of the material are identified, it is possible to compute the plastic strain evolution of the matrix phase by identifying the matrix damaged secant tensor $\tilde{C}_0^{\mathrm{SDr}}$ using the reloading step of the incremental secant scheme as previously shown. Having identified and fixed the parameter $\tilde{\beta}$, the definition of the shear and bulk moduli,
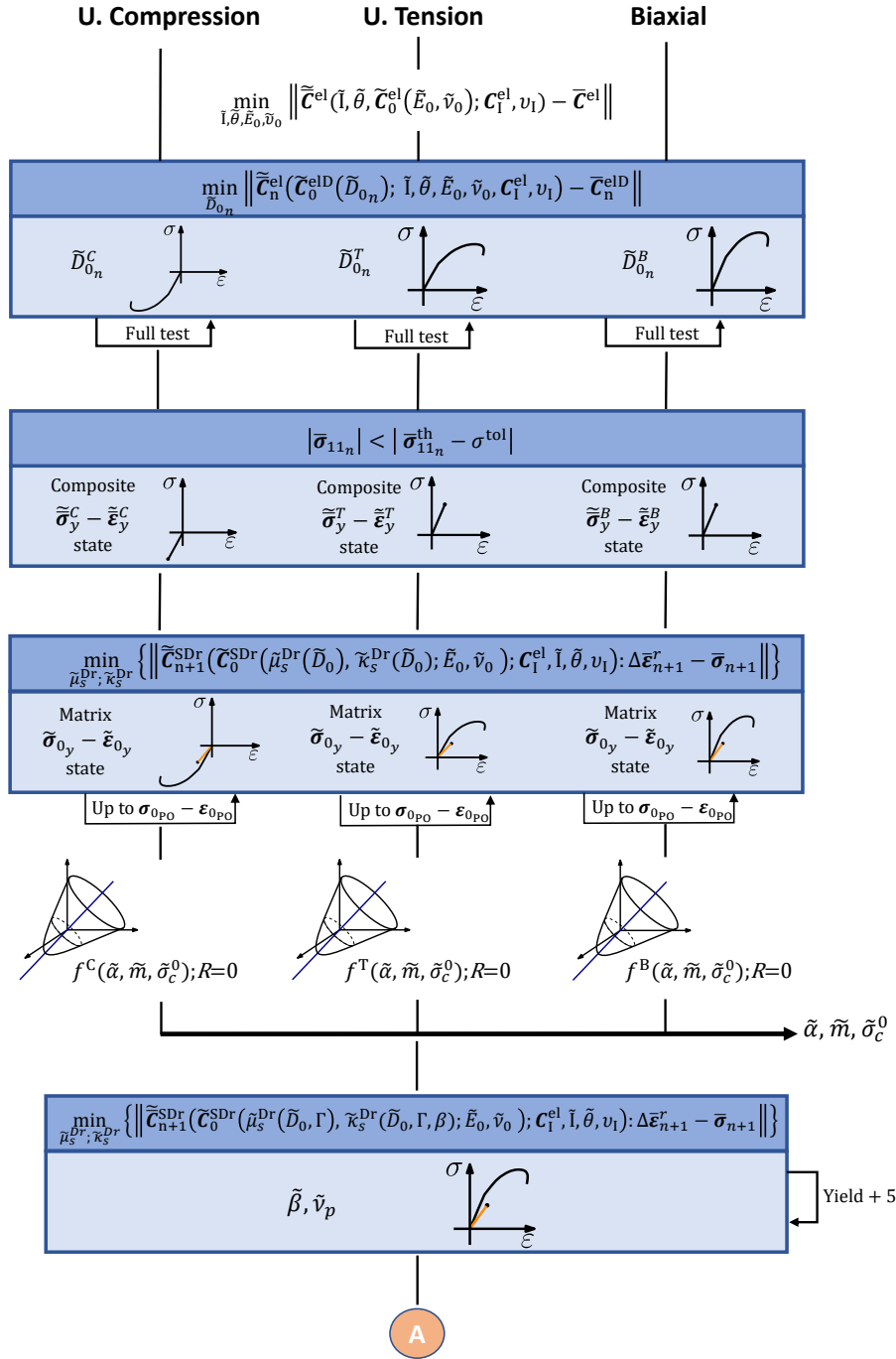
FIGURE 18 Flowchart of the inverse identification process up to plastic flow.

Eq. (41), will now only depend on one unknown: the plastic multiplier Γ through Eq. (61), reducing the evaluation of $\tilde{C}_0^{\text{SDr}}$ to the optimization of Γ. To that end, the following minimization is performed:

$$\min_{\Gamma_{n+1}} \left\{ \left\| \tilde{\bar{C}}_{n+1}^{\text{SDr}} \left(\tilde{C}_0^{\text{SDr}} \left(\tilde{\mu}_s^{\text{Dr}}(\Gamma_{n+1}); \tilde{\kappa}_s^{\text{Dr}}(\Gamma_{n+1}) \right); C_{\text{I}}^{\text{el}}, \tilde{\text{I}}, \tilde{\theta}, \upsilon_{\text{I}} \right) : \Delta \varepsilon_{n+1}^{\text{r}} - \bar{\sigma}_{n+1} \right\| \right\}, \tag{64}$$

Once the plastic multiplier Γ is obtained, the value of the matrix, inclusions and composite secant tensors ($\tilde{C}_0^{\text{SDr}}$, $\tilde{C}_{\text{I}}^{\text{Sr}}$ and $\tilde{C}^{\text{SDr}}$ respectively) are known from Eqs. (32, 40, 41), being possible to compute the stress-strain state of each of the phases for all loading increments (see Fig. 19). This step allows us to identify the matrix localization onset iteration, which is defined as

being the iteration in which the matrix stress reaches its maximum ($|\sigma^{eq}_{0_{n+1}}| \leq |\sigma^{eq}_{0_n}|$) and enters the strain softening phase, see Fig. 20. Once this condition is reached, the iterative process is stopped, since the identification of the post-strain softening region is not needed in terms of the plastic flow evolution information.

As shown in Fig. 19, by identifying the value of the plastic multiplier, it is possible to obtain the increment of the accumulated plastic strain in the matrix $\Delta\tilde{p}_{0_{n+1}}$ from time t_n to t_{n+1} using Eq. (43) as:

$$\Delta\tilde{p}_{0_{n+1}} = \frac{\Gamma_{n+1}}{\sqrt{1+2\tilde{v}_p^2}} \sqrt{6\left(\left(\tilde{\boldsymbol{C}}^{\mathrm{Sr}}_{0_{n+1}} : \Delta\boldsymbol{\varepsilon}^{\mathrm{r}}_{0_{n+1}}\right)^{\mathrm{eq}}\right)^2 + \frac{4}{3}\tilde{\beta}^2\left(\frac{1}{3}\mathrm{tr}\left(\tilde{\boldsymbol{C}}^{\mathrm{Sr}}_{0_{n+1}} : \Delta\boldsymbol{\varepsilon}^{\mathrm{r}}_{0_{n+1}}\right)\right)^2}, \tag{65}$$

where the matrix equivalent increment strain $\left(\Delta\boldsymbol{\varepsilon}^{\mathrm{r}}_0\right)^{\mathrm{eq}}$ is evaluated with the first statistical moment (see Eq. (44)). This accumulated plastic strain increment of the matrix phase allows to approximate the accumulated plastic strain by adding all steps increments $\tilde{p}_{0_{n+1}} = \sum_{l=0}^{n} \Delta\tilde{p}_{0_{l+1}}$.
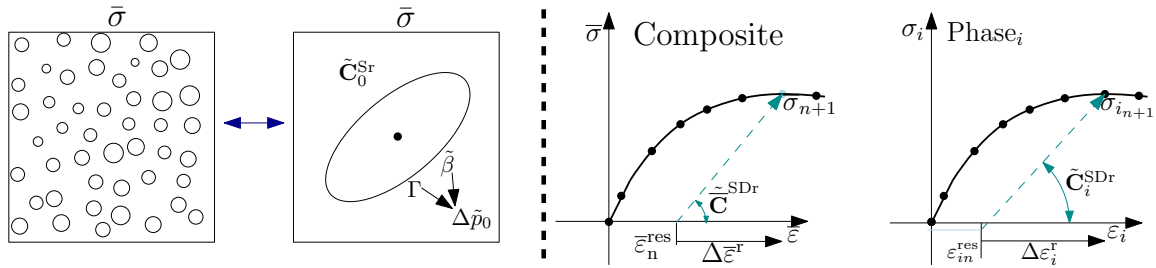
FIGURE 19 Schematic representation of the full-field SVE and its MFH virtual counterpart with computation of the plastic strain evolution (left) and schematic loading phase in a stress-strain plot (right).
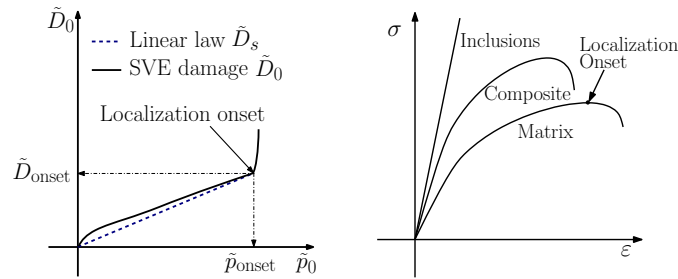
FIGURE 20 Damage-plastic strain plot representing the identified matrix damage from the SVE and the linear approximation used for the MFH surrogate on the left, and graphic representation of the composite, matrix and inclusions stress-strain curves with the location of the localization onset on the right.

A softening damage ($\tilde{D}_s$) evolution law is used to model the matrix damage. In this work, this surrogate model softening damage $\tilde{D}_s$ is simplified to a linear evolution law allowing for an accurate representation of the damage value at the strain softening onset, meaning the maximum stress reached by the composite material and the strain at which it is reached will be accurately represented while simplifying the model. In order to be able to accurately capture the damage state at the beginning of the strain softening onset, the slope of the damage law is defined by the damage ($\tilde{D}_0$) and the accumulated plastic strain ($\tilde{p}_0$) values at the matrix localization onset iteration. These quantities will be called $\tilde{D}_{onset}$ and $\tilde{p}_{onset}$ respectively, see Fig. 20. The evolution law of the softening damage then writes:

$$\Delta\tilde{D}_s = \frac{\tilde{D}_{onset}}{\tilde{p}_{onset}}\Delta\tilde{p}_0. \tag{66}$$

It is worth highlighting that even though the damage representation during this stage does not represent the main focus of this work, a more complex damage evolution law can be easily implemented in future works for a more complete damage representation during this stage.

Hardening identification

At this stage, the known MF-ROM variables are: $\left[\tilde{v}_{\mathrm{I}}, \tilde{\mathrm{I}}, \tilde{\theta}, \tilde{E}_0, \tilde{v}_0, \tilde{\alpha}, \tilde{m}, \tilde{\sigma}_c^0, \tilde{v}_p, \tilde{p}_{\mathrm{onset}}, \widetilde{D}_{\mathrm{onset}}\right]$. In this step, the following variables will be identified: $\left[\check{h}_0, \tilde{h}_1, \tilde{m}_0\right]$. Adding to the known MF-ROM variables, from which the softening damage $\tilde{D}_s(\tilde{p}_{\mathrm{onset}}, \widetilde{D}_{\mathrm{onset}})$ used in this step is defined, previous steps permitted the identification of the stress-strain state of the matrix phase $(\boldsymbol{\sigma}_0, \boldsymbol{\varepsilon}_0)$ for all iterations as well as the plastic strain evolution $\tilde{p}_0$ up to the localization onset .
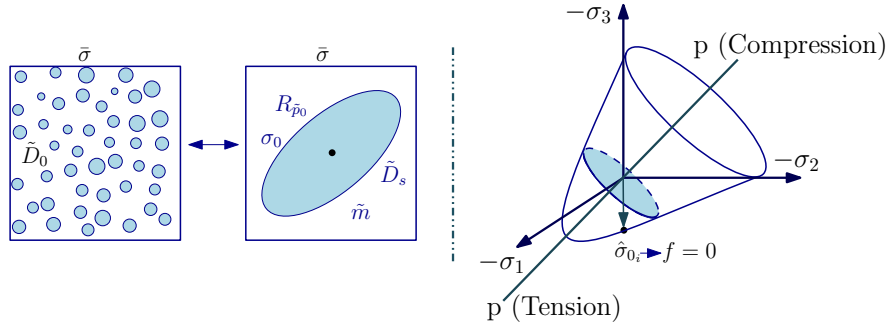
FIGURE 21 Schematic representation of the damaged plastic full-field SVE and its MFH virtual counterpart (left) and yield surface representation in the Haigh-Westergaard coordinate space and effective matrix stress at iteration i (right).

As already mentioned, in this Section the damage evolution law $\tilde{D}_s$ used for the MF-ROM will be defined and the hardening evolution of the matrix will be identified. The effective von Mises stress of the matrix phase can be computed using the first statistical formula, Eq. 44. As plastic flow occurs during the full loading, the yield function f has a null value at all steps, see Fig. 21.

Knowing the matrix stress and strain states at each loading increment, as well as the accumulated plastic strain evolution, it is then possible to identify the matrix effective hardening evolution $R_0\left(\tilde{p}_0\right)$ up to the strain softening onset at time n by minimizing the yield surface function f at each iteration:

$$
\min_{R_{n+1}\left(\tilde{p}_{0_{n+1}}\right)}\left\{\left|f_{n+1}\left(R_{n+1}\left(\tilde{p}_{0_{n+1}}\right)\right)=\frac{\left((\hat{\sigma}_{0_{n+1}})^{\mathrm{eq}}\right)^{\tilde{\alpha}}}{\left(\sigma_c^0+R_{n+1}\left(\tilde{p}_{0_{n+1}}\right)\right)^{\tilde{\alpha}}}-3\frac{\tilde{m}^{\tilde{\alpha}}-1}{(\tilde{m}+1)\left(\sigma_c^0+R_{n+1}\left(\tilde{p}_{0_{n+1}}\right)\right)}\hat{\phi}_{0_{n+1}}-\frac{\tilde{m}^{\tilde{\alpha}}+\tilde{m}}{\tilde{m}+1}\right|\right\},
\tag{67}
$$

where the effective stress is computed with the identified softening damage evolution $\tilde{D}_s$, such that:

$$
\hat{\boldsymbol{\sigma}}_{0_{n+1}}=\frac{\boldsymbol{\sigma}_{0_{n+1}}}{\left(1-\tilde{D}_{s_{n+1}}\right)}.
\tag{68}
$$

The use of the softening damage evolution law allows slightly increasing the accuracy of the MF-ROM, as it permits to compute the effective hardening evolution accounting for the damage law simplification.

Once the effective hardening evolution is computed, it is possible to identify the parameters $(\tilde{H})$ governing the dedicated evolution law $\tilde{R}_0(\tilde{p}_{0_n}, \tilde{H})$ used for the MFH model in order to fit the computed evolution. In order to identify the hardening parameters that best suit a given SVE, a curve fitting problem is performed using the previously computed hardening evolution $R_n(\tilde{p}_{0_n})$.

$$
\min_{\tilde{H}}\left\{\sum_n\left|R_n(\tilde{p}_{0_n})-\tilde{R}_0(\tilde{H}, \tilde{p}_{0_n})\right|\right\}.
\tag{69}
$$

In this paper, a linear exponential law is used in order to model this evolution:

$$
\tilde{R}_0\left(p_0\right)=\check{h}_0\tilde{p}_0+\tilde{h}_1\left(1-e^{-\tilde{m}_0\tilde{p}_0}\right).
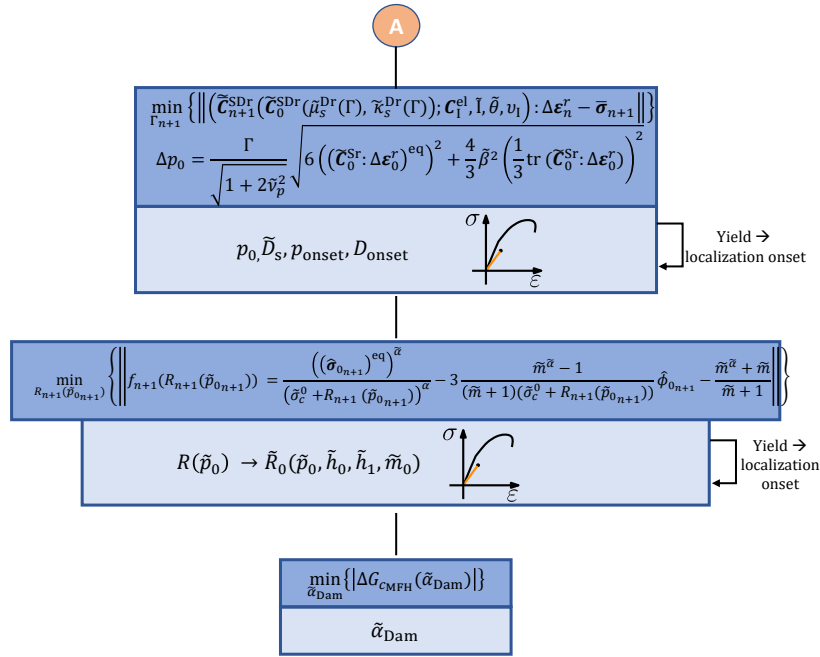\tag{70}
$$

FIGURE 22 Flowchart of the inverse identification process during plastic flow.

With this evolution model, the set of hardening parameters $(\tilde{H})$ that need to be identified consists of h_0, h_1 and m_0, which will be part of the set of random quantities in the final MFH-ROM. It is worth highlighting that this hardening identification process is applied up to the strain-softening onset, as the introduction of the post-strain softening onset would introduce spurious information due to the localization effects. A flowchart of the plastic flow stage identification process is shown in Fig. 22.

The identification process presented in this Section allows obtaining an accurate representation of the SVE behavior under different loading conditions independently of the SVE characteristics. A direct comparison between the response obtained with the full-field SVE realizations and its identified MFH counterpart for the three tested loading conditions, see Fig. 6, is shown in Fig. 23. As already observed in the work by Wu et al.[53], the identified matrix behavior differs from the SVE matrix material. This is observed in the comparison between the tensile hardening evolution curves obtained from the identification process of different SVE and the epoxy hardening law used to model the matrix behavior in the full-field realizations, see Fig. 23.

The capability of the identified surrogate model to capture the SVE behavior under a different loading to those used for the inverse process was checked by testing its performance under shear loading. We however note that the use of periodic boundary conditions for the cases different from tensile ones is debatable as discussed in Section 2.2. As seen in the results shown in Fig. 24, the MFH model yields less accurate results than for the previously tested loading conditions, however the MFH simulations predict the composite strength within a 10% error. Different loading modes should be considered during the identification process in order to reduce this error, but that would imply, on the one hand to increase the number of parameters of the MF-ROM –for example by considering different hardening laws in tension and compression, and on the other hand to consider unsupervised learning for the parameters identification to account for several loading cases altogether –for example using a Bayesian Inference (BI) process as in[93].

3.2.3 | Nonlinear damage-enhanced elasto-plastic composites accounting for loss of objectivity during local softening

At this stage, the known MF-ROM variables are: $\left[\tilde{v}_I, \tilde{I}, \tilde{\theta}, \tilde{E}_0, \tilde{v}_0, \tilde{\alpha}, \tilde{m}, \tilde{\sigma}_c^0, \tilde{v}_p, \tilde{p}_{\text{onset}}, \widetilde{D}_{\text{onset}}, \tilde{h}_0, \tilde{h}_1, \tilde{m}_0\right]$. In this step, the following variables will be identified: $\left[\tilde{\alpha}_{\text{Dam}}, \tilde{\beta}_{\text{Dam}}\right]$. At this step, the critical energy release rate extracted from the full-field realization $G_{c_{\text{SVE}}}$ will be used for the calibration of the failure stage damage law.

Up to now, the loss of objectivity that is encountered once the onset of strain softening occurs has not been taken into account. To that end, the energy release rate is used as objective value that will allow the recovery of the size objectivity ([56],[71]). In order to
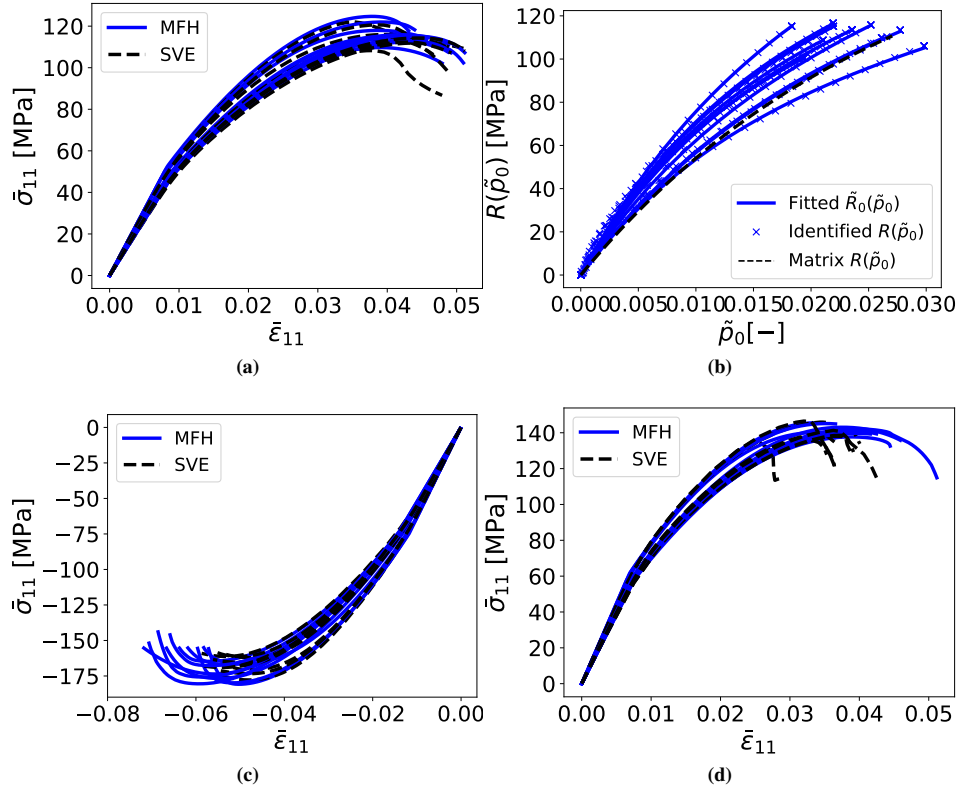
FIGURE 23 (a) Stress-strain curves of random picked SVEs under uniaxial tension. (b) Comparison between epoxy tensile hardening law and the identified hardening evolution. (c) Stress-strain curves of random picked SVEs under uniaxial compression. (d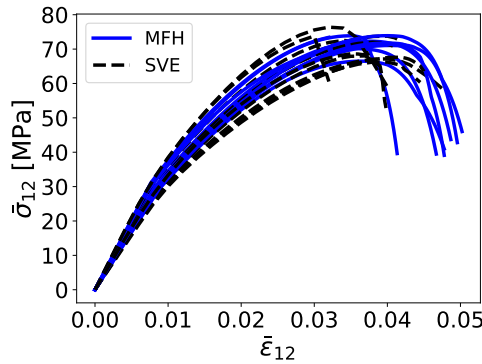) Stress-strain curve of random picked SVEs under biaxial tension. MFH stands for the results obtained with the surrogate model. SVE stands for the results obtained in the full-field SVE realizations. The Identified and Fitted $\tilde{R}_0\left(\tilde{p}_0\right)$ stand for the identified surrogate matrix hardening law. The Matrix $\tilde{R}_0\left(\tilde{p}_0\right)$ stands for the hardening law used in the full-field SVE realizations.

FIGURE 24 Stress-strain curves of random picked SVEs under shear loading. MFH stands for the results obtained with the surrogate model. SVE stands for the results obtained in the full-field SVE realizations.

estimate the critical energy release rate associated to the MFH model, similarly to the approach used in the publications ([56],[59]), a uniaxial test with a loading direction perpendicular to the UD composite fiber orientation is performed on a 2D specimen with length L ten times bigger than the characteristic length l used in the MFH model and width W four times smaller than the characteristic length of homogenized composite material (see Fig. 25). A slight decrease of the bar diameter in its center is

introduced through a curvature with radius R in order to generate a localization of the deformation while not affecting the pre-localization response of the material. A thorough convergence study of the solution with respect to the mesh was performed in order to ensure a correct identification of the energy release values.
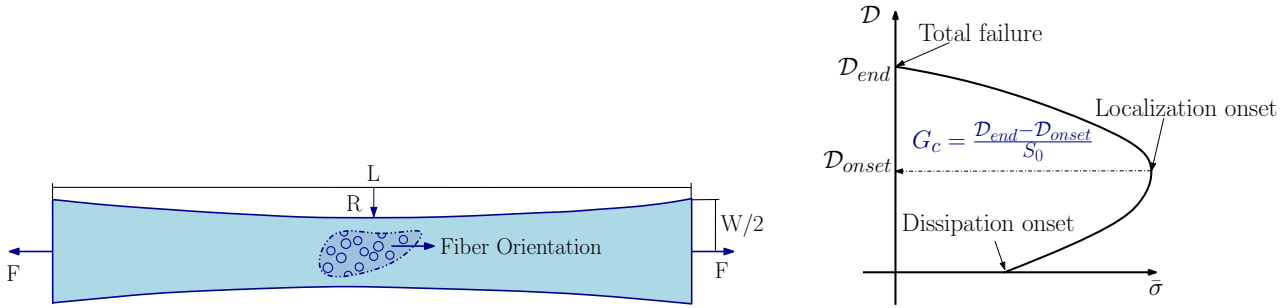
FIGURE 25 Schematic representation of the uniaxial test on the left and energy dissipation ($\mathcal{D}$) - stress ($\bar{\sigma}$) plot used for the computation of the MFH energy release rate G_c.

The failure stage of the composite response is considered to be started once $\tilde{p}_0 > \tilde{p}_{onset}$. In order to be able to control the failure characteristics of the material, a new failure damage (D_f) contribution is introduced in the MFH surrogate model. This failure damage evolution law writes:

$$\Delta \tilde{D}_f = \tilde{\alpha}_{\mathrm{Dam}} \left(\tilde{p}_0 + \Delta \tilde{p}_0 - \tilde{p}_{onset} \right)^{\beta_{Dam}}, \quad \text{if} \quad \tilde{p}_0 > \tilde{p}_{onset}. \tag{71}$$

The total damage of the surrogate model during this post-strain softening point is then defined by the sum of both damage components: $\Delta \tilde{D}_{\mathrm{MFH}} = \Delta \tilde{D}_s + \Delta \tilde{D}_f$. As can be observed in Eq. (71), the failure damage evolution depends on two new parameters: $\tilde{\alpha}_{\mathrm{Dam}}$ and $\tilde{\beta}_{\mathrm{Dam}}$. These parameters will affect the ductility of the material, see Fig. 26, changing the resultant energy release rate. In this paper, $\tilde{\beta}_{\mathrm{Dam}}$ was fixed to a value of 2.5 [−], value for which realistic behaviour for a wide range of G_c was obtained, allowing to reduce the optimization problem to a one-DOF problem. Furthermore, the characteristic length l introduced used for the definition of c_g (see Eq. 14) with the use of the nonlocal formulation of the damage, was fixed to a value of 25 μm, so the value of the energy release rate will only depend on the post-strain softening damage characteristics of the composite material.
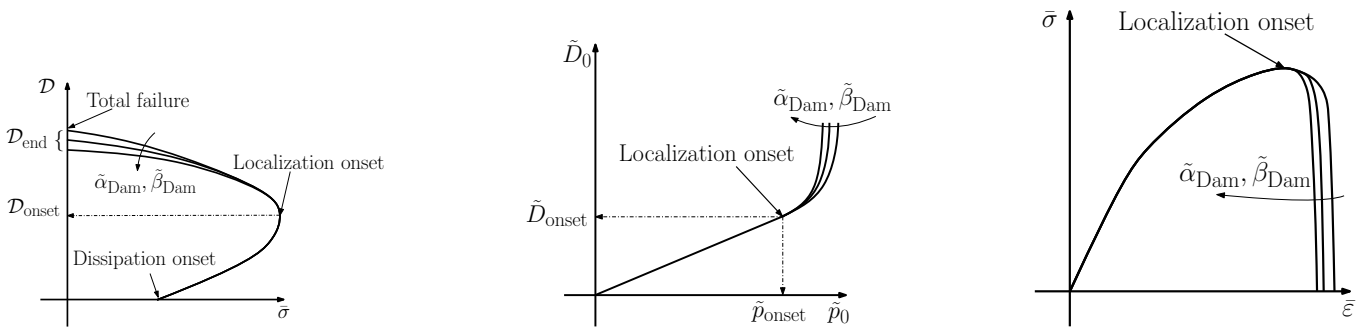
FIGURE 26 Schematic representation of the composite energy dissipation ($\mathcal{D}$) - stress ($\bar{\sigma}$) plot, the matrix damage evolution law with respect to its accumulated plastic strain and the composite averaged $\sigma - \varepsilon$ curve and the effect of the failure damage evolution law parameter ($\tilde{\alpha}_{\mathrm{Dam}}$) on each respective graph.

After the matrix softening strain onset is reached, the identification of the post-strain softening damage evolution law parameter ($\tilde{\alpha}_{\mathrm{Dam}}$) is performed through an iterative process, in which the energy release rate obtained with the full-field SVE simulation is recovered with its MFH model counterpart. These model parameters are then found through the following minimization
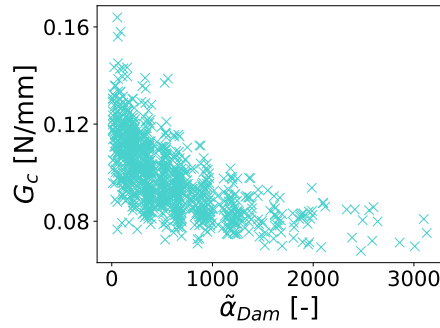
FIGURE 27 $G_c - \tilde{\alpha}_{\mathrm{Dam}}$ distribution for the $25 \times 25 \ \mu\mathrm{m}^2$ SVE realizations.

problem:

$$\min_{\tilde{\alpha}_{\mathrm{Dam}}} \left\{ \left| \Delta G_{c_{\mathrm{MFH}}} \left(\tilde{\alpha}_{\mathrm{Dam}} \right) \right| \right\}, \tag{72}$$

where $\Delta G_{c_{\mathrm{MFH}}} \left(\tilde{\alpha}_{\mathrm{Dam}} \right) = G_{c_{\mathrm{MFH}}} \left(\tilde{\alpha}_{\mathrm{Dam}} \right) - G_{c_{\mathrm{SVE}}}$.

An initial guess value for $\tilde{\alpha}_{\mathrm{Dam}}$ is used to start the iterative process, in which a finite element simulation from which the energy release rate $G_{c_{\mathrm{MFH}}}$ will be computed is performed at each iteration as shown by Fig. 25. Once the energy release rate is obtained, this value is compared to the SVE realization energy release rate, being possible to implement an algorithm capable of finding a better guess of the set of parameters of the damage model for the next iteration. As shown by Fig. 26, a change in the matrix damage evolution law modifies the failure characteristics of the homogenized composite material response. This change in the failure characteristics has a direct impact in the dissipated energy after the localization onset, modifying the characteristic energy release rate of the studied material. This iterative process is performed until minimizing the $\left(\Delta G_{c_{\mathrm{MFH}}} \left(\tilde{\alpha}_{\mathrm{Dam}} \right) \right)$ below a fixed tolerance value. In this work, this tolerance is fixed to be 2% of the reference value $G_{c_{\mathrm{SVE}}}$, such that $\Delta G_{c_{\mathrm{MFH}}} \leq \text{tolerance} = 0.02 \cdot G_{c_{\mathrm{SVE}}}$. In the case reaching this tolerance would not be possible for a given SVE realization, the results of that realization would not be taken into account in the final data.

As the resultant effect of $\tilde{\alpha}_{\mathrm{Dam}}$ on the energy release rate $G_{c_{\mathrm{SVE}}}$ also depends on all other parameters defining the surrogate model, a direct relation between $G_{c_{\mathrm{SVE}}}$ and $\tilde{\alpha}_{\mathrm{Dam}}$ cannot be found explicitly as shown in Fig. 27, being necessary to iterate this optimization problem until reaching a sufficiently low error $\Delta G_{c_{\mathrm{MFH}}}$. Fig. 28 shows a scheme of the optimization algorithm used to identify the parameter $\tilde{\alpha}_{\mathrm{Dam}}$ through a flowchart.

4 | STOCHASTIC MF-ROM FOR UD COMPOSITE MATERIAL

After the presentation of the identification process, this section will start with a study of the statistical properties of the identified effective random parameters used to define the MF-ROM. Then, the data-driven sampling method [94] used for the generation of proper random fields for the construction of the structural stochastic FEM [53] will be presented.

4.1 | Analysis of the MF-ROM effective random parameters

As shown in Section 3, a total of 16 effective random parameters is needed for the definition of the MF-ROM. These random parameters constitute the vector $\boldsymbol{\beta}^D$ ($n = 16$) (Eq. 48). A vector of 16 parameters is therefore identified for each SVE realization, meaning as many vectors $\boldsymbol{\beta}^D$ as SVE realizations are obtained. Fig. 29 shows the different distributions of the random effective material parameters obtained from the inverse identification process for the case with $25 \times 25 \ \mu\mathrm{m}^2$ and $45 \times 45 \ \mu\mathrm{m}^2$ by plotting their respective probability density histograms. It is possible to observe how in general, the parameters using the $45 \times 45 \ \mu\mathrm{m}^2$ SVE present less widespread values of the effective random parameters, which is reflected in higher maximums of the probability density histograms, due to the higher size of the SVE. This lower standard deviation allows reducing the number of SVE realizations needed to obtain the complete distribution of the effective parameters compared to the $25 \times 25 \ \mu\mathrm{m}^2$ case. However, the effect of this lower heterogeneity of the effective parameter values is still to be verified afterwards during the verification of the MF-ROM performance. The probability density distribution of the rest of the effective random parameters can be found in Appendix D.
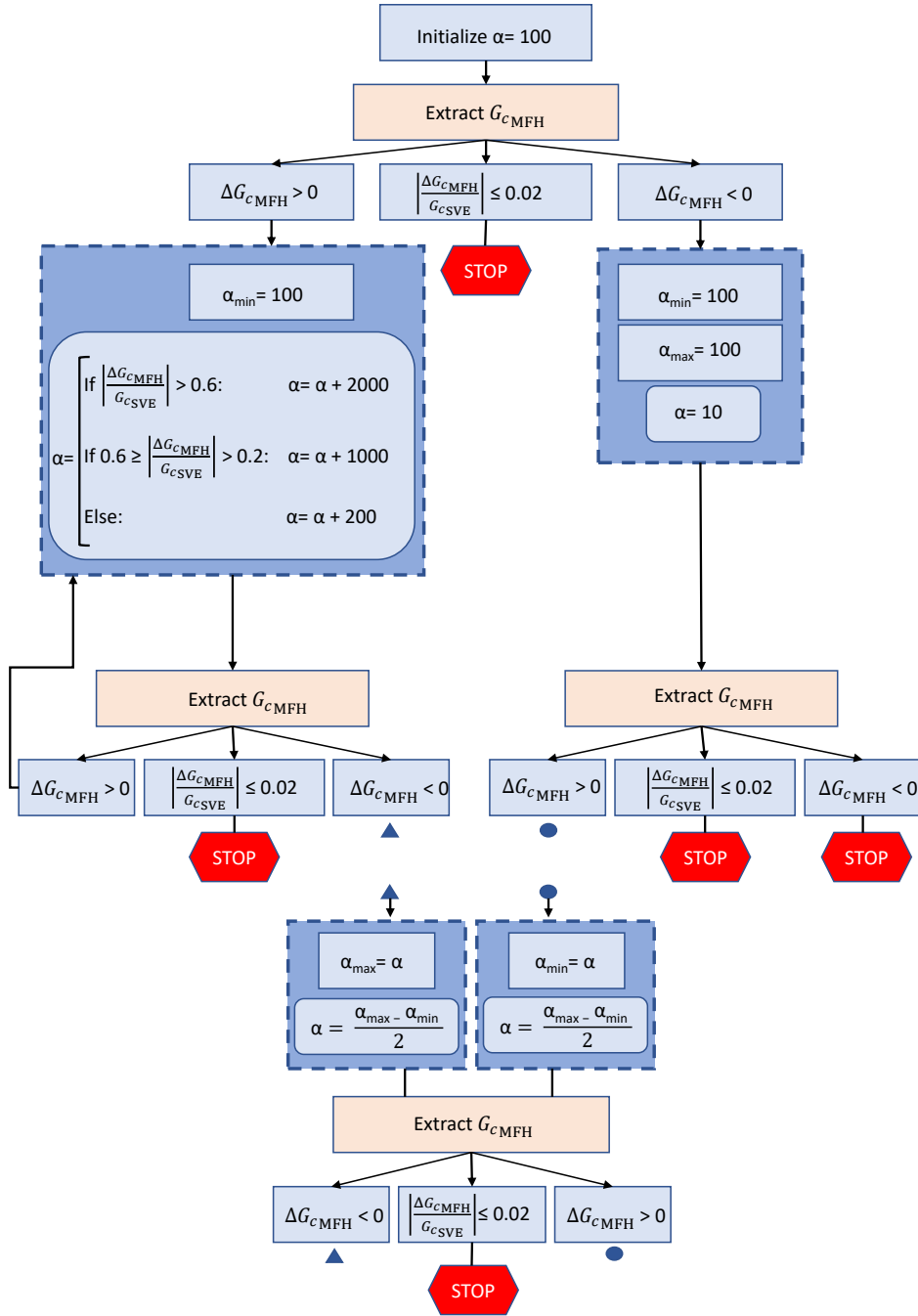
FIGURE 28 Flowchart of the optimization process of parameter $\tilde{\alpha}_{\mathrm{Dam}}$ for the recovery of the size objectivity through the energy release rate.

As in the elasto-plastic case[53], the effective random parameters used to build the damage-enhanced pressure-dependent MF-ROM show a clear cross-dependence, as shown by the distance correlation[95] values obtained in Figs. 30 and 31. This cross-dependence between the effective random parameters must be preserved by the data-driven sampling method in order to yield an accurate result when using the MF-ROM.

4.2 | **Generation of random parameters**

This section will start by briefly introducing the data-driven sampling method presented in [94] and used for a stochastic MF-ROM in the works [53], method that will serve in this work to generate new data from the obtained data-set through the identification process, and will then discuss the obtained identified and generated data-sets that will be used to build the stochastic structural FEM.

The data-driven sampling method developed by G. Soize and R. Ghanem [94] is used for the generation of proper random fields. This method accounts for the random properties of the material, which are defined in a probability space $(\Theta, \mathcal{T}, \mathcal{P})$ with a given value in $\mathbb{R}^n$ through a random vector whose statistic information is supposed to belong to a subset $\mathcal{S}^n$ of $\mathbb{R}^n$ but its distribution is unknown.

The random matrix $[\beta^D] = [\beta_1^D, ..., \beta_N^D]$ with value in $\mathcal{M}_{n,N}$, where each column is an independent copy of the random vector defined in the space $(\Theta, \mathcal{T}, \mathcal{P})$, allows preserving the local structure of the data-set. In our case, the identification process permits us to obtain a matrix $[b] = [b_1, ..., b_N]$, which is a realization of matrix $[\beta^D]$ with a size of $N = 1037$ for the $25 \times 25 \mu m^2$ SVE case and with a size of $N = 803$ for the $45 \times 45 \mu m^2$ SVE case. The information contained in the matrix $[b]$ allows then to generate n_{MC} new realizations of the random matrix $[\beta^D]$ thanks to a Markov Chain Monte Carlo (MCMC) process. To that end, first the mean is removed from the data-set values and a normalization of the variance is carried out, being then possible to generate a new random data-set. Once the new data is generated, this is re-scaled to the original data-set scale, obtaining the final data. This process is summarized in ([53]).

Figs. 32, 33 and 34 present visually a direct comparison between the generated data and the identified data-set. The number of needed realizations of the random vector β^D can vary with the application. The size of the studied geometry, or the number of desired stochastic simulations could increase or decrease the needed amount of stochastic information, meaning a larger set of realizations may be required. In this work, a value of $n_{MC} = 24$ was used in the generation of the new data-set for the $25 \times 25 \mu m^2$ SVE case, meaning that a total of 24888 realizations are generated from the original data-set of 1037 SVE realizations. These plots show an excellent agreement between the identified and the generated distributions. Similar results were obtained for the $45 \times 45 \mu m^2$ SVE case, in which a value of $n_{MC} = 29$ was used since less realizations were obtained from the full-field simulations, obtaining a total of 23287 realizations of the random vector β^D. As already observed with the distance correlation between the different effective random parameters, a cross-dependence between the different effective random parameters can be observed. It is worth mentioning the ability of the generator to successfully capture the different distributions of the different parameters. Similar results were obtained for the $45 \times 45 \mu m^2$ SVE, whose results are presented in Appendix E.
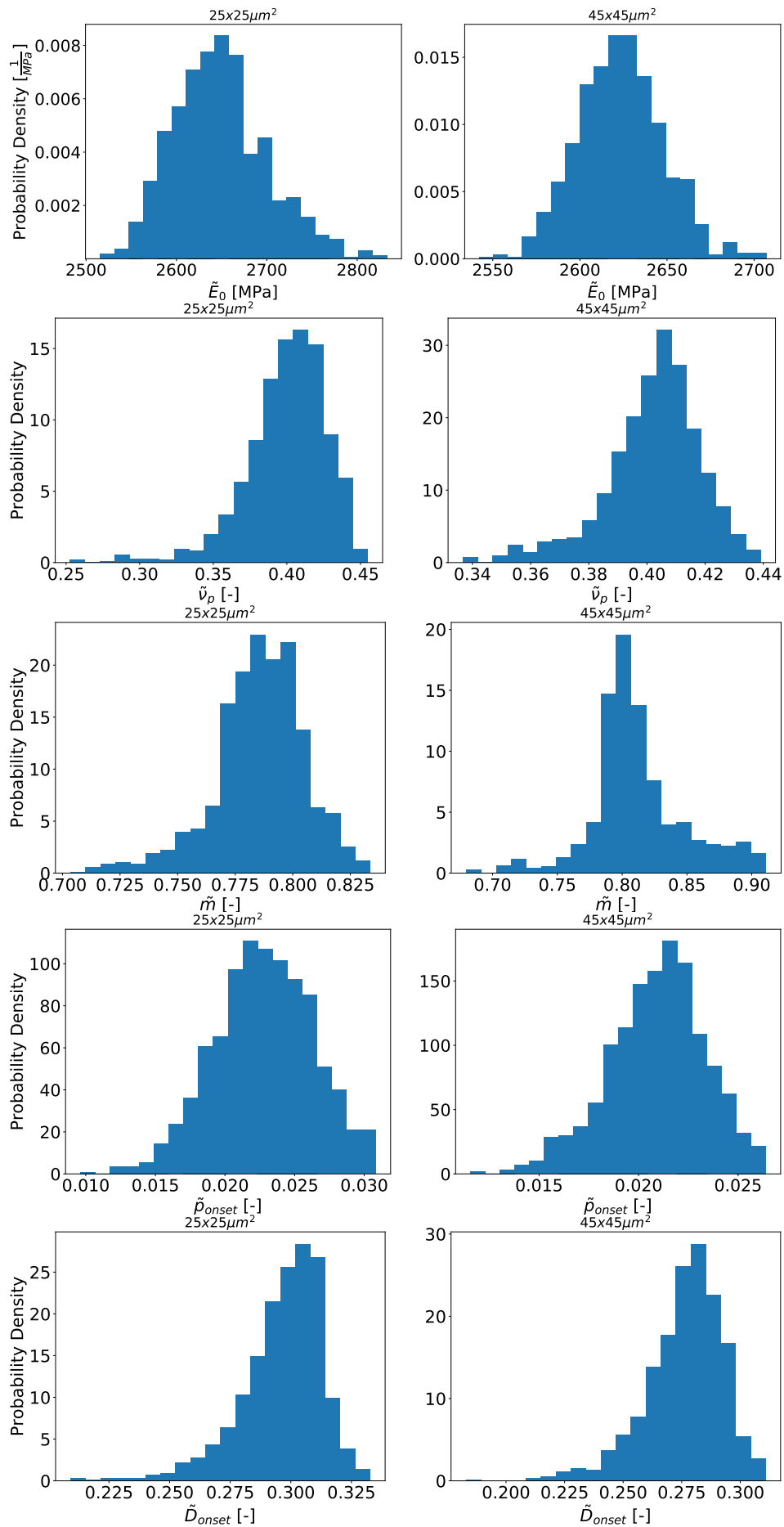
FIGURE 29 Probability density histograms of $\tilde{E}_0$, $\tilde{\nu}_p$, $\tilde{m}$, $\tilde{p}_{\mathrm{onset}}$ and $\tilde{D}_{\mathrm{onset}}$ for the $25 \times 25 \mu m^2$ (left) and $45 \times 45 \mu m^2$ (right) SVE cases.

$\tilde{v}_I$	$\widetilde{\theta}$	$\tilde{I}$	$\widetilde{E}_0$	$\tilde{v}_0$	$\tilde{\sigma}_c^0$	$\tilde{h}_0$	$\tilde{h}_1$	$\widetilde{m}_0$	$\widetilde{m}$	$\tilde{\alpha}$	$\tilde{v}_p$	$\tilde{p}_{onset}$	$\widetilde{D}_{onset}$	
0.152	0.131	0.093	0.146	0.140	0.195	0.303	0.115	0.094	0.110	0.077	0.092	0.216	0.350	$\tilde{\alpha}_{Dam}$
	0.052	0.164	0.593	0.739	0.109	0.073	0.218	0.076	0.188	0.078	0.169	0.091	0.071	$\tilde{v}_I$
		0.107	0.038	0.041	0.319	0.074	0.094	0.125	0.146	0.094	0.079	0.096	0.070	$\widetilde{\theta}$
			0.046	0.048	0.228	0.054	0.059	0.052	0.077	0.048	0.098	0.045	0.050	$\tilde{I}$
				0.938	0.330	0.118	0.291	0.123	0.228	0.081	0.222	0.259	0.182	$\widetilde{E}_0$
					0.311	0.104	0.294	0.121	0.279	0.074	0.234	0.224	0.156	$\tilde{v}_o$
						0.061	0.452	0.085	0.099	0.226	0.039	0.307	0.077	$\tilde{\sigma}_c^0$
							0.631	0.510	0.108	0.104	0.079	0.172	0.232	$\tilde{h}_0$
								0.312	0.234	0.068	0.469	0.453	0.093	$\tilde{h}_1$
									0.477	0.328	0.347	0.469	0.350	$\widetilde{m}_0$
										0.750	0.380	0.372	0.153	$\widetilde{m}$
											0.132	0.081	0.074	$\tilde{\alpha}$
												0.713	0.107	$\tilde{v}_p$
													0.536	$\tilde{p}_{onset}$

FIGURE 30 Distance correlation of the effective random material parameters of the $25 \times 25 \mu m^2$ SVEs.

$\tilde{v}_I$	$\widetilde{\theta}$	$\tilde{I}$	$\widetilde{E}_0$	$\tilde{v}_0$	$\tilde{\sigma}_c^0$	$\tilde{h}_0$	$\tilde{h}_1$	$\widetilde{m}_0$	$\widetilde{m}$	$\tilde{\alpha}$	$\tilde{v}_p$	$\tilde{p}_{onset}$	$\widetilde{D}_{onset}$	
0.094	0.105	0.080	0.127	0.098	0.088	0.340	0.197	0.158	0.070	0.067	0.134	0.217	0.334	$\tilde{\alpha}_{Dam}$
	0.067	0.066	0.589	0.739	0.084	0.060	0.096	0.091	0.134	0.123	0.083	0.053	0.076	$\tilde{v}_I$
		0.155	0.070	0.066	0.240	0.071	0.145	0.146	0.147	0.134	0.094	0.076	0.070	$\widetilde{\theta}$
			0.061	0.073	0.174	0.063	0.072	0.074	0.060	0.056	0.119	0.059	0.061	$\tilde{I}$
				0.928	0.234	0.063	0.162	0.158	0.270	0.228	0.088	0.193	0.213	$\widetilde{E}_0$
					0.204	0.066	0.151	0.147	0.249	0.213	0.101	0.143	0.178	$\tilde{v}_o$
						0.076	0.454	0.122	0.752	0.779	0.100	0.102	0.065	$\tilde{\sigma}_c^0$
							0.612	0.680	0.265	0.189	0.082	0.097	0.181	$\tilde{h}_0$
								0.500	0.365	0.372	0.210	0.184	0.092	$\tilde{h}_1$
									0.323	0.211	0.246	0.391	0.249	$\widetilde{m}_0$
										0.954	0.095	0.136	0.096	$\widetilde{m}$
											0.069	0.094	0.091	$\tilde{\alpha}$
												0.509	0.061	$\tilde{v}_p$
													0.717	$\tilde{p}_{onset}$

FIGURE 31 Distance correlation of the effective random material parameters of the $45 \times 45 \mu m^2$ SVEs.

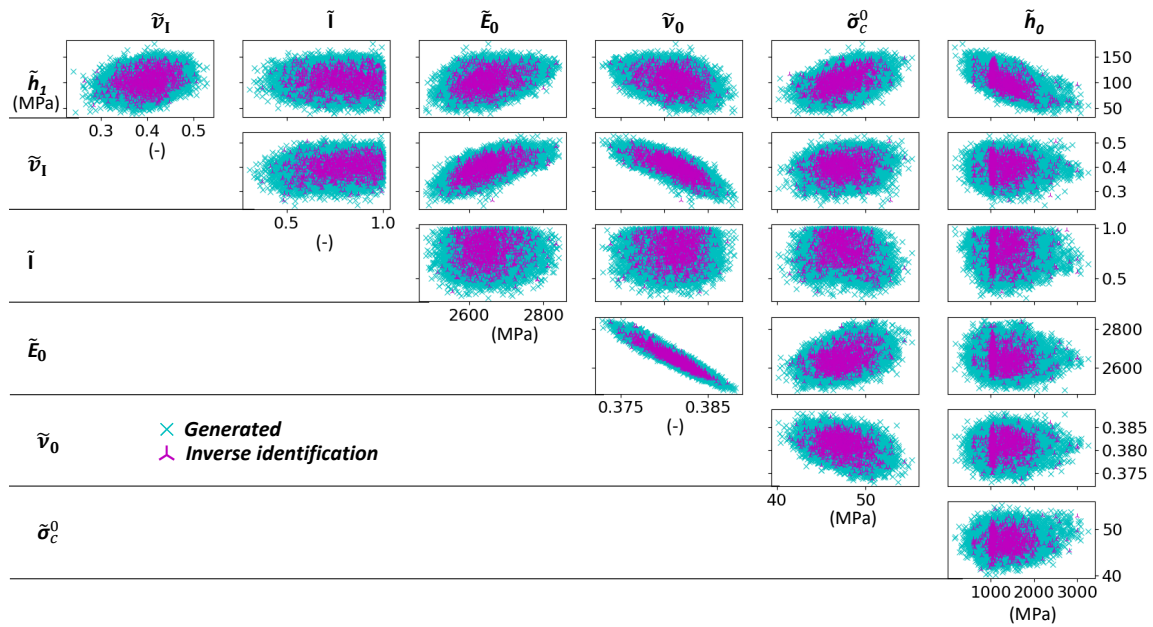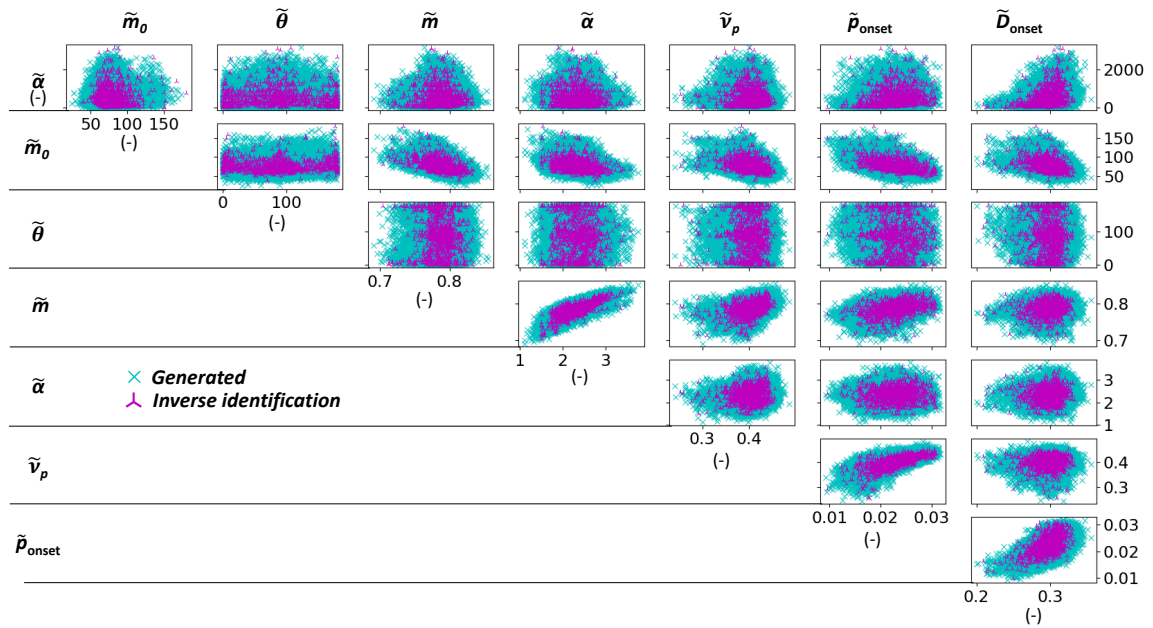**FIGURE 32** $25 \times 25 \mu m^2$ effective random parameters distributions and their cross-dependence for the identified and generated $\tilde{v}_I, \tilde{I}, \tilde{E}_0, \tilde{v}_0, \tilde{\sigma}_c^0, \tilde{h}_0$ and $\tilde{h}_1$.

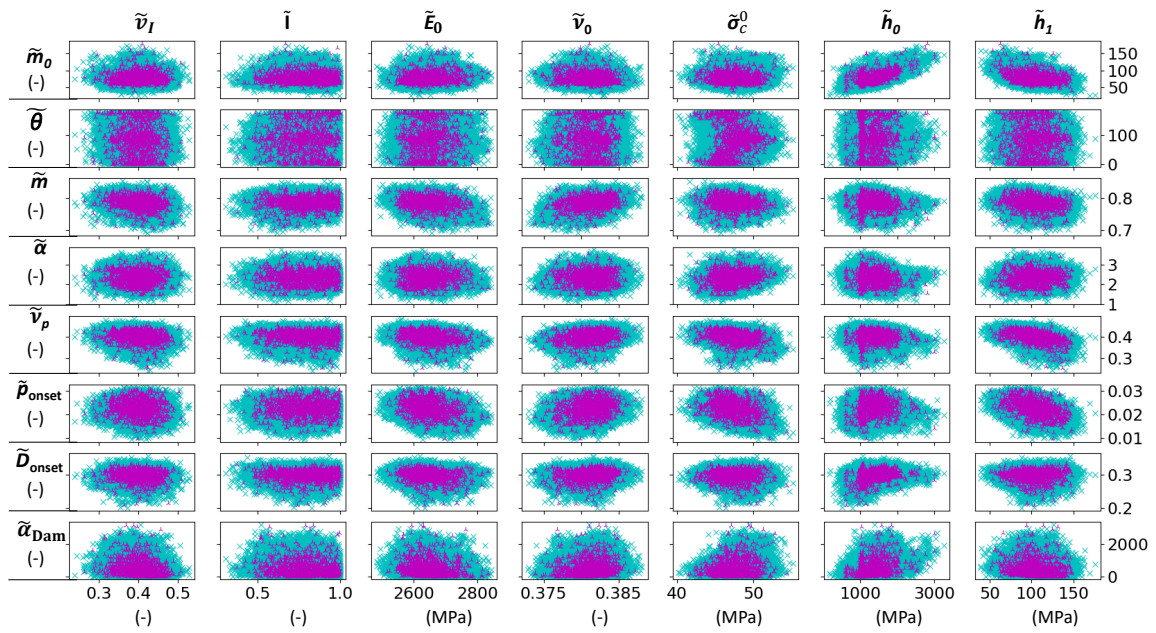**FIGURE 33** $25 \times 25 \mu m^2$ effective random parameters distributions and their cross-dependence for the identified and generated $\tilde{m}_0, \tilde{\theta}, \tilde{m}, \tilde{v}_p, \tilde{\alpha}, \tilde{p}_{\text{onset}}, \widetilde{D}_{\text{onset}}$ and $\tilde{\alpha}_{\text{Dam}}$.

FIGURE 34 $25 \times 25 \mu \mathrm{m}^2$ effective random parameters distributions and their cross-dependence for the identified and generated $\tilde{v}_\mathrm{I}, \tilde{\mathrm{I}}, \tilde{\theta}, \tilde{E}_0, \tilde{v}_0, \tilde{\sigma}_c^0, \tilde{h}_0, \tilde{h}_1, \tilde{m}_0, \tilde{m}, \tilde{v}_p, \tilde{\alpha}, \tilde{p}_{\mathrm{onset}}, \widetilde{D}_{\mathrm{onset}}$ and $\tilde{\alpha}_{\mathrm{Dam}}$.

5 | APPLICATION OF THE STOCHASTIC MF-ROM

Now that the data-set used to build the stochastic MF-ROM and the modeling strategy are presented, this section will directly test the performance of the ROM by comparing its results against full-field simulations and experimental results.

In order to test the consistency of the developed methodology, the two constructed MF-ROMs, one built with the $25 \times 25 \mu m^2$ SVEs and the other built with the $45 \times 45 \mu m^2$ SVEs are tested as input of the stochastic finite element simulations. As shown in Fig. 35, the random fields of the effective parameters, which are different realizations of the random vector $\boldsymbol{\beta}^D$, are discretized in squares with the same size as the SVEs used to construct the used MF-ROM, i.e. $25 \times 25 \mu m^2$ or $45 \times 45 \mu m^2$, determining the distribution of different effective random parameters on the integration points. Following the methodology developed in ([7], [53]), due to the vanishing of the spatial correlation, the effective random parameters used at each random field discretization are independent of the parameters of adjacent squares. As in [7,53], smooth step functions are used at the random field discretization, avoiding possible artificial effects that could be introduced due to sharp changes in the material properties. The finite element discretization of the tested sample is performed with a mesh performed with quadratic elements whose characteristic size must be smaller than the random field discretization squares and the characteristic length used in the MF-ROM[53]. The nonlocal equations governing the material at the ply level write:

$$\begin{cases} \boldsymbol{\nabla}_0 \cdot \bar{\boldsymbol{\sigma}} \left(\boldsymbol{\beta}^D(\boldsymbol{x}_{\text{ref}}), \boldsymbol{x}_{\text{ref}} \right) = 0 & \forall \boldsymbol{x}_{\text{ref}} \in \omega, \\ \breve{p}_0 - \boldsymbol{\nabla}_0 \cdot \left(\boldsymbol{c}_g \cdot \boldsymbol{\nabla}_0 \breve{p}_0 \right) = p_0 & \forall \boldsymbol{x}_{\text{ref}} \in \omega. \end{cases} \tag{73}$$

At the ply level, the stress $\bar{\boldsymbol{\sigma}}$ is computed using the built MF-ROM. The resolution of this nonlocal MFH problem is detailed in Appendix C.

This Section will start verifying the MF-ROM by applying it to the stochastic study of UD ply realizations under tensile loading. To this end, UD plies of $500 \times 250 \mu m^2$ will be tested by using the two constructed MF-ROMs, one built with the $25 \times 25 \mu m^2$ SVEs and the other one with the $45 \times 45 \mu m^2$ SVEs. Several UD ply realizations are tested under this loading condition in order to obtain a representative view of the MF-ROM performance. Then, this Section will end by validating the performance of the MF-ROM against real-life results. To this end, an experimental transverse compression test will be simulated, allowing not only to directly test the validity of the MF-ROM against the real behavior of the composite, but also to test the performance of the MF-ROM under multiple loading conditions.

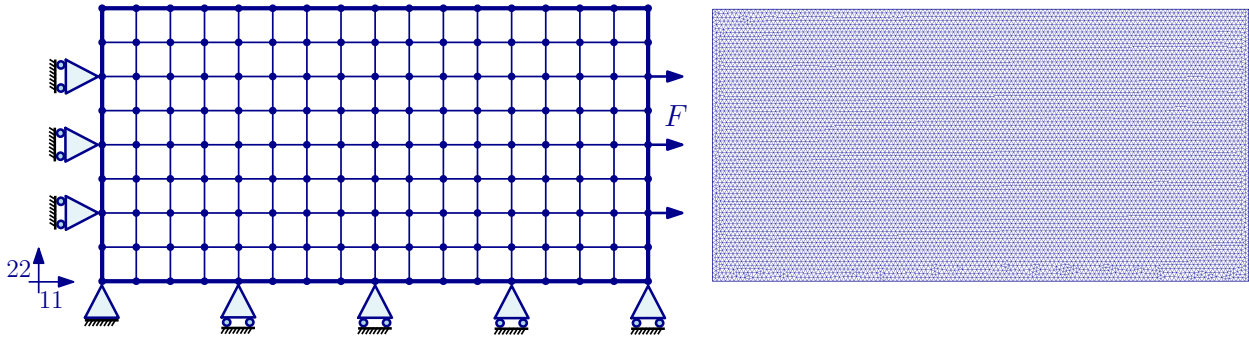## 5.1 | UD ply under tensile loading

FIGURE 35 Boundary conditions and property discretization on the left and quadratic mesh used on the right.

In the tensile test, the sample will be stretched in the horizontal direction as shown in Fig. 35. Quadratic elements are used to discretize the sample with a size smaller than the squares used for the property discretization and than the characteristic length, see Eq. (14), used in the nonlocal damage definition of the MFH. A convergence study with respect to the macroscale element size of the stochastic MF-ROM method is performed in Appendix F. It is shown that for elements of size lower than half of both the SVE size and the characteristic length l of the nonlocal MFH formulation, the predictions have converged.
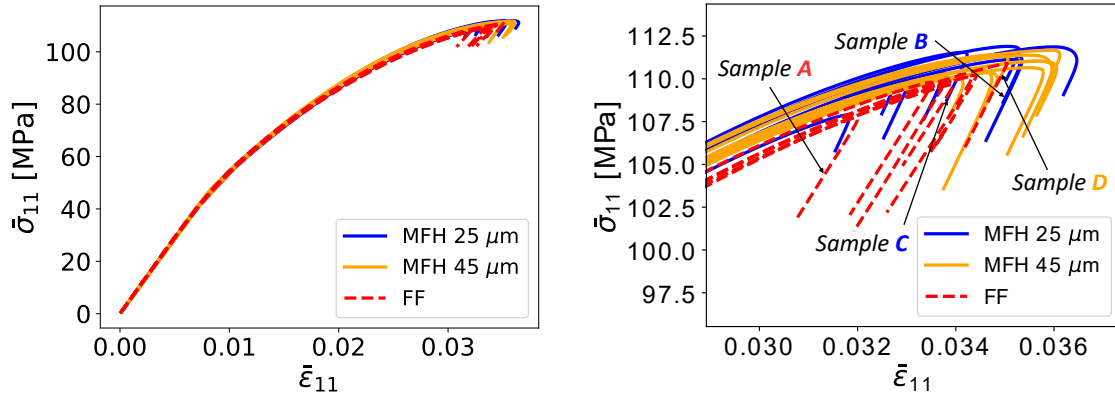
FIGURE 36 Averaged stress-strain curves for samples using the $25 \times 25\mu\text{m}^2$ (MFH 25μm) and $45 \times 45\mu\text{m}^2$ (MFH 45μm) MF-ROM, and full-field simulations (FF).

The model is capable of capturing successfully the average response of the sample at all stages of loading as seen in Fig. 36. In this figure it can be seen how the stress variability in the solutions provided by the MF-ROM is able to represent the variability in the stress-strain curve that is observed when performing the full-field simulations.

It is also observed how the point at which the failure phase of the sample begins, is correctly captured by the MF-ROM. However, it is worth noting the slightly stiffer behavior of the stochastic MFH simulations when reaching large strains. Enriching the damage modeling of the matrix by using more complex damage evolution laws that allow capturing more subtilities of the damage evolution of each SVE could help making the MF-ROM more accurate and able to find more complex behaviors of the material. The average runtimes of the ply analyses were respectively 5.3 hours and 124.4 hours on a i5 single processor for the stochastic simulation using the MF-ROM as surrogate and for the full-field simulation. In average, the ratio between both simulations is of 23.4 [-], demonstrating the interest of the method.
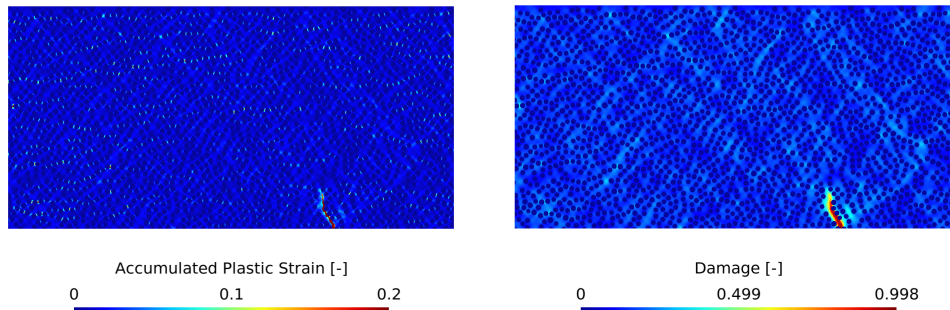
FIGURE 37 Accumulated plastic strain (left) and damage (right) field plots for the randomly picked full-field sample A whose response is reported in Fig. 36.

Let us now discuss the resultant distribution of different quantities through field plots by considering 4 randomly picked samples (A, B, C and D) whose responses are represented in Fig. 36. The field plots obtained for the accumulated plastic strain, damage and stresses on the full-field sample A can be observed in Figs. 37 and 38. Figs. 39 and 40 show the obtained field distributions of the accumulated plastic strain, damage or stress for the picked $25 \times 25\mu\text{m}^2$ MF-ROM sample B. Figs. 41 and 42 allow comparing these results with another sample C using the $25 \times 25\mu\text{m}^2$ MF-ROM, and Figs. 43 and 44 allows discussing, the results obtained for the $45 \times 45\mu\text{m}^2$ MF-ROM sample D. The properties discretization can be easily observed, as quantities such as damage or the accumulated plastic strain show a uniform field inside each property sub-division of the sample.

In the accumulated plastic strain field plot, it is possible to observe shear bands emanating from the location with the highest damage. This behavior can also be observed in the full-field simulations presented in Fig. 37. These bands are also seen in the damage field plots, see Figs. 39, 41 and 43, as the faster evolution of the plastic-strain causes a faster development of the
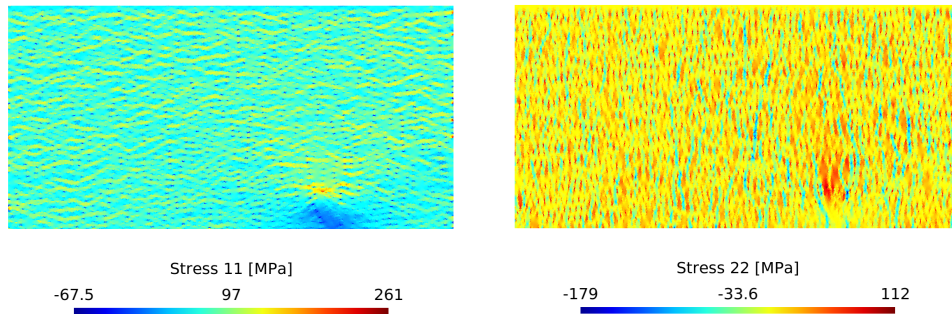
FIGURE 38 Stress 11 (left) and stress 22 (right) field plots for the randomly picked full-field sample A whose response is reported in Fig. 36.
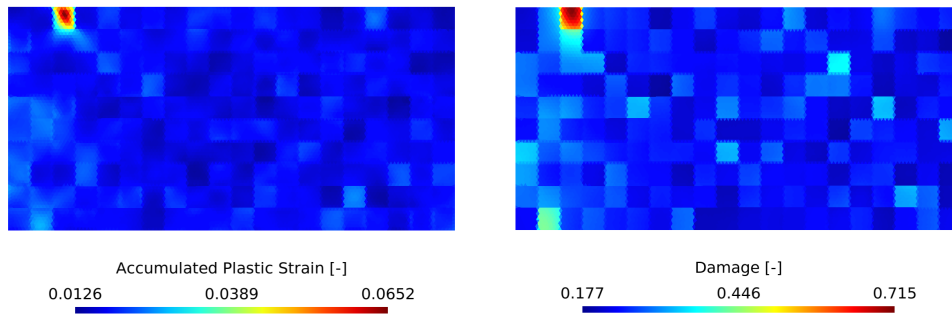

FIGURE 39 Accumulated plastic strain (left) and damage (right) field plots for the randomly picked $25 \times 25 \mu m^2$ sample B whose response is reported in Fig. 36.
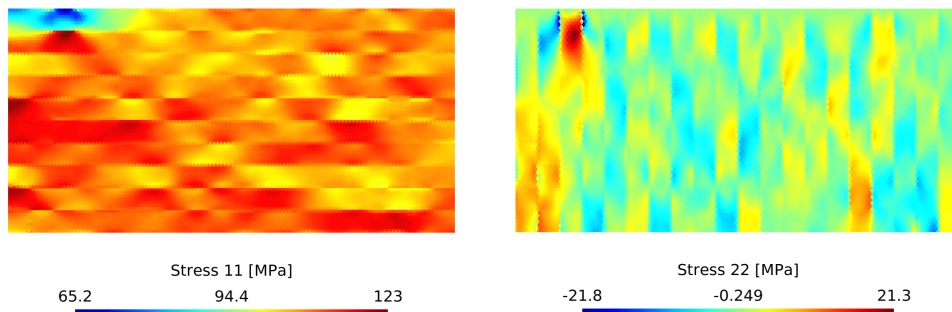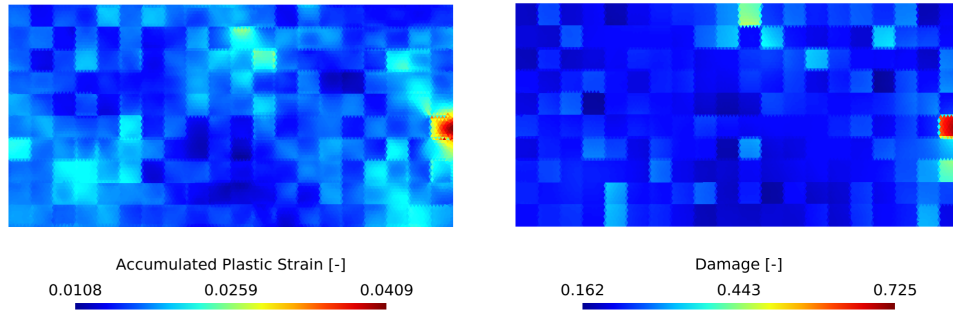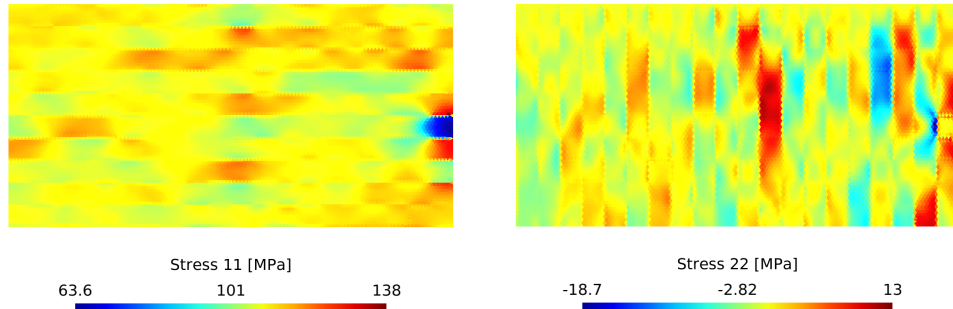

FIGURE 40 Stress 11 (left) and stress 22 (right) field plots for the random picked $25 \times 25 \mu m^2$ sample B whose response is reported in Fig. 36.

damage. A strong localization of the damage once the failure onset is reached can be seen. This localization effect can clearly be seen in the stress graphs. When looking at the component in the loading direction of the stress (Stress 11), the location in which one can find the highest damage suffers an abrupt decrease in its loading state, which provokes a high stress localization in its boundaries. Similarly, the high accumulated plastic strain and damage have a clear effect on the component 22 of the stress, which sees a sudden change in the localization zone and its surroundings.

Looking at Fig. 38, it is possible to observe a clear horizontal or vertical pattern in the stresses, depending whether the component 11 or 22 is studied. This effect is well captured by both MF-ROMs ($25 \times 25 \mu m^2$ and $45 \times 45 \mu m^2$) as shown by Figs. 40, 42 and 44. Focusing on the results obtained with the MF-ROM constructed from the $25 \times 25 \mu m^2$ and $45 \times 45 \mu m^2$ SVE realizations, it is possible to conclude that the methodology shows a good consistency on both cases, being both MF-ROMs capable of providing good predictions of the UD composite ply sample response up to its complete failure, where the model

Accumulated Plastic Strain [-]

0.0108   0.0259   0.0409

Damage [-]

0.162   0.443   0.725

FIGURE 41 Accumulated plastic strain (left) and damage (right) field plots for the randomly picked $25 \times 25 \mu m^2$ sample C whose response is reported in Fig. 36.

Stress 11 [MPa]

63.6   101   138

Stress 22 [MPa]

-18.7   -2.82   13

FIGURE 42 Stress 11 (left) and stress 22 (right) field plots for the randomly picked $25 \times 25 \mu m^2$ sample C whose response is reported in Fig. 36.

Accumulated Plastic Strain [-]

0.0137   0.0365   0.0594

Damage [-]

0.182   0.391   0.6
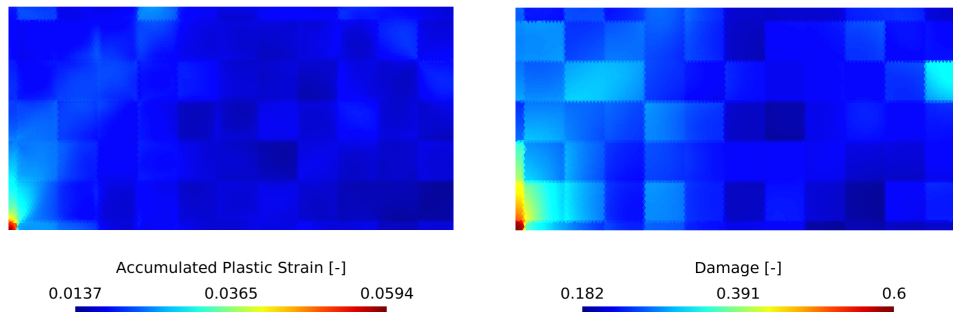
FIGURE 43 Accumulated plastic strain (left) and damage (right) field plots for the randomly picked $45 \times 45 \mu m^2$ sample D whose response is reported in Fig. 36.

satisfactorily captures how the geometrical variabilities found at the microstructure level affect the failure characteristics of the sample.

5.2 | Experimental compression test

In this Section, the MF-ROM will be tested against real life experiment results. For this purpose, the used test is the transverse compression test performed in the work by Chevalier et al.[96]. In this work, the transverse compression test is performed on a $10 \times 10 \times 10$ mm^3 cubic sample as shown in Fig. 45. In order to reduce the computational cost of the simulation, a 2D square sample of 10×10 mm^2 divided into two differentiated regions is used. As shown in Fig. 45, the 2D sample is divided into an inner and an outer region. As it was observed in the experimental results[96], the starting failure mechanism consists on a tensile
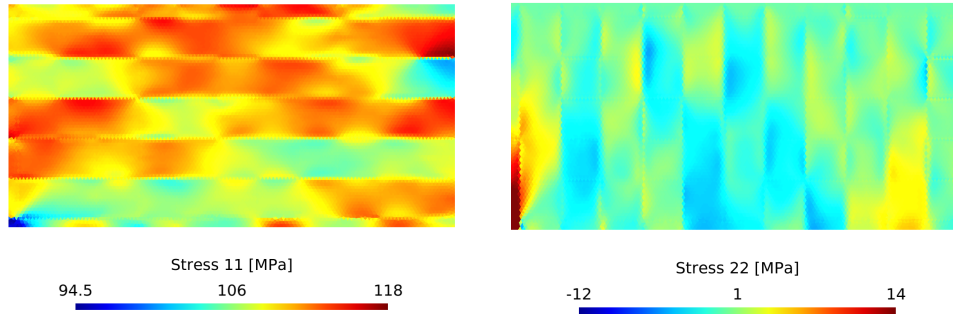
FIGURE 44 Stress 11 (left) and stress 22 (right) field plots for the randomly picked $45 \times 45\mu m^2$ sample D whose response is reported in Fig. 36.

stress driven failure at the center of the specimen, followed by a transition to shear failure (see Fig. 47). Therefore, numerical setup must be able to provide a good representation of the damage evolution in this inner region in order to correctly capture the failure mechanism of the sample. The inner part of the 2D geometry used for the test is meshed with quadratic triangular elements with a characteristic length of $20\mu m$ and the behavior will be modeled with the developed stochastic MF-ROM. The outer part will be modeled with a deterministic MFH model with a characteristic length of $200\mu m$, meaning a coarser mesh can be used. For this region, the properties used correspond to realizations of fiber volume fractions close to the average of 40%. This division of the tested sample allows not only to reduce the computational cost of the simulation while retaining the ability to capture the starting failure mechanism, but also to mitigate the effect of the boundary conditions on the failure characteristics of the sample. Two different boundary conditions will be tested in order to represent two limit cases. First, a no-slip condition is tested, in which the upper and lower edges will be constrained along the horizontal direction (see Fig. 45). Then, a perfect slip test in which these constrains are removed is performed. Due to the impossibility to accurately model the real friction effect at the top and lower boundaries of the tested sample, these two conditions will allow us to obtain two limit cases, knowing the experimental conditions remain in between these two conditions. For this test, the MF-ROM built from $25 \times 25 \ \mu m^2$ SVEs is used.
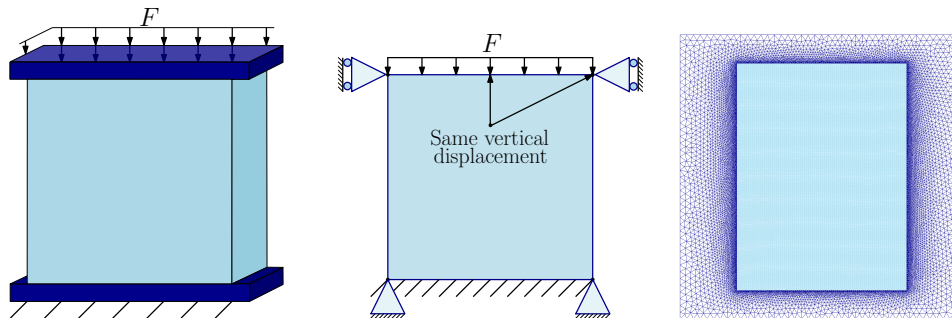

FIGURE 45 Schematic representation of the experimental setup built in[96] on the left, blocked case boundary conditions in the middle and second-order mesh with inner and outer regions on the right.

As in the experimental test by J. Chevlier[96], an average of 40% volume fraction is used, and the Young's modulus is corrected in order to account for the viscous effect seen on the real experiment. To perform this correction, the same modeling approach as the one implemented in V.D. Nguyen et al.[56] is used. This viscous correction consists on:

$$E_0 = \tilde{E}_0 + \sum_{i=1}^{N} E_i \exp\left(-\frac{t}{\tau_i}\right), \tag{74}$$

where $\tau_i, i = 1..N$ and $E_i, i = 1..N$, are the modulus and time constants of the N Maxwell branches and $\tilde{E}_0$ is the random value of the Young's modulus for a given realization. The properties identified for the modeling of the RTM6 epoxy in[56] to account for

visco-elasticity are used to account for the elastic stage of the experimental test performed at $\dot{\varepsilon} = 10^{-4} \text{s}^{-1}$, which took around 150s to be performed.

Looking at the averaged behavior results shown in Fig. 46, we can observe how the behavior of the composite sample under these loading conditions is capable of correctly capturing the behavior observed in the real experiment, correctly capturing the minimum stress reached during the test. Looking at the blocked edges BC (where the no-slip condition is applied to the upper and lower edges), a stiffer behavior compared to the one obtained at the experiment is obtained. This is due to the stronger constraints introduced by the no-slip condition at the edges of the sample. Similarly, this stronger constraint yields on a sooner fracture of the sample compared to the experiment results. In contrast, as expected, the free edges condition (BC in which the horizontal constraint is removed from the top and lower edges) yields a softer behavior and a later failure of the sample. As anticipated, the results obtained with both boundary conditions represent two limit cases, in which the experimental results yield between both results.
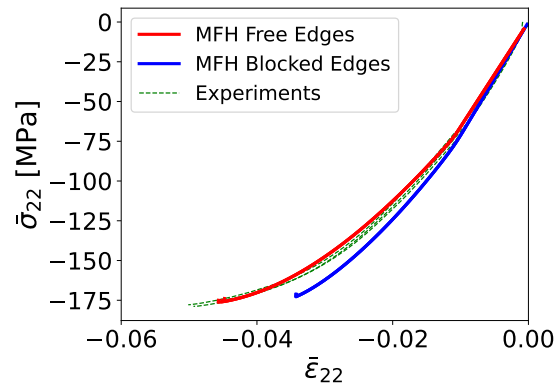
FIGURE 46 Stress-strain curve comparison between the MFH results and the experimental results obtained in [96] for a true strain rate of -10^{-4} s^{-1}.

As expected, a lower variability to the one observed in the previous ply stochastic study is observed due to the much larger size of the studied sample, size at which one obtains a representative response of the composite behavior. The use of the stochastic MF-ROM in the inner part of the sample allows to observe a variability in the damage evolution characteristics of each realization, as well as a slight variability in the elastic and nonlinear responses of the studied sample. Let us analyse the contour plots obtained from these simulations. First, Fig. 47 shows images from the real experiment results and a damage contour plot of the result obtained with a deterministic MFH at the dawn of failure in the test performed by J.M. Calleja et al. [54]. Then, Figs. 48-50 show the field plots for the stress, the accumulated plastic strain and the damage evolution state at the start of the failure of the sample realizations under the blocked edges BC. Fig. 51 shows the damage field plots obtained with the two samples tested with the free edges BC. All the shown results are extracted at the starting of the failure stage, meaning the tensile stress driven failure observed at the center of the specimen can be observed to be developing.

The effect of the MF-ROM used in the inner part of the sample can be observed in the field plots of the stress and the accumulated plastic strain. However, the most interesting comparison can be seen in the damage field plots. As it is presented, the damage contour plot at the beginning of the failure stage, presented a smooth and very uniform distribution over the sample when using the deterministic material law, being possible to observe the concentration of damage at the center of the sample due to the tensile stress driven failure. Similar results are observed on the new stochastic results. However, these present a much complex distribution and different behavior for each realization. Damage evolution can also be observed at the corners of the sample, however this is a result of the no-slip boundary condition used in the numerical setup. This is thought to be one of the main causes for the sooner failure observed with this boundary condition. As shown in Fig. 51, the free edges BC does not present this problem, allowing the material to undergo larger strains before failing.
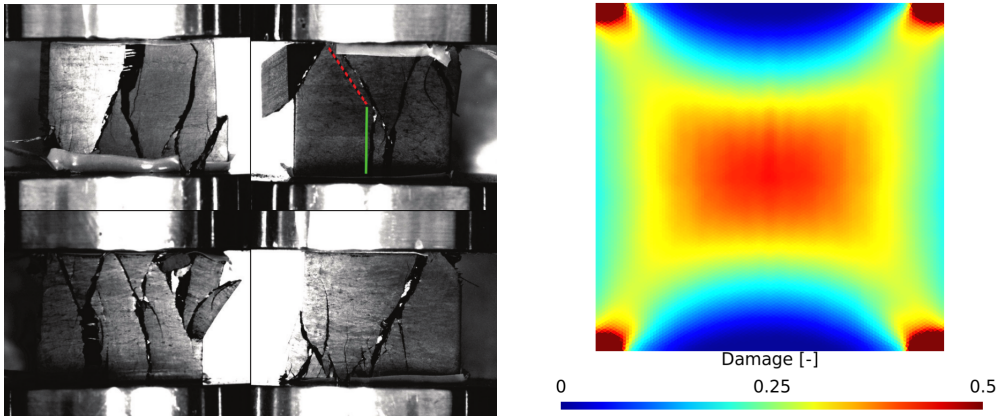
FIGURE 47 Surfaces of the cubic UD specimens after failure as shown in [96] on the left: the green and red lines emphasize the transition between a tensile stress dominated crack propagation to a shear one. Reprinted from Composite Structures, 209, J. Chevalier and P.P. Camanho and F. Lani and T. Pardoen, Multi-scale characterization and modelling of the transverse compression response of unidirectional carbon fiber reinforced epoxy, 160-176, Copyright (2019), with permission from Elsevier. Damage [-] contour plot of the deterministic multiscale MFH simulation with blocked upper and lower edges on the right.
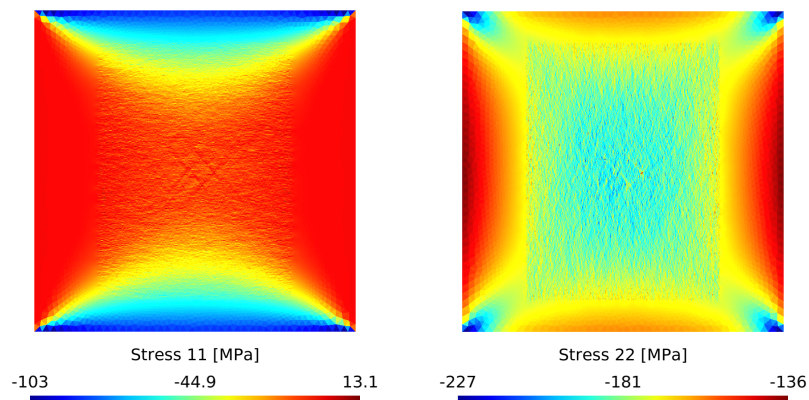
FIGURE 48 Stress 11 (left) and Stress 22 (right) field plots of realization A with constrained upper and lower edge.
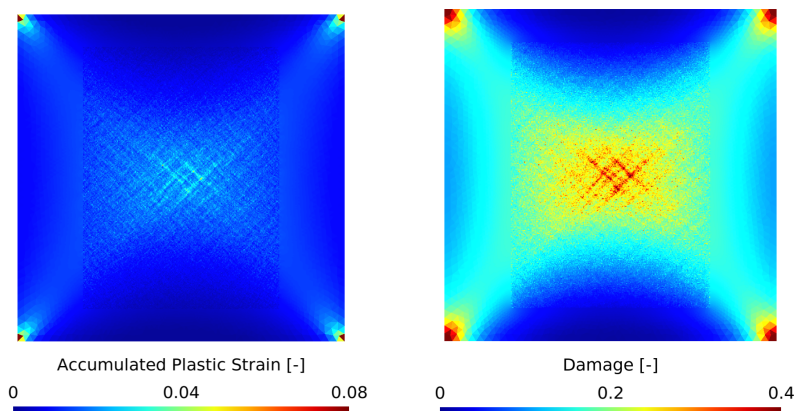
FIGURE 49 Accumulated plastic strain (left) and damage (right) field plots of realization A with constrained upper and lower edge.
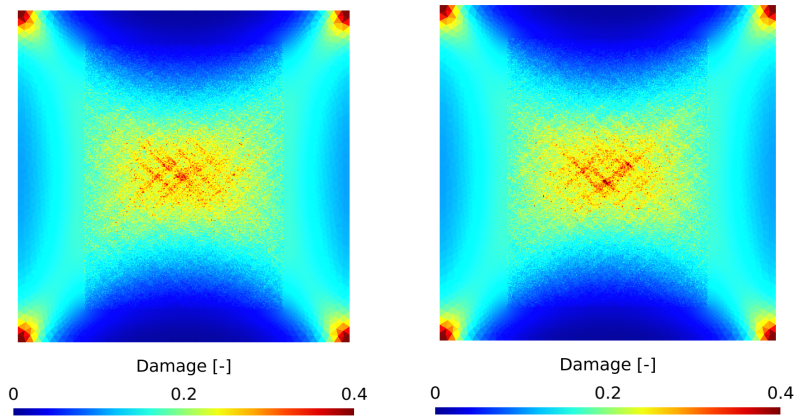
FIGURE 50 Damage field plots of realization B (left) and realization C (right) with constrained upper and lower edge.
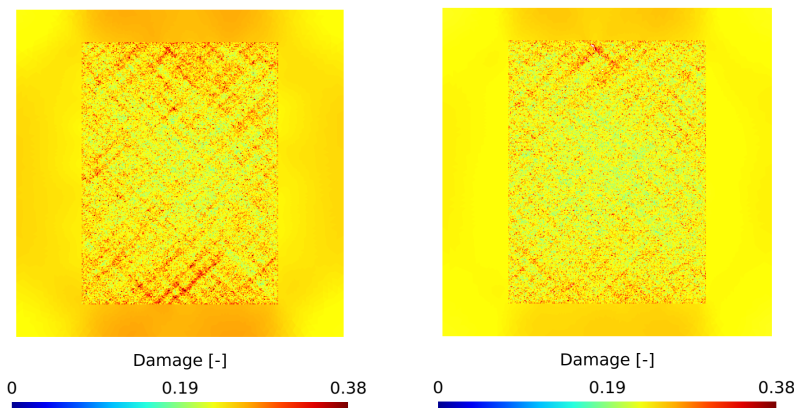

FIGURE 51 Damage field plots of realization D (left) and realization E (right) with slip conditions on upper and lower edge.

6 | CONCLUSION

The goal of this paper is to build a stochastic MF-ROM capable of capturing the pressure-dependent nonlinear behavior of two-phase UD composite materials with epoxy matrix, and capable of remaining valid after the strain-softening onset. In order to generate the stochastic MF-ROM, the information extracted from full-field SVE realizations is used as input of an inverse identification process that allows obtaining the effective random properties of a micromechanical MFH surrogate. The homogenized stress-strain responses and the damaged elastic tensor of the SVE realization serve as input for this identification process, however, these quantities do not remain valid once the strain-softening onset is reached. Once this stage is reached, a loss of size objectivity is encountered, meaning that a new objective value that allows to recover it is needed. In this work, the energy release rate is used as the target value that would allow this recovery of the size objectivity. By identifying the MFH surrogate parameters allowing to recover the same energy release rate as the one extracted from the full-field simulation, it is possible to correctly capture the behavior of each SVE up to its complete failure. Providing the model with the ability to maintain the size objectivity over the entire response of the material allows the uncertainties encountered in the material microstructure to be upscaled to the macroscale, making it possible to analyze the effect of these geometrical uncertainties in the failure characteristics of a material.

This stochastic MF-ROM paves the way for efficient stochastic virtual testing of composite materials by using an incremental-secant mean-field homogenization scheme as its basis. Two different SVE sizes are tested in the construction of the MF-ROM, being possible to study its impact in the performance of the stochastic simulations. The developed identification process is able to correctly capture the behavior of the studied SVEs under multiple loading conditions up to their complete failure. The identified parameters for each SVE represent a realization of a matrix of random vectors, which is used as the input of a data-driven-process that allows to obtain proper random fields by generating new data with the same statistical properties as the input

matrix. The generated data obtained with this data-driven process show a good representation of not only the distribution of each random parameter, but also an accurate representation of the relation between them. We however note that for an identified set of parameters, the MF-ROM predictions show more discrepancies with the corresponding SVE model when loading under shearing, for which the use of periodic boundary condition under damage is debatable. To reduce this error, different loading modes should be considered in the future during the identification process as well as more parameters of the MF-ROM –for example by considering different hardening laws in tension and compression. The more complex identification would then have to be conducted through unsupervised learning to account for several loading cases altogether, for example using a Bayesian Inference (BI) process as in [93].

Finally, the performance of the stochastic MF-ROM is verified against full-field simulations and real-life experiments. First, multiple UD plies under tensile loading are tested using full-field and the MF-ROM representations. The field distribution plots show how the MF-ROM models constructed with the two property discretizations ($25 \times 25 \mu m^2$ and $45 \times 45 \mu m^2$) are able to capture the overall patterns observed in the full-field simulations for quantities such as the stresses, the damage evolution or the accumulated plastic strain. Looking at the averaged responses, it is possible to observe a correct representation of the ply response for both MF-ROMs, obtaining a good variability of the responses at low and medium strains and being able to capture the failure point of the samples. Secondly, a transverse compression test experiment was virtually modeled with the developed MF-ROM built from the $25 \times 25 \mu m^2$ SVE realizations. Two different boundary conditions were used on the edges of the sample in order to test two limit cases (fully blocked upper and lower edges, simulating an infinite friction between the machine and the tested sample; and free upper and lower edges, simulating an idealized zero-friction condition). The obtained results show the ability of the methodology to capture the effects of the microscale variabilities into the macroscale response of the tested sample, confirming the good accuracy of the MF-ROM. This MF-ROM methodology allows for a high flexibility, making it easy to adapt it to other kind of materials or to enrich the model with more complex evolution laws. This high flexibility mixed with the promising obtained results and the intrinsic advantages of the incremental-secant formulation, allows to confirm this stochastic reduced-order model as a basis for future works. However, the approach is now limited to composites that can be represented by an equivalent ellipsoidal fiber. For more complex composite microstructures, MFH blocks made of equivalent fibers of different orientations and aspect ratio values can be combined following the approach presented in [97].

7 | ACKNOWLEDGEMENTS

8 | DATA AVAILABILITIES

The raw/processed data required to reproduce these findings are available under the Creative Commons Attribution 4.0 International (CC BY 4.0) licence [98].

☐

APPENDIX

A PHASE MODELS

A.1 Elastic phase model

The first presented model is the case of elastic phases. A neo-Hookean strain energy $\Psi_f = \Psi_f(\mathbf{C})$ ($\mathbf{C}$ stands for the right Cauchy-Green tensor) is used to describe the transversely isotropic hyperelastic model used for the modeling of the unidirectional fibers [70,71]. As transversely istropic properties are taken into account, the strain energy Ψ_f can be divided into isotropic (Ψ_f^{iso})

and transverse (Ψ_f^{trn}) components as:

$$\Psi_f = \Psi_f^{\text{iso}} + \Psi_f^{\text{trn}}. \tag{A1}$$

The parameters characterizing such material are the transverse Young's modulus E^{T}, Poisson's ratio ν^{TT} and shear modulus μ^{TT}, the longitudinal-transverse Poisson's ratio ν^{LT} and shear modulus μ^{LT}, and the longitudinal Young's modulus E^{L}.

The isotropic and transverse parts of the neo-Hookean strain energy write:

$$\Psi_f^{\text{iso}} = \frac{1}{2}\mu_{12}\left(I_1 - 3\right) - \mu_{12}\log J + \frac{1}{2}\lambda \log^2 J,$$

$$\Psi_f^{\text{trn}} = \left[\alpha_{\text{trn}} + 2\beta_{\text{trn}}\ln J + \gamma_{\text{trn}}\left(I_4 - 1\right)\right]\left(I_4 - 1\right) - \frac{1}{2}\alpha_{\text{trn}}\left(I_5 - 1\right), \tag{A2}$$

where $I_1 = \text{tr}\left(\mathbf{C}\right), I_4 = \mathbf{A} \cdot \mathbf{C} \cdot \mathbf{A}, I_5 = \mathbf{A} \cdot \mathbf{C}^2 \cdot \mathbf{A}$, being $\mathbf{A}$ the unit vector with the fibers direction in the original non-deformed configuration, $J = \sqrt{\det(\mathbf{C})}$. The quantities $\mu_{12}, \lambda, \alpha_{\text{trn}}, \beta_{\text{trn}}$, and γ_{trn} are material constants defined as:

$$\mu_{12} = \frac{E^{\text{T}}}{2\left(1 + \nu^{\text{TT}}\right)},$$

$$\lambda = \frac{E^{\text{T}}\left(\nu^{\text{TT}} + n\nu^{\text{TL}^2}\right)}{m^{\text{TL}}\left(1 + \nu^{\text{TT}}\right)},$$

$$\alpha_{\text{trn}} = \mu_{12} - \mu_3, \tag{A3}$$

$$\beta_{\text{trn}} = \frac{E^{\text{T}}\left[n^{\text{TL}}\nu^{\text{TL}}\left(1 + \nu^{\text{TT}} - \nu^{\text{TL}}\right) - \nu^{\text{TT}}\right]}{4m^{\text{TL}}\left(1 + \nu^{\text{TT}}\right)},$$

$$\gamma_{\text{trn}} = \frac{E^{\text{L}}\left(1 - \nu^{\text{TT}}\right)}{8m^{\text{TL}}} - \frac{\lambda + 2\mu_{12}}{8} + \frac{\alpha_{\text{trn}}}{2} - \beta_{\text{trn}},$$

where $m^{\text{TL}} = 1 - \nu^{\text{TT}} - 2n^{\text{TL}}\nu^{\text{TL}^2}$, and $n^{\text{TL}} = \frac{E^{\text{L}}}{E^{\text{T}}}$.

Finally, this strain energy Ψ_f allows the first Piola-Kirchhoff stress tensor to be written by computing the strain energy derivative with respect to the deformation gradient tensor $\mathbf{F}$ as:

$$\begin{aligned}\mathbf{P} = \frac{\partial \Psi_f}{\partial \mathbf{F}} = 2\mathbf{F} \cdot \frac{\partial \Psi_f}{\partial \mathbf{C}} = 2\mathbf{F} \cdot \Big\{ &\lambda \ln J \mathbf{C}^{-1} + \mu_{12}\left(\mathbf{I} - \mathbf{C}^{-1}\right) + 2\beta_{\text{trn}}\left(I_4 - 1\right)\mathbf{C}^{-1} \\ &+ 2\left[\alpha_{\text{trn}} + 2\beta_{\text{trn}}\ln J + 2\gamma_{\text{trn}}\left(I_4 - 1\right)\right]\mathbf{A} \otimes \mathbf{A} \\ &- \alpha_{\text{trn}}(\mathbf{C} \cdot \mathbf{A} \otimes \mathbf{A} + \mathbf{A} \otimes \mathbf{C} \cdot \mathbf{A})\Big\}. \end{aligned} \tag{A4}$$

A.2 Damage-enhanced pressure-dependent elasto-plastic phases model.

The elasto-plastic phase of the composite is modeled using the large strain constitutive model based on a multi-mechanism nonlocal damage continuum[72,56]. In this work, the viscous effect that was studied in these works will be omitted, as the main focus of this paper is the pressure-dependent effect seen in this kind of materials and the modeling of their failure. The deformation gradient $\mathbf{F}$ will be therefore divided into an elastic part and a plastic part such that:

$$\mathbf{F} = \mathbf{F}^{\text{el}} \cdot \mathbf{F}^{\text{pl}}. \tag{A5}$$

The elastic strain energy reads $\Psi\left(\mathbf{E}^{\text{el}}\right)$, where $\mathbf{E}^{\text{el}}$ stands for the elastic logarithmic strain defined by the elastic right Cauchy strain tensor $\mathbf{C}^{\text{el}}$ as:

$$\mathbf{E}^{\text{el}} = \frac{1}{2}\ln \mathbf{C}^{\text{el}}. \tag{A6}$$

A bi-logarithmic potential function is used for the definition of $\Psi\left(\mathbf{E}^{\text{el}}\right)$, which writes:

$$\Psi\left(\mathbf{C}^{\text{el}}\right) = \frac{\kappa^{\text{el}}}{2}\ln^2 J^{\text{el}} + \mu^{\text{el}}\left(\text{dev}\,\mathbf{E}^{\text{el}}\right) : \left(\text{dev}\,\mathbf{E}^{\text{el}}\right), \tag{A7}$$

where κ^{el} and μ^{el} are the bulk and shear moduli and J^{el} stands for the jacobian of the elastic deformation gradient $\mathbf{F}^{\text{el}}$.

Writing in the effective stress space in view of the application of damage, it is then possible to define the conjugated stress measures from the potential (Eq. A7) as:

$$\dot{\Psi} = \hat{\boldsymbol{\kappa}} : \mathbf{L}^{\text{el}} = \hat{\boldsymbol{\tau}} : \dot{\mathbf{E}}^{\text{el}}, \tag{A8}$$

where $\hat{\boldsymbol{\kappa}}$ is the effective Kirchhoff stress, $\hat{\boldsymbol{\tau}}$ is the effective stress measure conjugated to the logarithmic strain, also called the effective corotational Kirchhoff stress, and $\mathbf{L}^{\text{el}}$ stands for the elastic spatial gradient of velocity.

As shown in[72], the following relation between the effective Kirchhoff stress and corotational Kirchhoff stress can then be obtained:

$$\hat{\boldsymbol{\kappa}} = 2\mathbf{F}^{\text{el}} \cdot \frac{\partial \Psi}{\partial \mathbf{C}^{\text{el}}} \cdot \mathbf{F}^{eT} = \mathbf{F}^{e-T} \cdot \hat{\boldsymbol{\tau}} \cdot \mathbf{F}^{eT}, \tag{A9}$$

Finally, making use of these relations, it is possible to estimate the effective Piola-Kirchhoff stress $\hat{\mathbf{P}}$ as:

$$\hat{\mathbf{P}} = \hat{\boldsymbol{\kappa}} \cdot \mathbf{F}^{-T} = 2\mathbf{F}^{\text{el}} \cdot \frac{\partial \Psi}{\partial \mathbf{C}^{\text{el}}} \cdot \mathbf{F}^{p-T} = \mathbf{F}^{e-T} \cdot \hat{\boldsymbol{\tau}} \cdot \mathbf{F}^{p-T}. \tag{A10}$$

The used yield function for the modeling of plasticity represents a power-enhanced version of the original Drucker-Prager formulation capable of capturing accurately the behavior of amorphous glassy polymers by allowing to represent different power yield surfaces, including the classical Drucker-Prager or Merlo et al.[99] yield surfaces. This yield surface will be written in terms of a combined stress tensor $\boldsymbol{\phi}$ written in terms of the effective corotational Kirchhoff stress and the corotational backstress tensor $\hat{\boldsymbol{b}}$ as:

$$\boldsymbol{\phi} = \hat{\boldsymbol{\tau}} - \hat{\boldsymbol{b}}. \tag{A11}$$

The yield surface F of the pressure-dependent elasto-plastic material writes:

$$\begin{cases} F = \frac{(\phi^{\text{eq}})^\alpha}{\sigma_c^\alpha} - \frac{3(m^\alpha-1)}{(m+1)\sigma_c}\hat{\phi} - \frac{m^\alpha+m}{m+1} \leq 0, \\ \phi^{\text{eq}} = \sqrt{\frac{3}{2} \text{dev}(\boldsymbol{\phi}) : \text{dev}(\boldsymbol{\phi})}, \\ \hat{\phi} = \frac{1}{3} tr(\boldsymbol{\phi}), \end{cases} \tag{A12}$$

where the exponent α is a material constant, $\text{tr}(\boldsymbol{\phi}) = \phi_{ii}$, "dev" stands for the deviatoric operator $(\text{dev}(\bullet) = (\bullet) - \text{vol}(\bullet))$, "vol" standing for the volume operator $\left(\text{vol}(\bullet) = \frac{1}{3}\text{tr}(\bullet)\mathbf{1}\right)$, being $\mathbf{1}$ the second order identity tensor, and where σ_c represents the isotropic compressive yield stress. Finally, $m = \frac{\sigma_t}{\sigma_c}$ is the ratio between the current compressive and tensile yield stresses, where σ_t represents the current tensile yield stress. The evolution of the tensile and compressive yield stresses will be dictated by a tensile (H_t) and a compressive (H_c) hardening functions respectively, and the evolution of the backstress tensor will be ruled by a kinematic hardening evolution law (H_b). The plastic strain rate tensor $\mathbf{D}^{\text{pl}}$ is defined as:

$$\mathbf{D}^{\text{pl}} = \dot{\Gamma}\mathbf{Q}, \tag{A13}$$

where $\mathbf{Q}$ is the normal to the plastic flow potential and Γ the plastic multiplier. In order to take into account the irreversibility of the process, the internal variable used is the equivalent plastic strain p, whose increment is written as:

$$\dot{p} = k\sqrt{\mathbf{D}^{\text{pl}} : \mathbf{D}^{\text{pl}}} = k\dot{\Gamma}\sqrt{\mathbf{Q} : \mathbf{Q}}, \tag{A14}$$

where k is defined in terms of the plastic Poisson's ratio v_p as:

$$k = \frac{1}{\sqrt{1 + 2v_p^2}} \quad ; \quad k = \sqrt{\frac{2}{3}} \quad \text{if incompressible flow rule.} \tag{A15}$$

The hardening evolution laws describing the evolution of the compressive and tensile isotropic yield stresses are defined as a function of equivalent plastic strain $\dot{p}$ as $\dot{\sigma}_c = H_c(p)\dot{p}$, and $\dot{\sigma}_t = H_t(p)\dot{p}$, while the kinematic hardening law describing the backstress evolution follows $\dot{\hat{b}} = kH_b(p)\mathbf{D}^{\text{pl}}$.

Following previous contributions ([100,99,101]), a non-associated flow rule is used for the correct capturing of the polymer behavior. The flow rule will then evolve in a direction normal to a plastic flow potential, which writes:

$$G = (\phi^{\text{eq}})^2 + \beta\left(\hat{\phi}\right)^2. \tag{A16}$$

where β is a material parameter. The plastic Poisson's ratio v_p yields from this potential flow, modeling the volumetric plastic deformation. At the plastic flow onset v_p writes:

$$v_p = \frac{9 - 2\beta}{18 + 2\beta}. \tag{A17}$$

As previously pointed out, the non-associated flow follows a direction normal to the plastic flow potential, writing:

$$\mathbf{Q} = \frac{\partial G}{\partial \hat{\boldsymbol{\tau}}} = 3\text{dev}(\boldsymbol{\phi}) + \frac{2\beta}{3}\text{vol}(\boldsymbol{\phi}), \tag{A18}$$

where $\text{vol}(\boldsymbol{\phi}) = \frac{tr(\boldsymbol{\phi})}{3}\mathbf{1}$. This normal is used in the computation of the plastic evolution, which is determined through the plastic strain rate tensor as:

$$\dot{\mathbf{F}}^{pl} = \mathbf{D}^{pl} \cdot \mathbf{F}^{pl}. \tag{A19}$$

Integrating this expression on a time interval $[t_n, t_{n+1}]$ and using the radial return algorithm [102], one finally gets:

$$\mathbf{F}^{pl}_{n+1} = \exp(\Gamma\mathbf{Q})\mathbf{F}^{pl}_n, \tag{A20}$$

where Γ stands for the plastic multiplier.

For the elasto-plastic phases, a nonlocal damage model will be taken into account, introducing a new damage parameter ($D \in [0, 1)$) in order to take this phenomenon into consideration. The multi-stage behavior of the high-crosslinked epoxy is modeled using a multi-stage damage formulation (see Fig. A1) divided into softening (D_s) and failure (D_f) damages, such that:

$$D = 1 - (1 - D_s)(1 - D_f). \tag{A21}$$
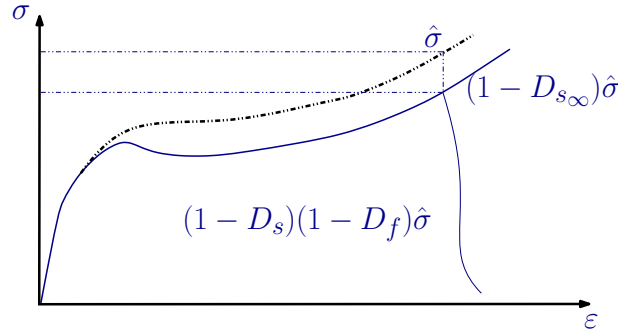
FIGURE A1 Schematic representation of the modeled material response and the effect of the used multi-stage damage evolution law

The damage is formulated in a Lemaitre-Chaboche style [103] writing the first Piola-Kirchhoff stress as:

$$\mathbf{P} = \left(1 - D_s\right)\left(1 - D_f\right)\hat{\mathbf{P}}. \tag{A22}$$

The saturation law D_s follows a saturation law that tends to the saturated value $D_{s\infty}$:

$$\begin{cases} \dot{D}_s(t) = H_s \left(p_s - p_{s0}\right)^{\zeta_s} \left(D_{s\infty} - D_s\right) \dot{p}_s, \\ p_s(t) = \max_{\tau \in [0,t]} \left(p_{s0}, \tilde{p}(\tau)\right), \end{cases} \tag{A23}$$

where p_{s0} is the damage threshold, $\breve{p}$ is the nonlocal counterpart of the equivalent plastic strain p following the Helmholtz-type Eq. (4) and H_s, ζ_s and $D_{s\infty}$ are material constants. Integrating Eq. (A23), it is possible to obtain the expression of D_s as:

$$D_s = D_{s\infty} \left[1 - \exp\left(-\frac{H_s}{\zeta_s + 1}\left(p_s - p_{s0}\right)^{\zeta_s+1}\right)\right]. \tag{A24}$$

Similarly, the failure damage is defined as:

$$\begin{cases} \dot{D}_f(t) = H_f \left(p_f\right)^{\zeta_f} \left(1 - D_f\right)^{-\zeta_d} \dot{r}_f, \\ r_f(t) = \max_{\tau \in [0,t]} \left(p_{f_0}, \breve{p}_f(\tau)\right), \end{cases} \tag{A25}$$

where the failure strain r_f results from $\breve{p}_f$ the nonlocal failure plastic strain and H_f, ζ_f, ζ_d and $D_{f\infty}$ are material constants. As for the case of the nonlocal plastic strain. The nonlocal failure plastic strain $\breve{p}_f$ is related to its local counterpart p_f, whose evolution is described below, with the Helmholtz-type Eq. (4). The constant H_f can be written in terms of other material quantities as:

$$H_f = \frac{\zeta_f + 1}{\zeta_d + 1} \frac{1 - \left(1 - D_{f_c}\right)^{\zeta_d+1}}{p_{f_c}^{\zeta_f+1} - p_{f_0}^{\zeta_f+1}}, \tag{A26}$$

where $D_{f_c} = D_f(p_{f_c})$ stands for the critical failure damage value and p_{f_c} is the critical nonlocal failure plastic strain. Integrating Eq. (A25), one gets:

$$D_f = \begin{cases} 0 & \text{if } r_f \leq p_{f_0}; \\ 1 - \left[1 - H_f \frac{\zeta_d+1}{\zeta_f+1} \left(r_f^{\zeta_f+1} - p_{f_0}^{\zeta_f+1} \right) \right]^{\frac{1}{\zeta_d+1}} & \text{if } p_{f_0} \leq r_f \leq p_{f_c}; \\ D_{f_c} & \text{if } p_{f_c} \leq r_f. \end{cases} \tag{A27}$$

The onset at which failure starts on a given node is controlled by a criterion based on the equivalent plastic strain[104] which writes:

$$\Phi_f = p - a \exp(-bT) - c = 0, \tag{A28}$$

where $T = \frac{\text{tr}(\hat{\tau})}{3\hat{\tau}^{eq}}$ refers to the stress triaxiality, and where a, b and c are material constants. Once the failure onset is reached, the evolution of the failure surface is defined by the Kuhn-Tucker condition:

$$\Phi_f - r \leq 0, \quad \dot{r} \geq 0, \quad \text{and} \quad \dot{r}\left(\Phi_f - r\right) = 0, \tag{A29}$$

where r is a non-negative variable that allows to store the maximal failure criterion reached in the loading history. Using the Kuhn-Tucker condition (Eq. A29), it is possible to define the evolution of the failure plastic strain as:

$$\dot{p}_f = \begin{cases} 0 & \text{if } \dot{r} = 0, \\ \dot{p} & \text{if } \dot{r} > 0. \end{cases} \tag{A30}$$

Concerning the boundary conditions used for the nonlocal variables, the equivalence to periodic boundary condition[56] is used for both $\breve{p}$ and $\breve{p}_f$ at the SVE boundaries $\partial\omega$:

$$\begin{cases} [\![c_g \cdot \nabla_0 \breve{p}_i]\!] \cdot N = 0, \\ [\![\dot{\breve{p}}_i]\!] = 0. \end{cases} \quad \text{on} \quad \partial\omega, \quad \breve{p}_i = \breve{p}, \breve{p}_f, \tag{A31}$$

where $[\![\bullet]\!]$ represents the jump operator between matching material points at opposite faces of the SVE, i.e. $[\![\bullet]\!] = \bullet\left(x_{\text{ref}}^+\right) - \bullet\left(x_{\text{ref}}^-\right)$.

At the internal boundary, $\partial_I\omega$ composed by the set of interfaces between the fibers and the matrix with outward normal N^I, the following conditions are used for the nonlocal variable $\breve{p}$:

$$\begin{cases} [\![c_g \cdot \nabla_0 \breve{p}]\!] \cdot N^I = 0, \\ [\![\breve{p}]\!] = 0. \end{cases} \quad \text{on} \quad \partial_I\omega. \tag{A32}$$

where $[\![\bullet]\!]$ represents the jump operator at the interface between fibers and matrix $[\![\bullet]\!] = \bullet_{\text{matrix}} - \bullet_{\text{fiber}}$, since they allow the introduction of the length scale effect of the matrix response introduced by the fiber distribution[56]. However, for the nonlocal variable $\breve{p}_f$, at the internal boundary $\partial_I\omega$, the following condition is considered so that the damage can develop at the interface between the fibers and the matrix:

$$\nabla_0 \breve{p}_f \cdot N^I = 0, \text{ on} \quad \partial_I\omega. \tag{A33}$$

B : STATISTICAL PROPERTIES OF THE MICROSTRUCTURE

The generated microstructures were built using the algorithm developed in[7], where the empirical statistical parameters of the microstructures extracted from SEM images were use as dependent variables. Five different random variables are used for the characterization of these microstructures: the fiber radius R, the nearest/neighbor net distance d_{1st}, the orientation θ_{1st} of the undirected line connecting these two fiber center points, the difference Δd between the net distances to the second neighbor (d_{2nd}) and the first /neighbor (d_{1st}), and the difference $\Delta\theta$ between the orientations of the second neighbor (θ_{2nd}) and the first nearest neighbor (θ_{1st}). A schematic representation of these descriptors is shown in Fig. B2. Besides, their distribution, their correlation was evaluated from the SEM images information. The fiber radius was found to be independent while the other
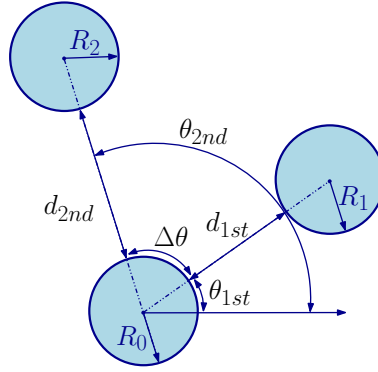
FIGURE B2 Schematic representation of the statistical characteristics of the generated microstructure and its descriptors.

parameters had a correlation matrix $\mathbf{R}$ as:

$$
\mathbf{R} = \begin{array}{c} d_{1\text{st}} \\ \theta_{1\text{st}} \\ \Delta d \\ \Delta \theta \end{array} \begin{pmatrix} \overset{d_{1\text{st}}}{1.0} & \overset{\theta_{1\text{st}}}{0.014} & \overset{\Delta d}{0.205} & \overset{\Delta \theta}{0.022} \\ & 1.0 & 0.002 & 0.020 \\ \text{symmetric} & & 1.0 & -0.005 \\ & & & 1.0 \end{pmatrix}.
\tag{B34}
$$

However, since the distributions exhibit non-Gaussianity, the statistical dependence of these random variables were assessed by their distance correlations matrix $\mathbf{dR}$ following [105], which reads in this case

$$
\mathbf{dR} = \begin{array}{c} d_{1\text{st}} \\ \theta_{1\text{st}} \\ \Delta d \\ \Delta \theta \end{array} \begin{pmatrix} \overset{d_{1\text{st}}}{1.0} & \overset{\Theta_{1\text{st}}}{0.040} & \overset{\Delta d}{0.273} & \overset{\Delta \theta}{0.075} \\ & 1.0 & 0.048 & 0.046 \\ \text{symmetric} & & 1.0 & 0.064 \\ & & & 1.0 \end{pmatrix},
\tag{B35}
$$

showing that two parameters should be considered as dependent.

Using the copula constructed from their cumulative distributions for the two dependent variables and using the inverse transform sampling method based on their cumulative distribution for the three independent variables, a generator was constructed in [7], in which the targeted volume fraction can be tuned, see also [4]. In the present work, a targeted volume fraction of 40% was set, and the resulting distributions of the microstructure descriptors are provided in Figs. B3 and B4.

C MFH MULTISCALE APPROACH

C.1 MFH resolution[90]

Assuming only the matrix phase can develop damage and making use of Eq. (31), at a given configuration $n + 1$, the MFH scheme satisfies:

$$
\Delta \varepsilon^{\text{r}}_{\text{I}n+1} = \boldsymbol{B}^{\epsilon}\left(\text{I}, \boldsymbol{C}^{\text{SDr}}_{0}, \boldsymbol{C}^{\text{Sr}}_{\text{I}}\right) : \Delta \varepsilon^{\text{r}}_{0n+1},
\tag{C36}
$$

where the equation relating the strain increments of the phases and the composite write:

$$
\Delta \bar{\varepsilon}^{\text{r}}_{n+1} = v_0 \Delta \varepsilon^{\text{r}}_{0n+1} + v_{\text{I}} \Delta \varepsilon^{\text{r}}_{\text{I}n+1}.
\tag{C37}
$$

Accounting for Eq. (C36) and multiplying Eq. (C37) by the strain concentration tensor $\boldsymbol{B}^{\epsilon}$ one gets:

$$
v_0 \Delta \varepsilon^{\text{r}}_{\text{I}n+1} + v_{\text{I}} \boldsymbol{B}^{\epsilon}\left(\text{I}, \boldsymbol{C}^{\text{SDr}}_{0}, \boldsymbol{C}^{\text{Sr}}_{\text{I}}\right) : \Delta \varepsilon^{\text{r}}_{\text{I}n+1} = \boldsymbol{B}^{\epsilon}\left(\text{I}, \boldsymbol{C}^{\text{SDr}}_{0}, \boldsymbol{C}^{\text{Sr}}_{\text{I}}\right) : \Delta \bar{\varepsilon}^{\text{r}}_{n+1},
\tag{C38}
$$

where $\boldsymbol{B}^{\epsilon}$ is defined with the Mori-Tanaka assumption, Eq. 18. Eq. (C38) can be then rewritten:

$$
\Delta \varepsilon^{\text{r}}_{\text{I}n+1} + v_0 \boldsymbol{S} : \left[\left(\boldsymbol{C}^{\text{SDr}}_{0}\right)^{-1} : \boldsymbol{C}^{\text{Sr}}_{\text{I}} - \boldsymbol{I}\right] : \Delta \varepsilon^{\text{r}}_{\text{I}n+1} = \Delta \bar{\varepsilon}^{\text{r}}_{n+1}.
\tag{C39}
$$

(a) Nearest-neighbor orientation

(b) Difference between nearest-neighbor orientations

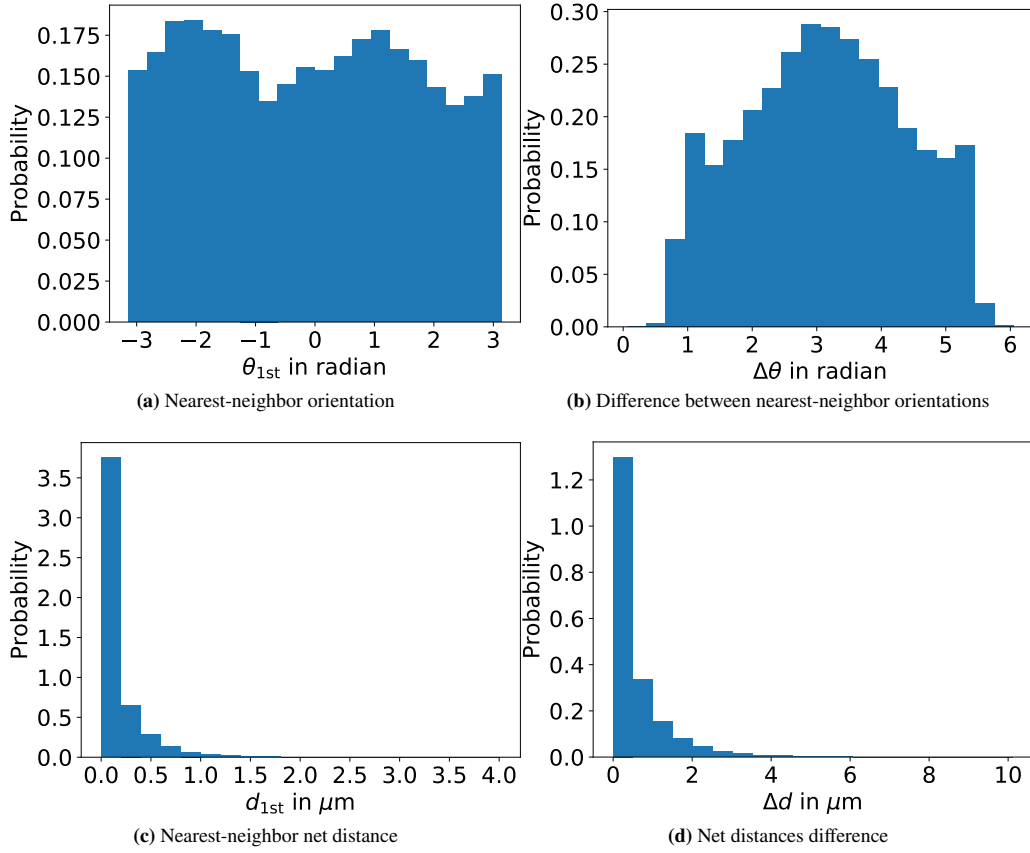**(c)** Nearest-neighbor net distance

(d) Net distances difference

FIGURE B3 Probability density histograms for the parameters characterizing the fibers spatial properties of the generated microstructures: (a) Nearest-neighbor orientation θ_{1st} distribution (b) Difference between nearest-neighbor orientations $\Delta\theta$ distribution (c) Nearest-neighbor net distance d_{1st} distributions (d) Difference between the net distances to the second and to the first nearest-neighbors Δd distribution.
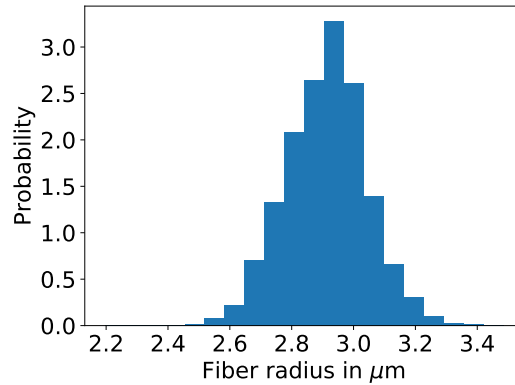
FIGURE B4 Probability density histograms of fiber radius from the generated microstructures.

The stress residual vector $\boldsymbol{F} = 0$ writes:

$$\boldsymbol{F} = \boldsymbol{C}_0^{\text{SDr}} : \left[\Delta\boldsymbol{\varepsilon}_{In+1}^{r} - \frac{1}{v_0}\boldsymbol{S}^{-1} : \left(\Delta\boldsymbol{\varepsilon}_{In+1}^{r} - \Delta\bar{\boldsymbol{\varepsilon}}_{n+1}^{r} \right) \right] - \boldsymbol{C}_I^{\text{Sr}} : \Delta\boldsymbol{\varepsilon}_{In+1}^{r}, \tag{C40}$$

being possible to linearize it as:

$$\mathrm{d}\boldsymbol{F} = \frac{\partial \boldsymbol{F}}{\partial \boldsymbol{\varepsilon}_\mathrm{I}} : \mathrm{d}\Delta\boldsymbol{\varepsilon}_\mathrm{I}^\mathrm{r} + \frac{\partial \boldsymbol{F}}{\partial \boldsymbol{\varepsilon}_0} : \mathrm{d}\Delta\boldsymbol{\varepsilon}_0^\mathrm{r} + \frac{\partial \boldsymbol{F}}{\partial \bar{\boldsymbol{\varepsilon}}} : \mathrm{d}\Delta\bar{\boldsymbol{\varepsilon}}^\mathrm{r} + \frac{\partial \boldsymbol{F}}{\partial \breve{p}_0} \, \mathrm{d}\breve{p}_0. \tag{C41}$$

For a given time step, the values of $\Delta\bar{\boldsymbol{\varepsilon}}^\mathrm{r}$ and $\breve{p}_0$ remain constant and Eq. (C41) yields: $\mathrm{d}\boldsymbol{F} = \boldsymbol{J} : \mathrm{d}\boldsymbol{\varepsilon}_\mathrm{I}$, where $\boldsymbol{J}$ writes:

$$\begin{aligned}
\boldsymbol{J} =& \boldsymbol{C}_0^{\mathrm{SDr}}{}_{n+1} : \left[\boldsymbol{I} - \boldsymbol{S}^{-1}\right] - \boldsymbol{C}_{\mathrm{I}_{n+1}}^{\mathrm{Sr}} - \frac{\partial \boldsymbol{C}_{\mathrm{I}_{n+1}}^{\mathrm{Sr}}}{\partial \boldsymbol{\varepsilon}_\mathrm{I}} : \Delta\boldsymbol{\varepsilon}_{\mathrm{I}_{n+1}}^\mathrm{r} - \\
& \frac{v_\mathrm{I}}{v_0} \left(\frac{\partial \boldsymbol{C}_0^{\mathrm{SDr}}{}_{n+1}}{\partial \boldsymbol{\varepsilon}_0} + \frac{\partial \boldsymbol{C}_0^{\mathrm{SDr}}{}_{n+1}}{\partial D_0} \frac{\partial D_0}{\partial \boldsymbol{\varepsilon}_0} \right) : \left[\Delta\boldsymbol{\varepsilon}_{\mathrm{I}_{n+1}}^\mathrm{r} - \boldsymbol{S}^{-1} : \frac{\left(\Delta\boldsymbol{\varepsilon}_{\mathrm{I}_{n+1}}^\mathrm{r} - \Delta\bar{\boldsymbol{\varepsilon}}_{n+1}^\mathrm{r}\right)}{v_0} \right] - \\
& \frac{v_\mathrm{I}}{v_0^2} \boldsymbol{C}_0^{\mathrm{SDr}}{}_{n+1} \otimes \left(\Delta\boldsymbol{\varepsilon}_{\mathrm{I}_{n+1}}^\mathrm{r} - \Delta\bar{\boldsymbol{\varepsilon}}_{n+1}^\mathrm{r}\right) :: \left(\boldsymbol{S}^{-1} \otimes \boldsymbol{S}^{-1}\right) :: \left(\frac{\partial \boldsymbol{S}}{\partial \boldsymbol{\varepsilon}_0} + \frac{\partial \boldsymbol{S}}{\partial D_0} \frac{\partial D_0}{\partial \boldsymbol{\varepsilon}_0} \right) - \frac{v_\mathrm{I}}{v_0} \boldsymbol{C}_0^{\mathrm{SDr}}{}_{n+1} : \boldsymbol{S}^{-1}.
\end{aligned} \tag{C42}$$

Appendix C.2 reports the derivatives of $\boldsymbol{C}_i^\mathrm{S}$ with respect to $\boldsymbol{\varepsilon}_i$ and Appendix C.3 details the derivative of the Eshelby tensor.

After convergence of the MFH resolution, constraining $d\boldsymbol{F} = 0$, the strain increment of each phase coming from the variation of $\mathrm{d}\Delta\bar{\boldsymbol{\varepsilon}}^\mathrm{r}$ is written as:

$$\frac{\partial \boldsymbol{\varepsilon}_\mathrm{I}}{\partial \bar{\boldsymbol{\varepsilon}}} = -\boldsymbol{J}^{-1} : \frac{\partial \boldsymbol{F}}{\partial \bar{\boldsymbol{\varepsilon}}} \,, \text{ and } \frac{\partial \boldsymbol{\varepsilon}_\mathrm{I}}{\partial \breve{p}_0} = -\boldsymbol{J}^{-1} : \frac{\partial \boldsymbol{F}}{\partial \breve{p}_0} \,. \tag{C43}$$

Using the equation relating the composite and the phases strain increments $\mathrm{d}\bar{\boldsymbol{\varepsilon}}^\mathrm{r} = v_0 \mathrm{d}\boldsymbol{\varepsilon}_0^\mathrm{r} + v_\mathrm{I} \mathrm{d}\boldsymbol{\varepsilon}_\mathrm{I}^\mathrm{r}$, the set of equations for the matrix phase writes:

$$\frac{\partial \boldsymbol{\varepsilon}_0}{\partial \bar{\boldsymbol{\varepsilon}}} = \frac{1}{v_0}\left(\boldsymbol{I} - v_1 \frac{\partial \boldsymbol{\varepsilon}_\mathrm{I}}{\partial \bar{\boldsymbol{\varepsilon}}} \right) \,, \text{ and } \frac{\partial \boldsymbol{\varepsilon}_0}{\partial \breve{p}_0} = -\frac{v_\mathrm{I}}{v_0} \frac{\partial \boldsymbol{\varepsilon}_\mathrm{I}}{\partial \breve{p}_0}. \tag{C44}$$

C.2 Derivatives of secant operators[54]

This Section will present the derivatives of the secant and damaged-enhanced secant operators. In order to simplify the notation of the equations presented hereafter, the subscript referring to the phase is omitted.

Accounting for the isotropic nature of the secant operator, the derivative of $\boldsymbol{C}^{\mathrm{Sr}}$ writes:

$$\frac{\partial \boldsymbol{C}^{\mathrm{Sr}}}{\partial \boldsymbol{\varepsilon}} = \frac{\partial}{\partial \Delta\boldsymbol{\varepsilon}^\mathrm{r}} \left(3\kappa_s^\mathrm{r} \boldsymbol{I}^{\mathrm{vol}} + 2\mu_s^\mathrm{r} \boldsymbol{I}^{\mathrm{dev}}\right) : \frac{\partial \Delta\boldsymbol{\varepsilon}^\mathrm{r}}{\partial \boldsymbol{\varepsilon}} = \left(3\boldsymbol{I}^{\mathrm{vol}} \frac{\partial \kappa_s^\mathrm{r}}{\partial \Gamma} + 2\boldsymbol{I}^{\mathrm{dev}} \frac{\partial \mu_s^\mathrm{r}}{\partial \Gamma} \right) \otimes \frac{\partial \Gamma}{\partial \boldsymbol{\varepsilon}}, \tag{C45}$$

where the derivative $\frac{\partial \Gamma}{\partial \boldsymbol{\varepsilon}}$ is developed in appendix C.4 and the derivatives of the bulk and shear moduli write:

$$\frac{\partial \mu_s^\mathrm{r}}{\partial \Gamma} = -\frac{6\mu^{\mathrm{el}^2}}{\left(1 + 6\mu^{\mathrm{el}}\Gamma\right)^2}, \text{ and } \frac{\partial \kappa_s^\mathrm{r}}{\partial \Gamma} = -\frac{2\beta\kappa^{\mathrm{el}^2}}{\left(1 + 2\kappa^{\mathrm{el}}\Gamma\beta\right)^2}. \tag{C46}$$

When accounting for damage, the derivative of the secant operator becomes:

$$\frac{\mathrm{d}\boldsymbol{C}^{\mathrm{SDr}}}{\mathrm{d}\boldsymbol{\varepsilon}} = \frac{\partial \boldsymbol{C}^{\mathrm{SDr}}}{\partial \boldsymbol{\varepsilon}} + \frac{\partial \boldsymbol{C}^{\mathrm{SDr}}}{\partial D} \frac{\partial D}{\partial \boldsymbol{\varepsilon}} = (1 - D)\frac{\partial \boldsymbol{C}^{\mathrm{Sr}}}{\partial \boldsymbol{\varepsilon}} - \boldsymbol{C}^{\mathrm{Sr}} \otimes \frac{\partial D}{\partial \boldsymbol{\varepsilon}}, \tag{C47}$$

where $\frac{\partial D}{\partial \boldsymbol{\varepsilon}} = \frac{\partial D}{\partial \Delta\boldsymbol{\varepsilon}^\mathrm{r}} = 0$.

C.3 Eshelby tensor derivatives[54]

This Section will present the Eshelby tensor derivatives for the elasto-plastic and the damage-enhanced elasto-plastic case. In order to simplify the notation of the equations presented hereafter, the subscript referring to the phase is omitted.

Elasto-plasticity

In the case of elasto-plasticity, the Eshelby tensor derivative writes:

$$\frac{\partial \boldsymbol{S}}{\partial \Delta\boldsymbol{\varepsilon}^\mathrm{r}} = \frac{\partial \boldsymbol{S}}{\partial v} \otimes \left(\frac{\partial v}{\partial \kappa_s^\mathrm{r}} \frac{\partial \kappa_s^\mathrm{r}}{\partial \Gamma} + \frac{\partial v}{\partial \mu_s^\mathrm{r}} \frac{\partial \mu_s^\mathrm{r}}{\partial \Gamma} \right) \frac{\partial \Gamma}{\partial \Delta\boldsymbol{\varepsilon}^\mathrm{r}}, \tag{C48}$$

where the derivatives of the bulk and shear moduli are given in Eq. (C46) and the derivative $\frac{\partial \Gamma}{\partial \boldsymbol{\varepsilon}}$ is developed in Appendix C.4.

Damage-enhanced elasto-plasticity

In the case in which damage is taken into account, the Eshelby tensor derivative writes:

$$\frac{\partial S}{\partial \Delta \varepsilon^{\mathrm{r}}} = \frac{\partial S}{\partial v} \otimes \left[\frac{\partial v}{\partial \kappa_s^{\mathrm{Dr}}} \left(-\frac{\partial D}{\partial \varepsilon^{\mathrm{r}}} \kappa_s^{\mathrm{r}} + (1-D) \frac{\partial \kappa_s^{\mathrm{r}}}{\partial \Gamma} \frac{\partial \Gamma}{\partial \Delta \varepsilon^{\mathrm{r}}} \right) + \frac{\partial v}{\partial \mu_s^{\mathrm{Dr}}} \left(-\frac{\partial D}{\partial \varepsilon^{\mathrm{r}}} \mu_s^{\mathrm{r}} + (1-D) \frac{\partial \mu_s^{\mathrm{r}}}{\partial \Gamma} \frac{\partial \Gamma}{\partial \Delta \varepsilon^{\mathrm{r}}} \right) \right], \tag{C49}$$

where $\frac{\partial D}{\partial \varepsilon^{\mathrm{r}}}$ is given in Appendix C.2.

C.4 Algorithmic operators[54]

In order to simplify the notation of the equations presented hereafter, the subscript referring to the phase is omitted.

The algorithmic operator $\boldsymbol{C}^{\mathrm{alg}}$ writes:

$$\boldsymbol{C}^{\mathrm{alg}} = \frac{\partial \hat{\boldsymbol{\sigma}}}{\partial \Delta \varepsilon} = \frac{\partial}{\partial \Delta \varepsilon^{\mathrm{r}}} \left[\Delta \hat{\boldsymbol{\sigma}}^{\mathrm{r}} \right] : \frac{\partial \Delta \varepsilon^{\mathrm{r}}}{\partial \Delta \varepsilon} = \frac{\partial \Delta \hat{\boldsymbol{\sigma}}^{\mathrm{r}}}{\partial \Delta \varepsilon^{\mathrm{r}}}. \tag{C50}$$

Having:

$$\Delta \hat{\boldsymbol{\sigma}}_{n+1}^{\mathrm{r}} = \left[\boldsymbol{C}^{\mathrm{el}} - \frac{6 \mu^{\mathrm{el}} \Gamma}{1 + 6 \mu^{\mathrm{el}} \Gamma} \left(\boldsymbol{I}^{\mathrm{dev}} : \boldsymbol{C}^{\mathrm{el}} \right) - \frac{2 \beta \kappa^{\mathrm{el}} \Gamma}{1 + 2 \kappa^{\mathrm{el}} \Gamma \beta} \left(\boldsymbol{I}^{\mathrm{vol}} : \boldsymbol{C}^{\mathrm{el}} \right) \right] : \Delta \varepsilon_{n+1}^{\mathrm{r}}, \tag{C51}$$

the term $\frac{\partial}{\partial \Delta \varepsilon^{\mathrm{r}}}$ writes:

$$\frac{\partial}{\partial \Delta \varepsilon^{\mathrm{r}}} \left[\Delta \hat{\boldsymbol{\sigma}}^{\mathrm{r}} \right] = \boldsymbol{C}^{\mathrm{el}} - 6 \mu^{\mathrm{el}} \left[\left(\hat{\boldsymbol{\sigma}}_{n+1}^{\mathrm{tr}} - \hat{\boldsymbol{\sigma}}_n^{\mathrm{res}} \right)^{\mathrm{dev}} \otimes \left(\frac{\frac{\partial \Gamma}{\partial \Delta \varepsilon^{\mathrm{r}}}}{\left(1 + 6 \mu^{\mathrm{el}} \Gamma \right)^2} \right) + \frac{\Gamma}{1 + 6 \mu^{\mathrm{el}} \Gamma} \left(2 \mu^{\mathrm{el}} \boldsymbol{I}^{\mathrm{dev}} \right) \right]$$

$$- 2 \kappa^{\mathrm{el}} \beta \left[\left(\hat{\boldsymbol{\sigma}}_{n+1}^{\mathrm{tr}} - \hat{\boldsymbol{\sigma}}_n^{\mathrm{res}} \right)^{\mathrm{vol}} \otimes \left(\frac{\frac{\partial \Gamma}{\partial \Delta \varepsilon^r}}{\left(1 + 2 \kappa^{\mathrm{el}} \beta \Gamma \right)^2} \right) + \frac{\Gamma}{1 + 2 \beta \kappa^{\mathrm{el}} \Gamma} \left(3 \kappa^{\mathrm{el}} \boldsymbol{I}^{\mathrm{Vol}} \right) \right]. \tag{C52}$$

Making use of the developments carried out in[54], the yield surface can be written as:

$$f \left(\hat{\boldsymbol{\sigma}}^{\mathrm{tr}}, \Gamma \right) = \left(\frac{\left(\frac{\hat{\boldsymbol{\sigma}}_{n+1}^{\mathrm{tr}} - \hat{\boldsymbol{\sigma}}_n^{\mathrm{res}}}{1 + 6 \mu^{\mathrm{el}} \Gamma} + \hat{\boldsymbol{\sigma}}_n^{\mathrm{res}} \right)^{\mathrm{eq}}}{\sigma_c} \right)^{\alpha} - 3 \frac{m^{\alpha} - 1}{(m+1) \sigma_c} \left(\frac{\hat{\phi}_{n+1}^{\mathrm{tr}} - \hat{\phi}_n^{\mathrm{res}}}{1 + 2 \kappa^{\mathrm{el}} \Gamma \beta} + \hat{\phi}_n^{\mathrm{res}} \right) - \frac{m^{\alpha} + m}{m+1} = 0. \tag{C53}$$

It is then possible to compute the derivative of the yield surface with respect to the plastic multiplier Γ:

$$\frac{df}{d\Gamma} = \left[-\frac{\alpha}{\sigma_c^{\alpha+1}} \frac{\partial R(\Delta p)}{\partial \Delta p} \left(\left(\frac{\hat{\boldsymbol{\sigma}}_{n+1}^{\mathrm{tr}} - \hat{\boldsymbol{\sigma}}_n^{\mathrm{res}}}{1 + 6 \mu^{\mathrm{el}} \Gamma} + \hat{\boldsymbol{\sigma}}_n^{\mathrm{res}} \right)^{\mathrm{eq}} \right)^{\alpha} + 3 \frac{m^{\alpha} - 1}{(m+1) \sigma_c^2} \frac{\partial R(\Delta p)}{\partial \Delta p} \left(\frac{\hat{\phi}_{n+1}^{\mathrm{tr}} - \hat{\phi}_n^{\mathrm{res}}}{1 + 2 \kappa^{\mathrm{el}} \Gamma \beta} + \hat{\phi}_n^{\mathrm{res}} \right) \right] \frac{\partial \Delta p}{\partial \Gamma} + \frac{\partial f}{\partial \Gamma}. \tag{C54}$$

From Eq. (C53), it is possible to compute the derivative $\frac{\partial \Gamma}{\partial \Delta \varepsilon^{\mathrm{r}}} = \frac{\partial \Gamma}{\partial \Delta \varepsilon}$. To that end, one can write:

$$0 = \delta f = \left(\frac{\partial f}{\partial \Delta \varepsilon} + \frac{\partial f}{\partial \Delta p} \underbrace{\frac{\partial \Delta p}{\partial \Delta \varepsilon}}_{= \frac{\partial \Delta p}{\partial \Gamma} \frac{\partial \Gamma}{\partial \Delta \varepsilon}} + \frac{df}{d\Gamma} \frac{\partial \Gamma}{\partial \Delta \varepsilon} \right) : \delta \Delta \varepsilon, \tag{C55}$$

yielding:

$$\frac{\partial \Gamma}{\partial \Delta \varepsilon} = -\left(\frac{df}{d\Gamma} \right)^{-1} \left(\frac{\partial f}{\partial \Delta \varepsilon} + \frac{\partial f}{\partial \Delta p} \frac{\partial \Delta p}{\partial \Gamma} \frac{\partial \Gamma}{\partial \Delta \varepsilon} \right). \tag{C56}$$

One finally finds:

$$\frac{\partial \Gamma}{\partial \Delta \varepsilon} = -\left(\frac{df}{d\Gamma} \right)^{-1} \frac{\partial f}{\partial \Delta \varepsilon} \left[1 + \left(\frac{df}{d\Gamma} \right)^{-1} \frac{\partial f}{\partial \Delta p} \frac{\partial \Delta p}{\partial \Gamma} \right]^{-1}. \tag{C57}$$

The term $\frac{df}{d\Gamma}$ is obtained from Eq. (C54) and the terms $\frac{\partial f}{\partial \Delta p}$, $\frac{\partial \Delta p}{\partial \Gamma}$ and $\frac{\partial f}{\partial \Delta \varepsilon}$ read:

$$\frac{\partial f}{\partial \Delta p} = -\frac{\alpha}{\sigma_c^{\alpha+1}} \frac{\partial R(\Delta p)}{\partial \Delta p} \left(\left(\frac{\hat{\boldsymbol{\sigma}}_{n+1}^{\mathrm{tr}} - \hat{\boldsymbol{\sigma}}_n^{\mathrm{res}}}{1 + 6 \mu^{\mathrm{el}} \Gamma} + \hat{\boldsymbol{\sigma}}_n^{\mathrm{res}} \right)^{\mathrm{eq}} \right)^{\alpha} + 3 \frac{m^{\alpha} - 1}{(m+1) \sigma_c^2} \frac{\partial R(\Delta p)}{\partial \Delta p} \left(\frac{\hat{\phi}_{n+1}^{\mathrm{tr}} - \hat{\phi}_n^{\mathrm{res}}}{1 + 2 \kappa^{\mathrm{el}} \Gamma \beta} + \hat{\phi}_n^{\mathrm{res}} \right), \tag{C58}$$

$$\frac{\partial \Delta p}{\partial \Gamma} = k \sqrt{6\left(\left(\frac{\hat{\boldsymbol{\sigma}}_{n+1}^{\mathrm{tr}} - \hat{\boldsymbol{\sigma}}_{n}^{\mathrm{res}}}{1 + 6\mu^{\mathrm{el}}\Gamma}\right)^{\mathrm{eq}}\right)^{2} + \frac{4\beta^{2}}{3}\left(\frac{\hat{\phi}_{n+1}^{\mathrm{tr}} - \hat{\phi}_{n}^{\mathrm{res}}}{1 + 2\kappa^{\mathrm{el}}\Gamma\beta}\right)^{2}}$$

$$- \frac{k\Gamma}{2\sqrt{6\left(\left(\frac{\hat{\boldsymbol{\sigma}}_{n+1}^{\mathrm{tr}} - \hat{\boldsymbol{\sigma}}_{n}^{\mathrm{res}}}{1 + 6\mu^{\mathrm{el}}\Gamma}\right)^{\mathrm{eq}}\right)^{2} + \frac{4\beta^{2}}{3}\left(\frac{\hat{\phi}_{n+1}^{\mathrm{tr}} - \hat{\phi}_{n}^{\mathrm{res}}}{1 + 2\kappa^{\mathrm{el}}\Gamma\beta}\right)^{2}}} \left[72\mu^{\mathrm{el}}\frac{\left(\left(\hat{\boldsymbol{\sigma}}_{n+1}^{\mathrm{tr}} - \hat{\boldsymbol{\sigma}}_{n}^{\mathrm{res}}\right)^{\mathrm{eq}}\right)^{2}}{\left(1 + 6\mu^{\mathrm{el}}\Gamma\right)^{3}} + \frac{16\beta^{3}\kappa^{\mathrm{el}}}{3}\frac{\left(\hat{\phi}_{n+1}^{\mathrm{tr}} - \hat{\phi}_{n}^{\mathrm{res}}\right)^{2}}{\left(1 + 2\kappa^{\mathrm{el}}\Gamma\beta\right)^{3}}\right], \tag{C59}$$

$$\frac{\partial f}{\partial \Delta \boldsymbol{\varepsilon}} = \frac{1}{\sigma_{c}^{\alpha}} \underbrace{\frac{\partial \left[\left(\frac{\hat{\boldsymbol{\sigma}}_{n+1}^{\mathrm{tr}} - \hat{\boldsymbol{\sigma}}_{n}^{\mathrm{res}}}{1 + 6\mu^{\mathrm{el}}\Gamma} + \hat{\boldsymbol{\sigma}}_{n}^{\mathrm{res}}\right)^{\mathrm{eq}}\right]^{\alpha}}{\partial \Delta \boldsymbol{\varepsilon}}}_{1*} - 3\frac{m^{\alpha} - 1}{(m+1)\sigma_{c}} \underbrace{\frac{\partial \left(\frac{\hat{\phi}_{n+1}^{\mathrm{tr}} - \hat{\phi}_{n}^{\mathrm{res}}}{1 + 2\kappa^{\mathrm{el}}\Gamma\beta} + \hat{\phi}_{n}^{\mathrm{res}}\right)}{\partial \Delta \boldsymbol{\varepsilon}}}_{2*}, \tag{C60}$$

where:

$$1* = \alpha \left[\left(\frac{\hat{\boldsymbol{\sigma}}_{n+1}^{\mathrm{tr}} - \hat{\boldsymbol{\sigma}}_{n}^{\mathrm{res}}}{1 + 6\mu^{\mathrm{el}}\Gamma} + \hat{\boldsymbol{\sigma}}_{n}^{\mathrm{res}}\right)^{\mathrm{eq}}\right]^{\alpha - 1} \frac{\frac{3}{2}\left[\frac{\boldsymbol{I}^{\mathrm{dev}} : \boldsymbol{C}^{\mathrm{el}}}{1 + 6\mu^{\mathrm{el}}\Gamma} : \left(\frac{\hat{\boldsymbol{\sigma}}_{n+1}^{\mathrm{tr}} - \hat{\boldsymbol{\sigma}}_{n}^{\mathrm{res}}}{1 + 6\mu^{\mathrm{el}}\Gamma} + \hat{\boldsymbol{\sigma}}_{n}^{\mathrm{res}}\right)^{\mathrm{dev}}\right]}{\sqrt{\frac{3}{2}\left(\frac{\hat{\boldsymbol{\sigma}}_{n+1}^{\mathrm{tr}} - \hat{\boldsymbol{\sigma}}_{n}^{\mathrm{res}}}{1 + 6\mu^{\mathrm{el}}\Gamma} + \hat{\boldsymbol{\sigma}}_{n}^{\mathrm{res}}\right)^{\mathrm{dev}} : \left(\frac{\hat{\boldsymbol{\sigma}}_{n+1}^{\mathrm{tr}} - \hat{\boldsymbol{\sigma}}_{n}^{\mathrm{res}}}{1 + 6\mu^{\mathrm{el}}\Gamma} + \hat{\boldsymbol{\sigma}}_{n}^{\mathrm{res}}\right)^{\mathrm{dev}}}}; \tag{C61}$$

$$2* = \frac{\kappa^{\mathrm{el}}\boldsymbol{1}}{1 + 2\kappa^{\mathrm{el}}\Gamma\beta}.$$

D EFFECTIVE RANDOM PARAMETER PROBABILITY DENSITY DISTRIBUTION
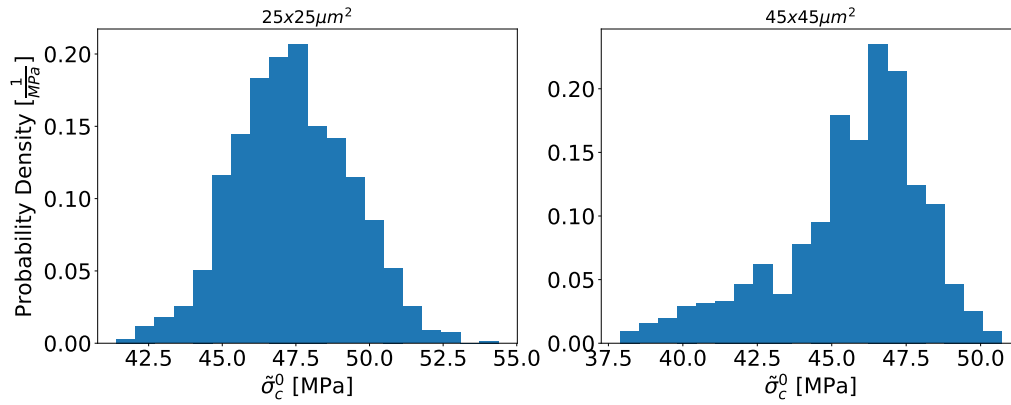
FIGURE D5 Probability density function of the effective yield stress for the $25 \times 25\mu\mathrm{m}^{2}$ and $45 \times 45\mu\mathrm{m}^{2}$ SVE cases.
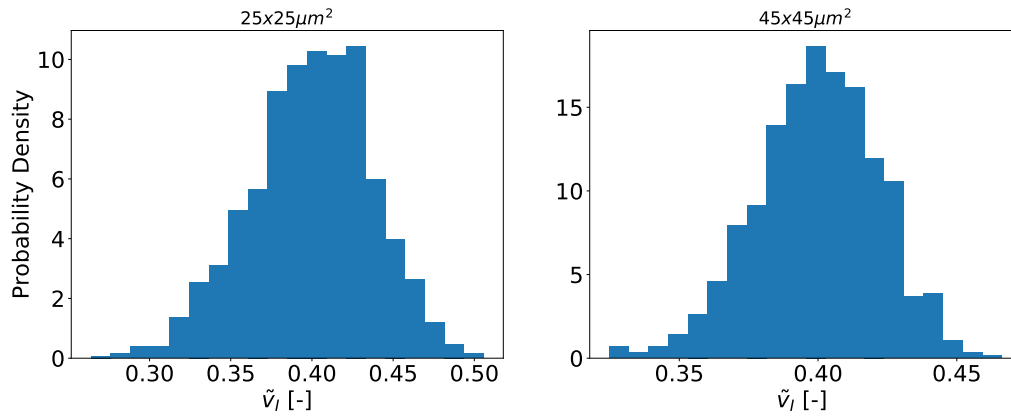
FIGURE D6 Probability density histogram of the effective fibre volume fraction for the $25 \times 25 \mu\text{m}^2$ and $45 \times 45 \mu\text{m}^2$ SVE cases.
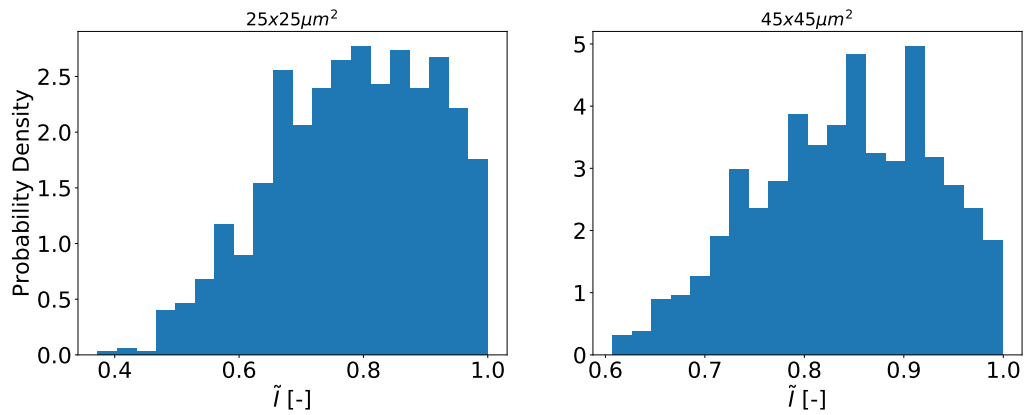

FIGURE D7 Probability density histogram of the effective aspect ratio for the $25 \times 25 \mu\text{m}^2$ and $45 \times 45 \mu\text{m}^2$ SVE cases.
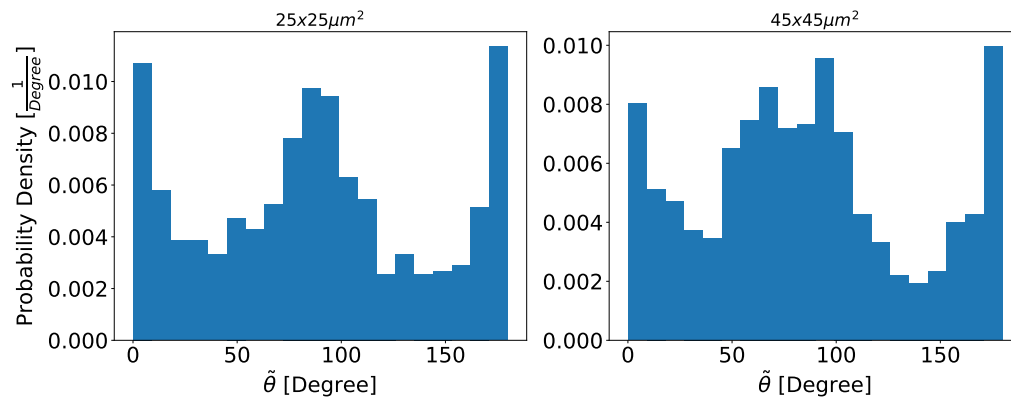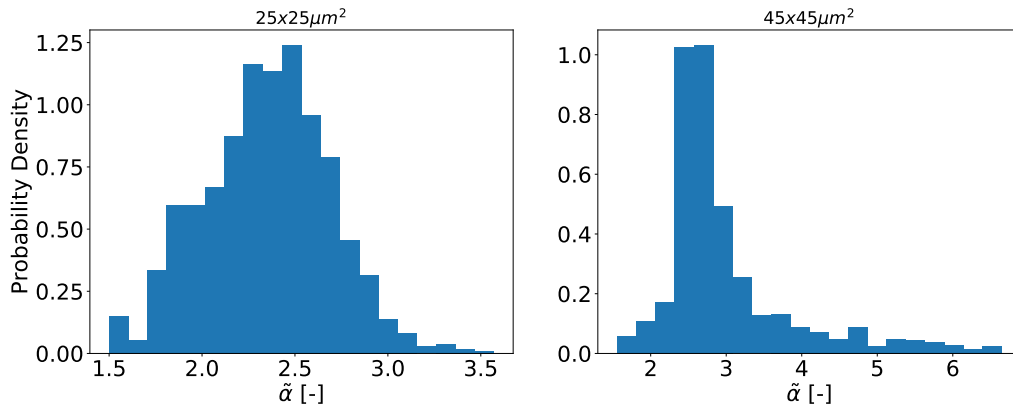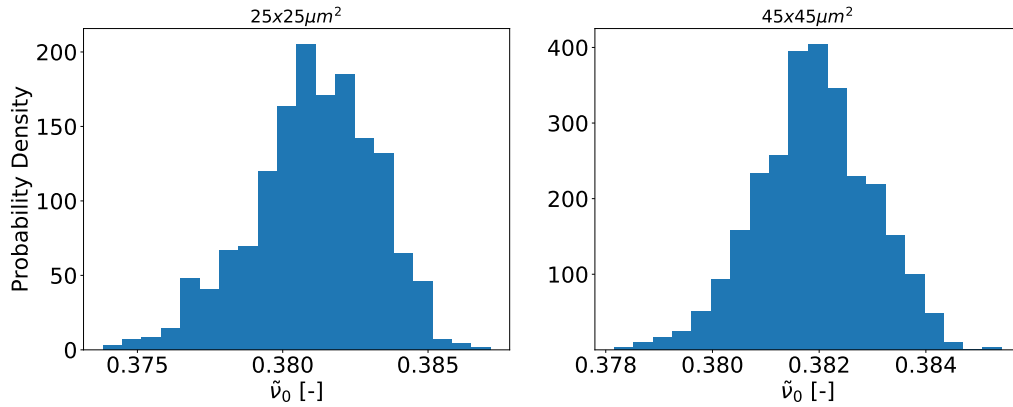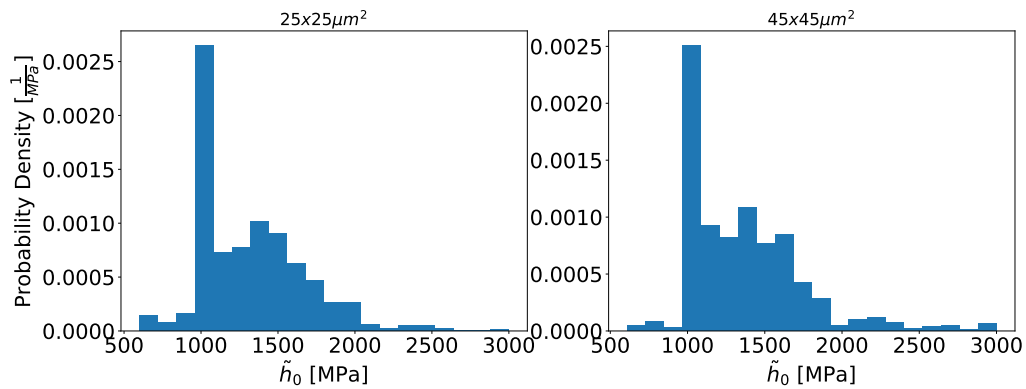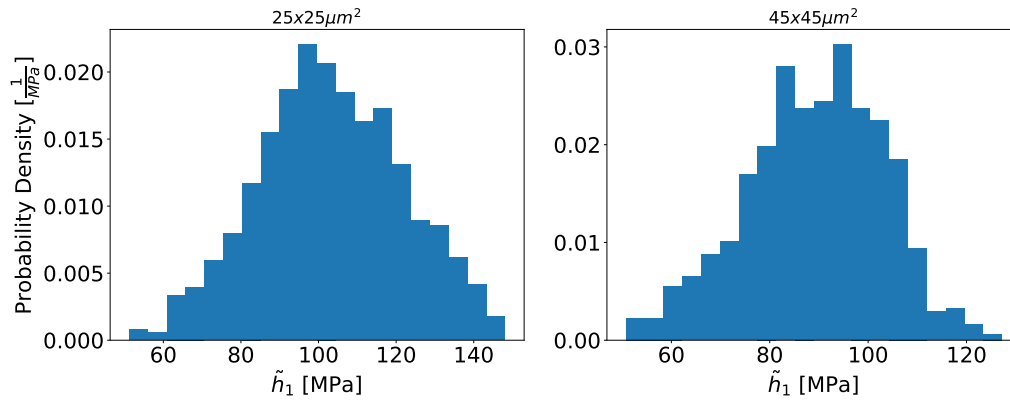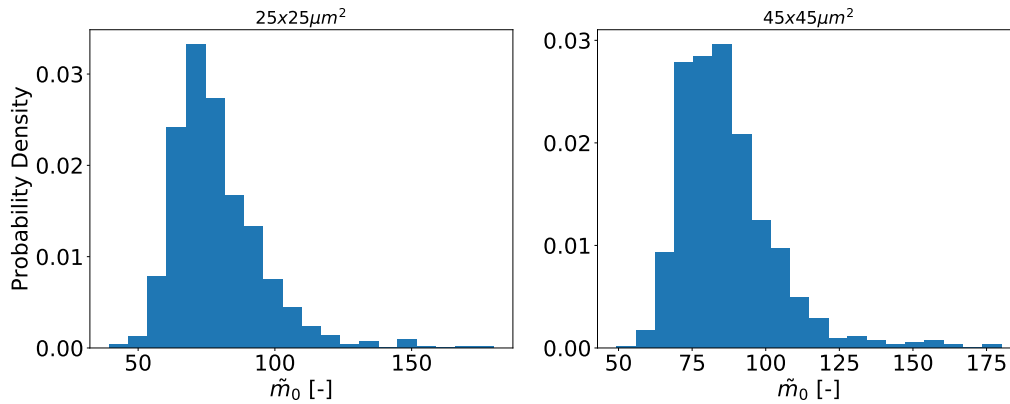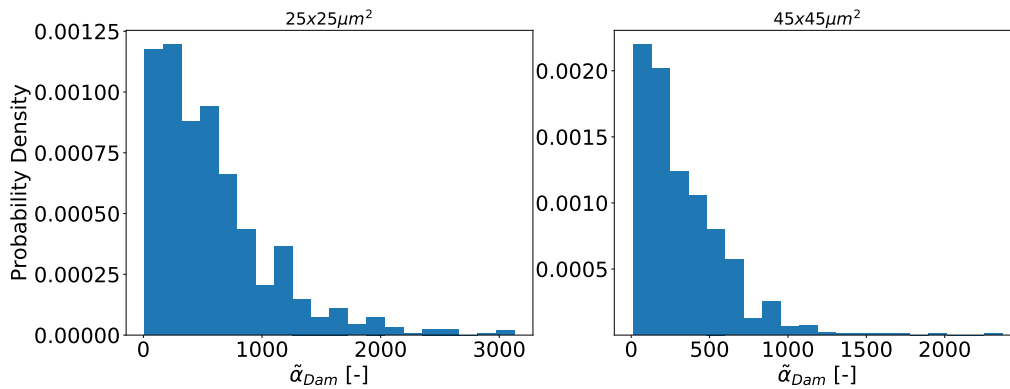

FIGURE D8 Probability density histogram of the effective angle for the $25 \times 25 \mu\text{m}^2$ and $45 \times 45 \mu\text{m}^2$ SVE cases.

FIGURE D9 Probability density histogram of the exponent $\tilde{\alpha}$, $25 \times 25 \mu\mathrm{m}^2$ and $45 \times 45 \mu\mathrm{m}^2$ SVE cases.

FIGURE D10 Probability density histogram of the effective Poisson's ratio for the $25 \times 25 \mu\mathrm{m}^2$ and $45 \times 45 \mu\mathrm{m}^2$ SVE cases.

FIGURE D11 Probability density histogram of the effective hardening parameter $\tilde{h}_0$ for the $25 \times 25 \mu\mathrm{m}^2$ and $45 \times 45 \mu\mathrm{m}^2$ SVE cases.

FIGURE D12 Probability density histogram of the effective hardening parameter $\tilde{h}_1$ for the $25 \times 25\mu\text{m}^2$ and $45 \times 45\mu\text{m}^2$ SVE cases.

FIGURE D13 Probability density histogram of the effective hardening parameter $\tilde{m}_0$ for the $25 \times 25\mu\text{m}^2$ and $45 \times 45\mu\text{m}^2$ SVE cases.

FIGURE D14 Probability density histogram of the effective parameter $\tilde{\alpha}_{\text{Dam}}$ for the $25 \times 25\mu\text{m}^2$ and $45 \times 45\mu\text{m}^2$ SVE cases.

E RESULTS OF THE 45×45 SQUARE MICROMETERS SVE MF-ROM

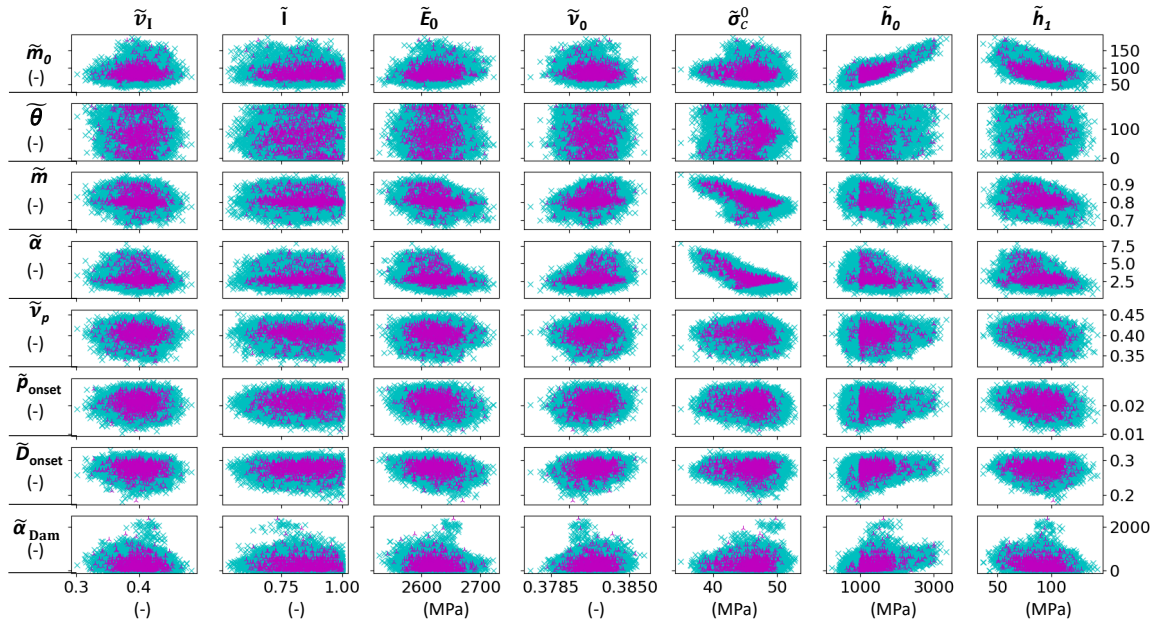## E.1 Statistical analysis of random effective parameters
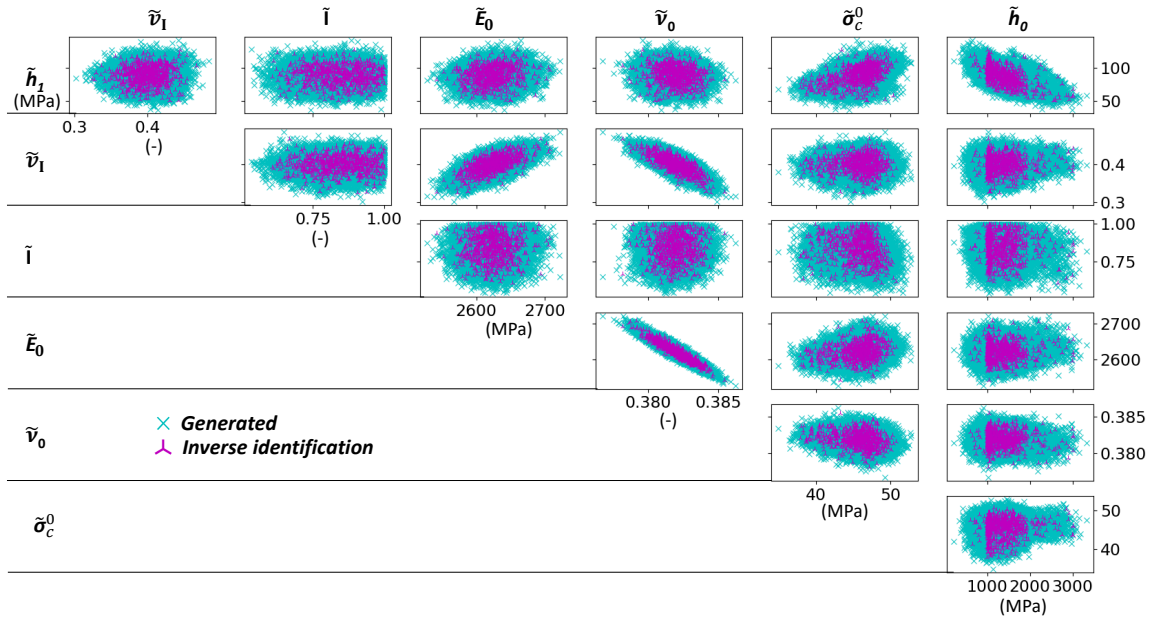
FIGURE E15 $45 \times 45\mu m^2$ effective random parameters distributions and their cross-dependence for random picked identified and generated $\tilde{v}_I, \tilde{I}, \tilde{E}_0, \tilde{v}_0, \tilde{\sigma}_c^0, \tilde{h}_0$ and $\tilde{h}_1$.
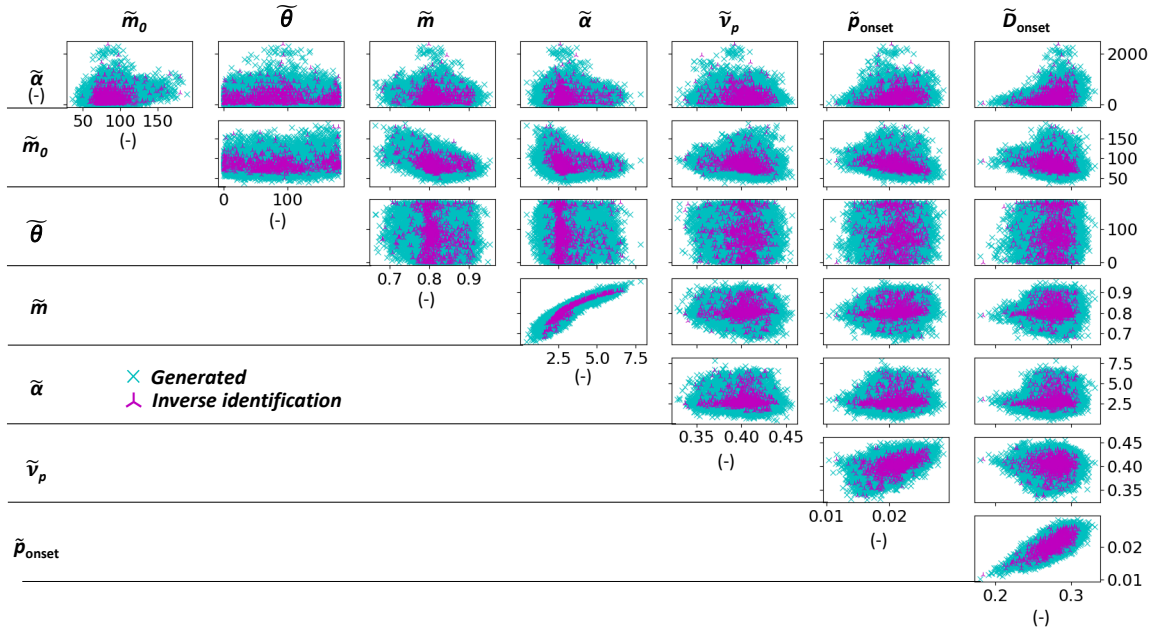
FIGURE E16 $45 \times 45\mu m^2$ effective random parameters distributions and their cross-dependence for random picked identified and generated $\tilde{m}_0, \tilde{\theta}, \tilde{m}, \tilde{v}_p, \tilde{\alpha}, \tilde{p}_{onset}, \widetilde{D}_{onset}$ and $\tilde{\alpha}_{Dam}$.

FIGURE E17 $45 \times 45\mu\text{m}^2$ effective random parameters distributions and their cross-dependence for random picked identified and generated $\tilde{v}_\text{I}, \tilde{\text{I}}, \tilde{\theta}, \tilde{E}_0, \tilde{v}_0, \tilde{\sigma}_c^0, \tilde{h}_0, \tilde{h}_1, \tilde{m}_0, \tilde{m}, \tilde{v}_p, \tilde{\alpha}, \tilde{p}_\text{onset}, \widetilde{D}_\text{onset}$ and $\tilde{\alpha}_\text{Dam}$.
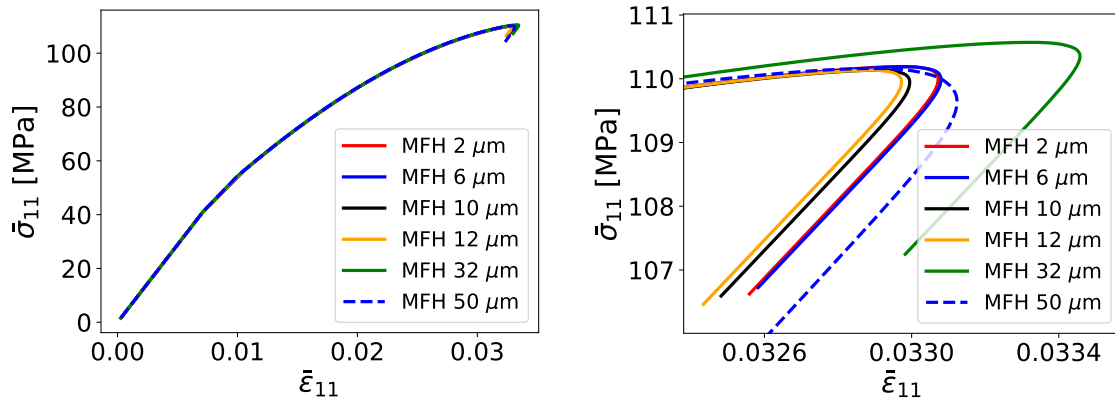
F STOCHASTIC MF-ROM MESH CONVERGENCE STUDY

FIGURE F18 Effect of the macroscale mesh size on a uniaxial loading test conducted on a $500\text{x}250\mu\text{m}^2$ ply with the MF-ROM defined using $25\text{x}25\mu\text{m}^2$ SVEs. Results on the left are zoomed on the right.

A convergence study is performed for the stochastic MF-ROM by considering different sizes of the macroscale finite elements ranging from $2\mu\text{m}$ to $50\mu\text{m}$. To this end, we consider two ply realizations, one using $25\text{x}25\mu\text{m}^2$ SVEs, Fig. F18 and another using $45\text{x}45\mu\text{m}^2$ SVEs, Fig. F19. As a reminder, the characteristic length l, see Eq. (14), of the nonlocal MFH formulation was fixed to a value of 25 μm for both SVE sizes. It clearly appears that for finite elements larger or close to the SVE size, i.e.$32\mu\text{m}$ and $50\mu\text{m}$ for the $25\text{x}25\mu\text{m}^2$ SVEs and the $45\text{x}45\mu\text{m}^2$ SVEs, and larger than the nonlocal length l the results are outliers when analyzing the maximum reached stress. For the other mesh sizes, the results are close, within a 0.3% in terms of the maximum stress, which is well below the variability observed for different ply realizations, see e.g. in Fig. 36. The observed variability in
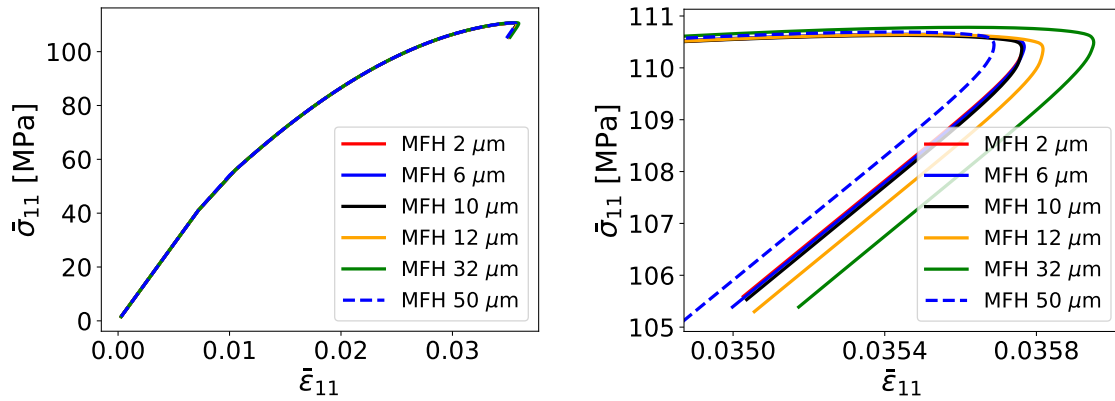
FIGURE F19 Effect of the macroscale mesh size on a uniaxial loading test conducted on a $500 \times 250 \mu m^2$ ply with the MF-ROM defined using $45 \times 45 \mu m^2$ SVEs. Results on the left are zoomed on the right.

the results is mainly explained by the variable step length of the path-following method, which yields slight inaccuracy when performing the time integration.

References

1. Ghanem R, Spanos P. Stochastic Finite Elements: A Spectral Approach. *Springer Verlag* 1991.

2. Charmpis D, Schuëller G, Pellissetti M. The need for linking micromechanics of materials with stochastic finite elements: A challenge for materials science. *Computational Materials Science* 2007; 41(1): 27-37. doi: https://doi.org/10.1016/j.commatsci.2007.02.014

3. Ostoja-Starzewski M, Wang X. Stochastic finite elements as a bridge between random material microstructure and global response. *Computer Methods in Applied Mechanics and Engineering* 1999; 168(1): 35-49. doi: https://doi.org/10.1016/S0045-7825(98)00105-4

4. Noels L. Chapter One - Toward stochastic multiscale methods in continuum solid mechanics. In: . 55 of *Advances in Applied Mechanics*. Elsevier. 2022 (pp. 1-254)

5. Vaughan T, McCarthy C. A combined experimental–numerical approach for generating statistically equivalent fibre distributions for high strength laminated composite materials. *Composites Science and Technology* 2010; 70(2): 291-297. doi: https://doi.org/10.1016/j.compscitech.2009.10.020

6. Melro A, Camanho P, Pinho S. Generation of random distribution of fibres in long-fibre reinforced composites. *Composites Science and Technology* 2008; 68(9): 2092-2102. doi: https://doi.org/10.1016/j.compscitech.2008.03.013

7. Wu L, Chung CN, Major Z, Adam L, Noels L. From SEM images to elastic responses: A stochastic multiscale analysis of UD fiber reinforced composites. *Composite Structures* 2018; 189: 206 - 227. doi: https://doi.org/10.1016/j.compstruct.2018.01.051

8. Blacklock M, Bale H, Begley M, Cox B. Generating virtual textile composite specimens using statistical data from micro-computed tomography: 1D tow representations for the Binary Model. *Journal of the Mechanics and Physics of Solids* 2012; 60(3): 451-470. doi: https://doi.org/10.1016/j.jmps.2011.11.010

9. Tal D, Fish J. Generating a statistically equivalent representative volume element with discrete defects. *Composite Structures* 2016; 153: 791-803. doi: https://doi.org/10.1016/j.compstruct.2016.06.077

10. Vanaerschot A, Cox BN, Lomov SV, Vandepitte D. Stochastic multi-scale modelling of textile composites based on internal geometry variability. *Computers & Structures* 2013; 122: 55-64. Computational Fluid and Solid Mechanics 2013doi: https://doi.org/10.1016/j.compstruc.2012.10.026

11. Gupta A, Cecen A, Goyal S, Singh AK, Kalidindi SR. Structure-property linkages using a data science approach: Application to a non-metallic inclusion/steel composite system. *Acta Materialia* 2015; 91: 239-254. doi: https://doi.org/10.1016/j.actamat.2015.02.045

12. Kanouté P, Boso D, Chaboche J, Schrefler B. Multiscale Methods for Composites: A Review. *Archives of Computational Methods in Engineering* 2009; 16: 31-75.

13. Matouš K, Geers MG, Kouznetsova VG, Gillman A. A review of predictive nonlinear theories for multi-scale modeling of heterogeneous materials. *Journal of Computational Physics* 2017; 330: 192-220. doi: https://doi.org/10.1016/j.jcp.2016.10.070

14. Feyel F. Multiscale FE2 elastoviscoplastic analysis of composite structures. *Computational Materials Science* 1999; 16: 344-354.

15. Miehe C. Strain-driven homogenization of inelastic microstructures and composites based on an incremental variational formulation. *International Journal for Numerical Methods in Engineering* 2002; 55(11): 1285-1322. doi: https://doi.org/10.1002/nme.515

16. Pivovarov D, Mergheim J, Willner K, Steinmann P. Stochastic local FEM for computational homogenization of heterogeneous materials exhibiting large plastic deformations. *Computational Mechanics* 2022; 69: 467-488. doi: 10.1007/s00466-021-02099-x

17. Kouznetsova V, Brekelmans W, Baaijens F. An approach to micro-macro modeling of heterogeneous materials. *Computational Mechanics* 2001; 27(1): 37-48.

18. Kouznetsova V, Geers M, Brekelmans W. Multi-scale second-order computational homogenization of muli-phase materials: a nested finite element solution strategy. *Comput. Methods Appl. Mech. Eng.* 2004; 193: 5525-5550.

19. Pingaro M, Reccia E, Trovalusci P, Masiani R. Fast statistical homogenization procedure (FSHP) for particle random composites using virtual element method. *Computational Mechanics* 2019; 64(1): 197-210.

20. Pingaro M, Reccia E, Trovalusci P. Homogenization of Random Porous Materials With Low-Order Virtual Elements. *ASCE-ASME J Risk and Uncert in Engrg Sys Part B Mech Engrg* 2019; 5(3). 030905doi: 10.1115/1.4043475

21. Pingaro M, De Bellis M, Reccia E, Trovalusci P, Sadowski T. Fast Statistical Homogenization Procedure for estimation of effective properties of Ceramic Matrix Composites (CMC) with random microstructure. *Composite Structures* 2023; 304: 116265. doi: https://doi.org/10.1016/j.compstruct.2022.116265

22. McDowell DL. A perspective on trends in multiscale plasticity. *International Journal of Plasticity* 2010; 26(9): 1280-1309. Special Issue In Honor of David L. McDowelldoi: https://doi.org/10.1016/j.ijplas.2010.02.008

23. Ostoja-Starzewski M, Du X, Khisaeva ZF, Li W. Comparisons of the Size of the Representative Volume Element in Elastic, Plastic, Thermoelastic, and Permeable Random Microstructures. *International Journal for Multiscale Computational Engineering* 2007; 5(2): 73–82.

24. Salmi M, Auslender F, Bornert M, Fogli M. Apparent and effective mechanical properties of linear matrix-inclusion random composites: Improved bounds for the effective behavior. *International Journal of Solids and Structures* 2012; 49(10): 1195-1211. doi: https://doi.org/10.1016/j.ijsolstr.2012.01.018

25. Trovalusci P, Ostoja-Starzewski M, De Bellis ML, Murrali A. Scale-dependent homogenization of random composites as micropolar continua. *European Journal of Mechanics - A/Solids* 2015; 49: 396-407. doi: https://doi.org/10.1016/j.euromechsol.2014.08.010

26. Reccia E, De Bellis ML, Trovalusci P, Masiani R. Sensitivity to material contrast in homogenization of random particle composites as micropolar continua. *Composites Part B: Engineering* 2018; 136: 39-45. doi: https://doi.org/10.1016/j.compositesb.2017.10.017

27. Ostoja-Starzewski M. Scale effects in plasticity of random media: status and challenges. *International Journal of Plasticity* 2005; 21(6): 1119-1160. Plasticity of Multiphase Materialsdoi: https://doi.org/10.1016/j.ijplas.2004.06.008

28. Hachemi A, Chen M, Chen G, Weichert D. Limit state of structures made of heterogeneous materials. *International Journal of Plasticity* 2014; 63: 124-137. Deformation Tensors in Material Modeling in Honor of Prof. Otto T. Bruhnsdoi: https://doi.org/10.1016/j.ijplas.2014.03.019

29. Lucas V, Golinval JC, Paquay S, Nguyen VD, Noels L, Wu L. A stochastic computational multiscale approach; Application to MEMS resonators. *Computer Methods in Applied Mechanics and Engineering* 2015; 294: 141-167. doi: https://doi.org/10.1016/j.cma.2015.05.019

30. Yvonnet J, He QC. The reduced model multiscale method (R3M) for the non-linear homogenization of hyperelastic media at finite strains. *Journal of Computational Physics* 2007; 223(1): 341-368. doi: https://doi.org/10.1016/j.jcp.2006.09.019

31. Hernández J, Oliver J, Huespe A, Caicedo M, Cante J. High-performance model reduction techniques in computational multiscale homogenization. *Computer Methods in Applied Mechanics and Engineering* 2014; 276: 149-189. doi: https://doi.org/10.1016/j.cma.2014.03.011

32. Soldner D, Brands B, Zabihyan R, Steinmann P, Mergheim J. A numerical study of different projection-based model reduction techniques applied to computational homogenisation. *Computational Mechanics volume* 2017; 60: 613,625. doi: 10.1007/s00466-017-1428-x

33. Michel JC, Suquet P. Non-uniform transformation field analysis: A reduced model for multiscale non-linear problems in solid mechanics. 2009: 159-206. doi: 10.1142/9781848163089/0004

34. Michel JC, Suquet P. A model-reduction approach in micromechanics of materials preserving the variational structure of constitutive relations. *Journal of the Mechanics and Physics of Solids* 2016; 90: 254-285. doi: https://doi.org/10.1016/j.jmps.2016.02.005

35. Liu Z, Bessa M, Liu WK. Self-consistent clustering analysis: An efficient multi-scale scheme for inelastic heterogeneous materials. *Computer Methods in Applied Mechanics and Engineering* 2016; 306: 319-341. doi: https://doi.org/10.1016/j.cma.2016.04.004

36. Pivovarov D, Steinmann P, Willner K. Acceleration of the spectral stochastic FEM using POD and element based discrete empirical approximation for a micromechanical model of heterogeneous materials with random geometry. *Computer Methods in Applied Mechanics and Engineering* 2020; 360. doi: 10.1016/j.cma.2019.112689

37. Clément A, Soize C, Yvonnet J. Computational nonlinear stochastic homogenization using a nonconcurrent multiscale approach for hyperelastic heterogeneous microstructures analysis. *International Journal for Numerical Methods in Engineering* 2012; 91(8): 799-824. doi: https://doi.org/10.1002/nme.4293

38. Yvonnet J, Monteiro E, He QC. Computational homogenization method and reduced database model for hyperelastic heterogeneous structures. *International Journal for Multiscale Computational Engineering* 2013; 11(3): 201–225.

39. Hashemi MS, Safdari M, Sheidaei A. A supervised machine learning approach for accelerating the design of particulate composites: Application to thermal conductivity. *Computational Materials Science* 2021; 197: 110664. doi: 10.48550/ARXIV.2010.00041

40. Lu X, Yvonnet J, Papadopoulos L, Kalogeris I, Papadopoulos V. A Stochastic FE2 Data-Driven Method for Nonlinear Multiscale Modeling. *Materials* 2021; 14(11). doi: 10.3390/ma14112875

41. Lu X, Glovanis D, Yvonnet J, Papadopoulos V, Detrez F. A data-driven computational homogenization method based on neural networks for the nonlinear anisotropic electrical response of graphene/polymer nanocomposites. *Computational Mechanics* 2019; 64: 307–321. doi: 10.1007/s00466-018-1643-0

42. Fritzen F, Fernández M, Larsson F. On-the-Fly Adaptivity for Nonlinear Twoscale Simulations Using Artificial Neural Networks and Reduced Order Modeling. *Frontiers in Materials* 2019; 6. doi: 10.3389/fmats.2019.00075

43. Liu Z, Wu C, Koishi M. A deep material network for multiscale topology learning and accelerated nonlinear modeling of heterogeneous materials. *Computer Methods in Applied Mechanics and Engineering* 2019; 345: 1138-1168. doi: https://doi.org/10.1016/j.cma.2018.09.020

44. Huang T, Liu Z, Wu C, Chen W. Microstructure-guided deep material network for rapid nonlinear material modeling and uncertainty quantification. *Computer Methods in Applied Mechanics and Engineering* 2022; 398: 115197. doi: https://doi.org/10.1016/j.cma.2022.115197

45. Wu L, Adam L, Noels L. A micromechanics-based inverse study for stochastic order reduction of elastic UD fiber reinforced composites analyses. *International Journal for Numerical Methods in Engineering* 2018; 115(12): 1430-1456. doi: https://doi.org/10.1002/nme.5903

46. Eshelby JD, Peierls RE. The determination of the elastic field of an ellipsoidal inclusion, and related problems. *Proceedings of the Royal Society of London. Series A. Mathematical and Physical Sciences* 1957; 241(1226): 376-396. doi: 10.1098/rspa.1957.0133

47. Mori T, Tanaka K. Average stress in matrix and average elastic energy of materials with misfitting inclusions. *Acta Metallurgica* 1973; 21(5): 571-574. doi: https://doi.org/10.1016/0001-6160(73)90064-3

48. Benveniste Y. A new approach to the application of Mori-Tanaka's theory in composite materials. *Mechanics of Materials* 1987; 6(2): 147-157. doi: https://doi.org/10.1016/0167-6636(87)90005-6

49. Kröner E. Berechnung der elastischen Konstanten des Vielkristalls aus den Konstanten des Einkristalls. *Zeitschrift für Physik* 1958; 151: 504-518.

50. Hill R. A self-consistent mechanics of composite materials. *Journal of the Mechanics and Physics of Solids* 1965; 13(4): 213-222. doi: https://doi.org/10.1016/0022-5096(65)90010-4

51. Hill R. Continuum micro-mechanics of elastoplastic polycrystals. *Journal of the Mechanics and Physics of Solids* 1965; 13(2): 89-101. doi: https://doi.org/10.1016/0022-5096(65)90023-2

52. Talbot D, J.R. W. Variational Principles for Inhomogeneous Non-linear Media. *IMA Journal of Applied Mathematics* 1985; 35(1): 39-54. doi: 10.1093/imamat/35.1.39

53. Wu L, Nguyen VD, Adam L, Noels L. An inverse micro-mechanical analysis toward the stochastic homogenization of nonlinear random composites. *Computer Methods in Applied Mechanics and Engineering* 2019; 348: 97-138. doi: https://doi.org/10.1016/j.cma.2019.01.016

54. Calleja Vázquez JM, Wu L, Nguyen VD, Noels L. An incremental-secant mean-field homogenization model enhanced with a non-associated pressure-dependent plasticity model. *International Journal for Numerical Methods in Engineering* 2022; 123(19): 4616-4654. doi: https://doi.org/10.1002/nme.7048

55. Verhoosel CV, Remmers JJC, Gutiérrez MA, Borst dR. Computational homogenization for adhesive and cohesive failure in quasi-brittle solids. *International Journal for Numerical Methods in Engineering* 2010; 83(8-9): 1155-1179. doi: https://doi.org/10.1002/nme.2854

56. Nguyen VD, Wu L, Noels L. A micro-mechanical model of reinforced polymer failure with length scale effects and predictive capabilities. Validation on carbon fiber reinforced high-crosslinked RTM6 epoxy resin. *Mechanics of Materials* 2019; 133: 193-213. doi: https://doi.org/10.1016/j.mechmat.2019.02.017

57. Mosby M, Matous K. On mechanics and material length scales of failure in heterogeneous interfaces using a finite strain high performance solver. *Modelling and Simulation in Materials Science and Engineering* 2015; 23. doi: https://doi.org/10.1088/0965-0393/23/8/085014

58. Phu Nguyen V, Lloberas-Valls O, Stroeven M, Johannes Sluys L. On the existence of representative volumes for softening quasi-brittle materials - A failure zone averaging scheme. *Computer Methods in Applied Mechanics and Engineering* 2010; 199(45): 3028-3038. doi: https://doi.org/10.1016/j.cma.2010.06.018

59. Wu L, Zhang T, Maillard E, Adam L, Martiny P, Noels L. Per-phase spatial correlated damage models of UD fibre reinforced composites using mean-field homogenisation; applications to notched laminate failure and yarn failure of plain woven composites. *Computers and Structures* 2021; 257: 106650. doi: https://doi.org/10.1016/j.compstruc.2021.106650

60. Peerlings RHJ, Borst dR, Brekelmans WAM, Vree dJHP. Gradient enhanced damage for quasi-brittle materials. *International Journal for Numerical Methods in Engineering* 1996; 39(19): 3391-3403. doi: https://doi.org/10.1002/(SICI)1097-0207(19961015)39:19<3391::AID-NME7>3.0.CO;2-D

61. Peerlings RHJ, Borst dR, Brekelmans WAM, Geers MGD. Gradient-enhanced damage modelling of concrete fracture. *Mechanics of Cohesive-frictional Materials* 1998; 3(4): 323-342. doi: https://doi.org/10.1002/(SICI)1099-1484(1998100)3:4<323::AID-CFM51>3.0.CO;2-Z

62. Geers M, de Borst R, Brekelmans W, Peerlings R. Strain-based transient-gradient damage model for failure analyses. *Computer Methods in Applied Mechanics and Engineering* 1998; 160(1): 133-153. doi: https://doi.org/10.1016/S0045-7825(98)80011-X

63. Peerlings R, Geers M, de Borst R, Brekelmans W. A critical comparison of nonlocal and gradient-enhanced softening continua. *International Journal of Solids and Structures* 2001; 38(44): 7723-7746. doi: https://doi.org/10.1016/S0020-7683(01)00087-7

64. Wu L, Sket F, Molina-Aldareguia J, et al. A study of composite laminates failure using an anisotropic gradient-enhanced damage mean-field homogenization model. *Composite Structures* 2015; 126: 246-264. doi: https://doi.org/10.1016/j.compstruct.2015.02.070

65. Nguyen VD, Béchet E, Geuzaine C, Noels L. Imposing periodic boundary condition on arbitrary meshes by polynomial interpolation. *Computational Materials Science* 2012; 55: 390-406. doi: https://doi.org/10.1016/j.commatsci.2011.10.017

66. Firooz S, Saeb S, Chatzigeorgiou G, Meraghni F, Steinmann P, Javili A. Systematic study of homogenization and the utility of circular simplified representative volume element. *Mathematics and Mechanics of Solids* 2019; 24(9): 2961-2985. doi: 10.1177/1081286518823834

67. Khoei AR, Saadat MA. A nonlocal computational homogenization of softening quasi-brittle materials. *International Journal for Numerical Methods in Engineering* 2019; 119(8): 712-736. doi: https://doi.org/10.1002/nme.6070

68. Coenen E, Kouznetsova V, Geers M. Novel boundary conditions for strain localization analyses in microstructural volume elements. *International Journal for Numerical Methods in Engineering* 2012; 90(1): 1-21. doi: https://doi.org/10.1002/nme.3298

69. Nguyen VD, Wu L, Noels L. Unified treatment of microscopic boundary conditions and efficient algorithms for estimating tangent operators of the homogenized behavior in the computational homogenization method. *Computational Mechanics* 2017; 59: 483-505. doi: 10.1007/s00466-016-1358-z

70. Bonet J, Burton A. A simple orthotropic, transversely isotropic hyperelastic constitutive equation for large strain computations. *Computer Methods in Applied Mechanics and Engineering* 1998; 162(1): 151-164. doi: https://doi.org/10.1016/S0045-7825(97)00339-3

71. Wu L, Tjahjanto D, Becker G, Makradi A, Jérusalem A, Noels L. A micro–meso-model of intra-laminar fracture in fiber-reinforced composites based on a discontinuous Galerkin/cohesive zone method. *Engineering Fracture Mechanics* 2013; 104: 162-183. doi: https://doi.org/10.1016/j.engfracmech.2013.03.018

72. Nguyen VD, Lani F, Pardoen T, Morelle X, Noels L. A large strain hyperelastic viscoelastic-viscoplastic-damage constitutive model based on a multi-mechanism non-local damage continuum for amorphous glassy polymers. *International Journal of Solids and Structures* 2016; 96: 192-216. doi: https://doi.org/10.1016/j.ijsolstr.2016.06.008

73. Wu L, Noels L, Adam L, Doghri I. A combined incremental-secant mean-field homogenization scheme with per-phase residual strains for elasto-plastic composites. *International Journal of Plasticity* 2013; 51: 80-102. doi: https://doi.org/10.1016/j.ijplas.2013.06.006

74. Berveiller M, Zaoui A. An extension of the self-consistent scheme to plastically-flowing polycrystals. *Journal of the Mechanics and Physics of Solids* 1978; 26(5): 325-344. doi: https://doi.org/10.1016/0022-5096(78)90003-0

75. Tandon GP, Weng GJ. A Theory of Particle-Reinforced Plasticity. *Journal of Applied Mechanics* 1988; 55(1): 126-135. doi: 10.1115/1.3173618

76. Castaneda PP. The effective mechanical properties of nonlinear isotropic composites. *Journal of the Mechanics and Physics of Solids* 1991; 39(1): 45-71. doi: https://doi.org/10.1016/0022-5096(91)90030-R

77. Lahellec N, Suquet P. On the effective behavior of nonlinear inelastic composites: I. Incremental variational principles. *Journal of the Mechanics and Physics of Solids* 2007; 55(9): 1932-1963. doi: https://doi.org/10.1016/j.jmps.2007.02.003

78. Brassart L, Stainier L, Doghri I, Delannay L. A variational formulation for the incremental homogenization of elasto-plastic composites. *Journal of the Mechanics and Physics of Solids* 2011; 59(12): 2455-2475. doi: https://doi.org/10.1016/j.jmps.2011.09.004

79. Boudet J, Auslender F, Bornert M, Lapusta Y. An incremental variational formulation for the prediction of the effective work-hardening behavior and field statistics of elasto-(visco)plastic composites. *International Journal of Solids and Structures* 2016; 83: 90-113. doi: https://doi.org/10.1016/j.ijsolstr.2016.01.003

80. Lucchetta A, Auslender F, Bornert M, Kondo D. A double incremental variational procedure for elastoplastic composites with combined isotropic and linear kinematic hardening. *International Journal of Solids and Structures* 2019; 158: 243-267. doi: https://doi.org/10.1016/j.ijsolstr.2018.09.012

81. Molinari A, Canova G, Ahzi S. A self consistent approach of the large deformation polycrystal viscoplasticity. *Acta Metallurgica* 1987; 35(12): 2983-2994. doi: https://doi.org/10.1016/0001-6160(87)90297-5

82. Masson R, Bornert M, Suquet P, Zaoui A. An affine formulation for the prediction of the effective properties of nonlinear composites and polycrystals. *Journal of the Mechanics and Physics of Solids* 2000; 48(6): 1203-1227. doi: https://doi.org/10.1016/S0022-5096(99)00071-X

83. Pierard O, Doghri I. An enhanced affine formulation and the corresponding numerical algorithms for the mean-field homogenization of elasto-viscoplastic composites. *International Journal of Plasticity* 2006; 22(1): 131-157. doi: https://doi.org/10.1016/j.ijplas.2005.04.001

84. Doghri I, Adam L, Bilger N. Mean-field homogenization of elasto-viscoplastic composites based on a general incrementally affine linearization method. *International Journal of Plasticity* 2010; 26(2): 219-238. doi: https://doi.org/10.1016/j.ijplas.2009.06.003

85. Miled B, Doghri I, Brassart L, Delannay L. Micromechanical modeling of coupled viscoelastic-viscoplastic composites based on an incrementally affine formulation. *International Journal of Solids and Structures* 2013; 50(10): 1755-1769. doi: https://doi.org/10.1016/j.ijsolstr.2013.02.004

86. Hutchinson JW, Hill R. Elastic-plastic behaviour of polycrystalline metals and composites. *Proceedings of the Royal Society of London. A. Mathematical and Physical Sciences* 1970; 319(1537): 247-272. doi: 10.1098/rspa.1970.0177

87. Doghri I, Ouaar A. Homogenization of two-phase elasto-plastic composite materials and structures: Study of tangent operators, cyclic plasticity and numerical algorithms. *International Journal of Solids and Structures* 2003; 40(7): 1681-1712. doi: https://doi.org/10.1016/S0020-7683(03)00013-1

88. Mercier S, Kowalczyk-Gajewska K, Czarnota C. Effective behavior of composites with combined kinematic and isotropic hardening based on additive tangent Mori–Tanaka scheme. *Composites Part B: Engineering* 2019; 174: 107052. doi: https://doi.org/10.1016/j.compositesb.2019.107052

89. Chaboche J, Kanouté P, Roos A. On the capabilities of mean-field approaches for the description of plasticity in metal matrix composites. *International Journal of Plasticity* 2005; 21(7): 1409-1434. doi: https://doi.org/10.1016/j.ijplas.2004.07.001

90. Wu L, Noels L, Adam L, Doghri I. An implicit-gradient-enhanced incremental-secant mean-field homogenization scheme for elasto-plastic composites with damage. *International Journal of Solids and Structures* 2013; 50(24): 3843-3860. doi: https://doi.org/10.1016/j.ijsolstr.2013.07.022

91. Wu L, Adam L, Doghri I, Noels L. An incremental-secant mean-field homogenization method with second statistical moments for elasto-visco-plastic composite materials. *Mechanics of Materials* 2017; 114: 180-200. doi: https://doi.org/10.1016/j.mechmat.2017.08.006

92. Haddad M, Doghri I, Pierard O. Viscoelastic-viscoplastic polymer composites: Development and evaluation of two very dissimilar mean-field homogenization models. *International Journal of Solids and Structures* 2022; 236-237: 111354. doi: https://doi.org/10.1016/j.ijsolstr.2021.111354

93. Wu L, Zulueta K, Major Z, Arriaga A, Noels L. Bayesian inference of non-linear multiscale model parameters accelerated by a Deep Neural Network. *Computer Methods in Applied Mechanics and Engineering* 2020; 360: 112693. doi: 10.1016/j.cma.2019.112693

94. Soize C, Ghanem R. Data-driven probability concentration and sampling on manifold. *Journal of Computational Physics* 2016; 321: 242-258. doi: https://doi.org/10.1016/j.jcp.2016.05.044

95. Székely GJ, Rizzo ML, Bakirov NK. Measuring and testing dependence by correlation of distances. *The Annals of Statistics* 2007; 35(6): 2769 – 2794. doi: 10.1214/009053607000000505

96. Chevalier J, Camanho P, Pardoen T. Multi-scale characterization and modelling of the transverse compression response of unidirectional carbon fiber reinforced epoxy. *Comp. Struct.* 2019.

97. Wu L, Adam L, Noels L. Micro-mechanics and data-driven based reduced order models for multi-scale analyses of woven composites. *Composite Structures* 2021; 270: 114058. doi: https://doi.org/10.1016/j.compstruct.2021.114058

98. Calleja Vázquez JM, Wu L, Nguyen VD, Noels L. Data of A micromechanical Mean-Field Homogenization surrogate for the stochastic multiscale analysis of composite materials failure. 2023

99. Melro A, Camanho P, Andrade Pires F, Pinho S. Micromechanical analysis of polymer composites reinforced by unidirectional fibres: Part I – Constitutive modelling. *International Journal of Solids and Structures* 2013; 50(11): 1897-1905. doi: https://doi.org/10.1016/j.ijsolstr.2013.02.009

100. Al-Rub RKA, Tehrani AH, Darabi MK. Application of a large deformation nonlinear-viscoelastic viscoplastic visco-damage constitutive model to polymers and their composites. *International Journal of Damage Mechanics* 2015; 24(2): 198-244. doi: 10.1177/1056789514527020

101. Vogler M, Rolfes R, Camanho P. Modeling the inelastic deformation and fracture of polymer composites - Part I: Plasticity model. *Mechanics of Materials* 2013; 59: 50-64. doi: https://doi.org/10.1016/j.mechmat.2012.12.002

102. Simo JC, Hughes TJ. *Computational inelasticity*. Springer Science and Business Media . 2006.

103. Lemaitre J, Chaboche JL. *Mechanics of Solid Materials*. Cambridge University Press . 1990

104. Morelle C, Chevalier J, Bailly C, Pardoen T, Lani F. Mechanical characterization and modeling of the deformation and failure of the highly crosslinked RTM6 epoxy resin. *Mechanics of Time-Dependent Materials* 2017; 21: 419-454. doi: https://doi.org/10.1007/s11043-016-9336-6

105. Székely GJ, Rizzo ML, Bakirov NK. Measuring and testing dependence by correlation of distances. *Ann. Statist.* 2007; 35(6): 2769–2794. doi: 10.1214/009053607000000505